POLITECNICO
MILANO 1863

SCUOLA DI INGEGNERIA INDUSTRIALE
E DELL'INFORMAZIONE

Femtosecond-laser-written wavelength division multiplexer for quantum photonics applications

Tesi di Laurea Magistrale in
Physics Engineering - Ingegneria Fisica

Author: **Giulio Gualandi**

Student ID: 945223
Advisor: Prof. Roberto Osellame
Co-advisors: Simone Atzeni
Academic Year: 2020-21

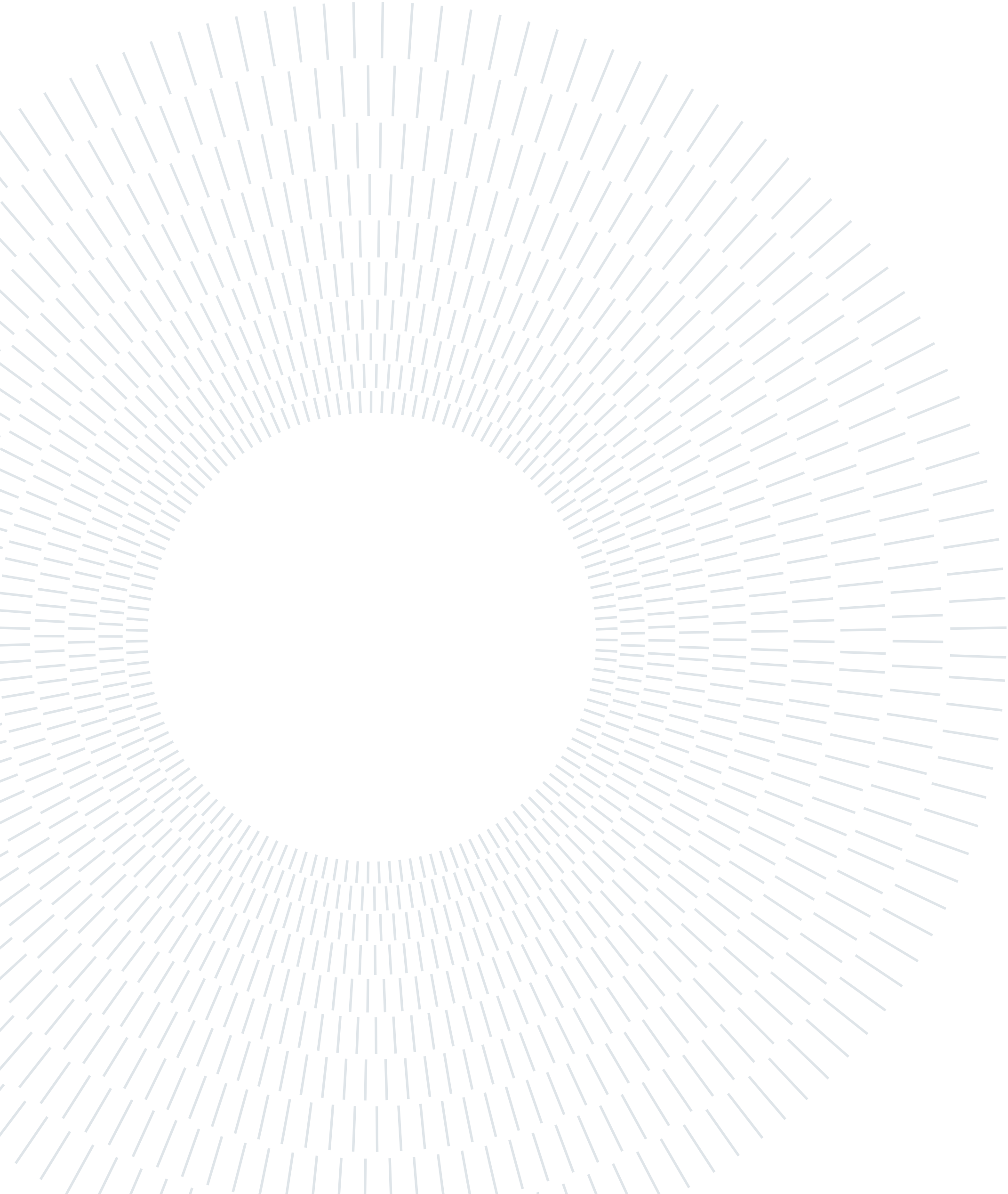

Abstract

The implementation of an integrated source capable of generating complex quantum states is a key milestone in the development of photonic quantum technologies. Integrated optics represents one of the most promising platforms to fulfil this task. Indeed, the generation of single photon-pairs, based on non-degenerate spontaneous parametric down conversion in integrated waveguides, represents a promising solution due to the enhanced stability and the increased nonlinear interaction. However, a complete standalone and integrated source should not only encompass the photon-pairs generation stage, but it should feature both an efficient pump filtering and the capability to divide idler (heralding) photons from the signal (heralded) ones. In this thesis, the fabrication and characterization of an integrated Wavelength Division Multiplexer (WDM) for a heralded integrated single-photons source is presented. This component relies on the wavelength dependence of the coupling coefficient in directional couplers. This device has been fabricated using the Femtosecond Laser Micromachining technique in a glass substrate. First, we fabricated a WDM at telecom wavelengths of 1550/1310 nm achieving very good extinction ratio, namely 24 and 22 dB respectively. We also fabricated and tested a WDM at closer wavelengths, i.e. 1510/1588 nm, obtaining an extinction ratio of 17 e 16 dB respectively. In addition, with the aim of optimizing the overall performance of this component by reducing its optical losses, we studied a new fabrication process on a different glass substrate, namely the Borofloat 33 instead of EAGLE XG. In particular, for the new substrate we measured propagation losses around 0.03 dB/cm for straight waveguides, which can be considered a state-of-the-art result for waveguides fabricated via femtosecond laser writing and are almost an order of magnitude better with respect to the previous platform. Finally, a 1510/1588 nm WDM was fabricated using this substrate, achieving an extinction ratio of 19 dB for both wavelengths.

Keywords: Quantum computing; Integrated single photon sources; Integrated optics; Femtosecond laser micromachining; Wavelength division multiplexer.

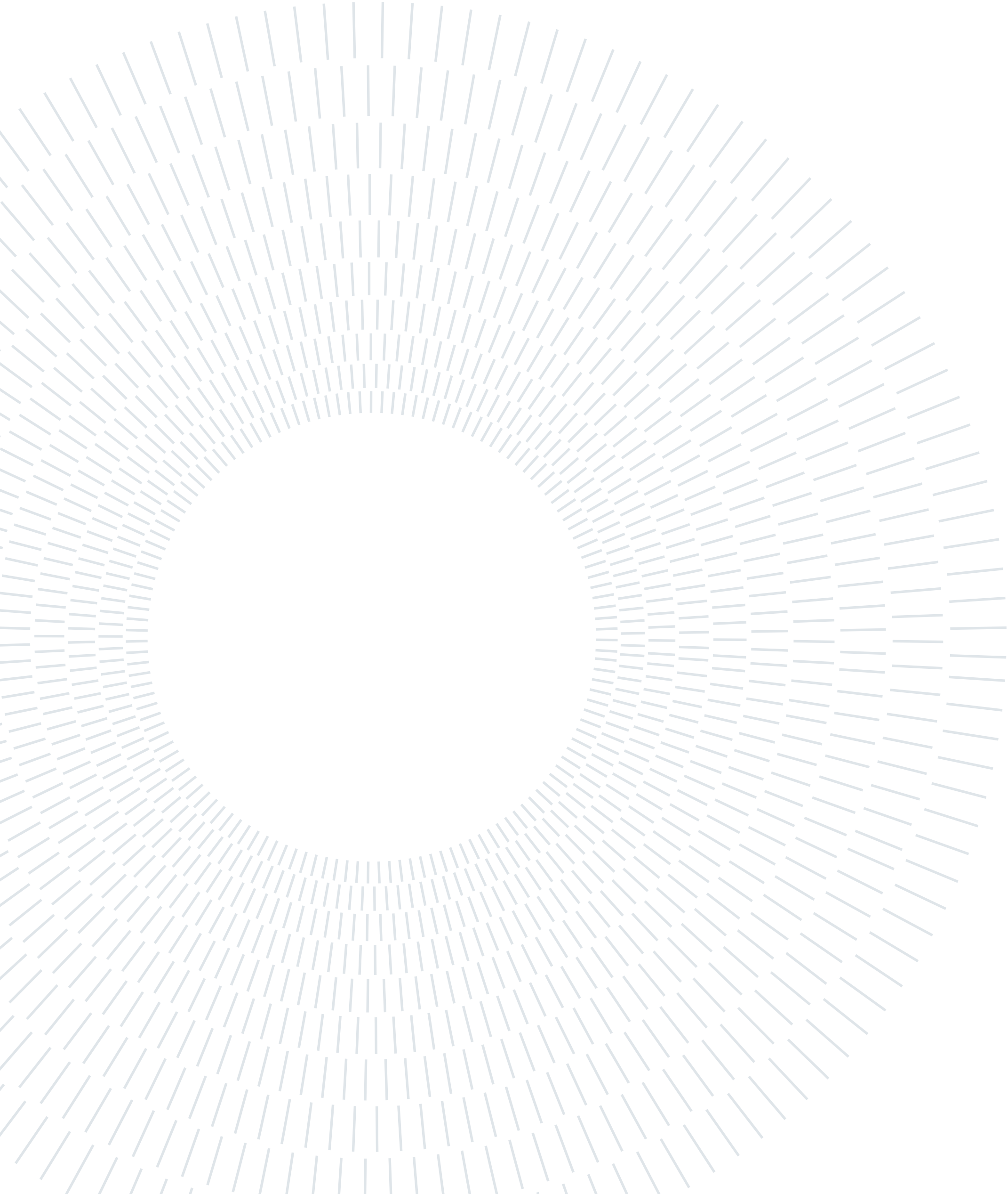

Abstract in lingua italiana

L'implementazione di una sorgente integrata in grado di generare stati quantistici complessi è un traguardo fondamentale nello sviluppo delle tecnologie quantistiche fotoniche. L'ottica integrata rappresenta una delle piattaforme più promettenti per realizzare questo compito. Infatti, la generazione di coppie di singoli fotoni, basata sul processo spontaneo di parametric down conversion non degenere in guide d'onda integrate, rappresenta una soluzione promettente grazie alla maggiore stabilità e alla maggiore interazione non lineare. Tuttavia, una sorgente completa, autonoma e integrata, non dovrebbe comprendere solo la fase di generazione delle coppie di fotoni, ma dovrebbe essere dotata sia di un efficiente filtraggio della pompa che della capacità di dividere i fotoni idler (annunciatori) da quelli di signal (annunciati). In questa tesi, viene presentata la fabbricazione e la caratterizzazione di un wavelength division multiplexer per una sorgente integrata di singoli fotoni annunciati. Questo componente si basa sulla dipendenza dalla lunghezza d'onda del coefficiente di accoppiamento negli accoppiatori direzionali. Questo dispositivo è stato fabbricato usando la tecnica di microfabbricazione di guide con laser a femtosecondi in un substrato di vetro. Per prima cosa, abbiamo fabbricato un WDM per le lunghezze d'onda tipiche della telecomunicazione di 1550/1310 nm raggiungendo un ottimo rapporto di estinzione, ovvero 24 e 22 dB rispettivamente. Abbiamo anche fabbricato e testato un WDM a lunghezze d'onda più vicine, cioè 1510/1588 nm, ottenendo un rapporto di estinzione di 17 e 16 dB rispettivamente. Inoltre, allo scopo di ottimizzare le prestazioni complessive di questo componente riducendo le sue perdite ottiche, abbiamo studiato un nuovo processo di fabbricazione su un diverso substrato di vetro, ovvero usando Borofloat 33 invece di EAGLE XG. In particolare, per il nuovo substrato abbiamo misurato perdite di propagazione intorno a 0.03 dB/cm per guide d'onda dritte, il che può essere considerato uno tra i migliori risultati nello stato dell'arte per guide d'onda fabbricate tramite scrittura laser a femtosecondi e risultando essere quasi un ordine di grandezza migliore rispetto alla piattaforma precedente. Infine, un WDM 1510/1588 nm è stato fabbricato utilizzando questo nuovo substrato, ottenendo un rapporto di estinzione di 19 dB per entrambe le lunghezze d'onda.

Parole chiave: Computazione quantistica; Sorgenti a singoli fotoni integrate; Ottica integrata; Microfabbricazione laser a femtosecondi; Wavelength division multiplexer.

Contents

Introduction

Quantum technologies have the potential to revolutionize the way we process information. This change touches several fields in science: quantum metrology and sensing, providing high-resolution measurements, quantum cryptography, applying protocols that ensure maximum secrecy in communications, to quantum simulation and quantum computing, that are capable of implementing and solving algorithms intractable for their classical counterparts. In recent years, scientists from all over the world have been putting countless efforts into developing these systems. First of all, it is necessary to find a physical system, which is scalable and engineerable, on which to implement this technology. The most mature technologies use superconducting circuits, trapped ions and photons. Among these, photons, thanks to their low decoherence and weak interaction with the environment, represent one of the most promising choices. Up to date, the most powerful quantum computer is based on photons [1]. Although this incredible achievement has been accomplished through bulk optics, to obtain a scalable, stable and portable platform it is necessary to switch to integrated optics. This fascinating approach uses waveguides to carry and manipulate information encoded in photon states. Multiple efforts are put into building a chip capable of performing full computational tasks, this means that a single chip must be able to generate complex photon input states, process them by interference in a unitary matrix and finally detect them through a detection system, all on one chip. However, for the accomplishment of such a system some problems have to be solved. One of these is the generation of input states that involve numerous photons. The generation of single photons through the effect of spontaneous parametric down conversion (SPDC) in nonlinear crystals, thanks to its stability and its relative ease of implementation, is so far the most widely used method for the realization of sources. However, due to their nature, they emit photons that are randomly distributed in time, making the generation of complex states more difficult. Fortunately, approaches such as the exploitation of heralding or post-selection mechanisms make these types of sources attractive. This thesis concerns the fabrication and characterization of an integrated wavelength division multiplexer, a key component for the implementation of a heralded integrated source. In particular, this device has been fabricated using the Femtosecond Laser Micromachining

(FLM) technique. This innovative technique proved to be very advantageous in several aspects. Compared to conventional lithographic processes, FLM is maskless, with fast prototyping capabilities and very low costs. In addition, an important advantage is the possibility to manufacture 3D circuits. This technique exploits the nonlinear absorption of the femtosecond laser to induce a permanent modification in the refractive index of the material. Thanks to this effect, FLM can be used on multiple transparent materials allowing the fabrication of hybrid devices, by maintaining low coupling losses between the various components. This thesis has been organized as follows: Chapter 1 introduces photonic quantum computing, showing the potentiality of this approach, how to implement it and introducing the boson sampling experiment. Chapter 2 covers femtosecond laser micromachining technique used to fabricate the devices shown in this thesis. Chapter 3 discusses the experimental setup and methods used for fabrication and characterization of the samples. Chapter 4 disclose the design and the operating principle of our final device. Chapter 5 shows the actual fabrication and characterization of the device. Finally, in Chapter 6 we developed a new photonic platform, based on femtosecond laser micromachining on a different glass substrate, for fabricating the integrated wavelength division multiplexer.

1 | Photonic Quantum Computing

In this chapter, a general overview of photonic quantum computing is presented. The chapter opens with a small introduction to quantum computing. Starting from the definition of a qubit and basic quantum gates, it generally presents the first algorithms that pushed the development of quantum computation in the last few decades. Then, a more specific outline of quantum computation using photons is given. In the second part of the chapter, the boson sampling model is described. The section also deals with two different approaches to implement it, namely bulk and integrated, showing state-of-the-art experiments. Finally a more specific insight into integrated sources and in particular the sources used to perform boson sampling is displayed.

1.1. Quantum Computing

In the late 1960s, it was thought that every computational problem could be solved with a Turing machine. This statement is summarised in the classic version of the Church-Turing's thesis: *Any algorithmic process can be simulated efficiently using a Turing machine* [2–4]. This thesis was never proven, but it held sway for many years and led to the evolution of the modern computers we know today. The tight constraint in this sentence lies in the word *"efficient"*. In 1982, Richard Feynman pointed out how complex it was to simulate quantum mechanical systems on classical computers and suggested that if these simulations were performed on quantum computers, the problem would be solved more efficiently [3–5]. Driven by this idea, in the years to come many people devised quantum algorithms in order to prove the real advantage of quantum computation, thus proving to solve tasks that are computationally hard for the classical counterpart. One of the first quantum algorithms is the Deutsch-Jozsa algorithm, devised by David Deutsch and Richard Jozsa in 1992, although it is of little practical interest, it demonstrates quantum exponential advantage [6]. Two years later Peter Shor demonstrated how quantum computation could efficiently solve two problems of enormous interest: the problem of finding the prime factors of an integer and the so-called "discrete logarithm" problem [7–9]. Further demonstrations of the power of quantum computing were brought by Lov Grover, who in 1995 formulated an algorithm that can speed up an unstructured search problem quadratically, the so-called quantum search algorithm [10]. After these theoretically based algorithms were discovered, research groups began to think how to implement the first quantum computer and thus actually demonstrate a quantum advantage on a physical platform. In the following years, some prototypes of quantum computers were developed, but not yet able to demonstrate the desired computing power. For the first time in history, in 2019 Google developed the first quantum processor capable of doing this, based on superconductor technology and operating at 53 qubits: the *Sycamore* quantum processor. Google announced that the processor was capable of solving a problem in 200 seconds, whereas a classical supercomputer would have taken 10,000 years, although IBM replied that a classical supercomputer would have taken 2.5 days [11, 12]. Despite the controversy between Google and IBM, the rapid growth of quantum computing increasingly highlights the possibility of quantum advantage even on physical devices. Indeed, in recent years other experiments has proven a computation advantage on task-driven algorithms. Among them, there is the experiment conducted by Yulin Wu *et al.*, that develop a programmable superconducting quantum processor based on 66 functional qubits: the *Zuchongzhi* [13]. Another important breakthrough has been achieved by Zhong *et al.* who succeeded in demonstrating quantum supremacy by developing a processor based no longer on superconducting elements, but on photons. In fact, this quantum computer, the *Jiuzhang* [14], processes up to 76 photons and was later improved in version 2.0 to 113 photons [1], making it 10 billion times faster than the previous version.

But what does quantum computing mean? Quantum computing refers to the way in which information is encoded and processed. In particular, it relies on the rules of quantum mechanics, by exploiting phenomena such as quantum interference, superposition principle and quantum entanglement. Quantum mechanics is a mathematical framework for the construction of these theories [3]. Hereafter, we introduce the general concepts at the basis of the quantum computation.

Just as the bit is the elementary unit of classical computation, the qubit (quantum bit) is its quantum counterpart. Unlike the classical bit, which can take the values 0 and 1, the qubit can assume more than one real value and can be written as a superposition of the two computational basis states:

$$|\psi\rangle = \alpha\,|0\rangle + \beta\,|1\rangle\,, \tag{1.1}$$

where α and β are complex numbers and holds the normalization condition $|\alpha|^2+|\beta|^2 = 1$. The qubit can exist in superposition only before being measured, once measured the wave function $|\psi\rangle$ collapses with probability $|\alpha|^2$ and $|\beta|^2$ into the basis states $|0\rangle$ and $|1\rangle$ respectively [15]. In a mathematical framework, the state of the qubit is a vector in the two-dimensional complex vector space, with special states $|0\rangle$ and $|1\rangle$ that form an orthonormal basis for this vector space. If the unit of quantum information has several states, d-levels state, we will speak of qudits [16].

The beauty of treating the qubit as an abstract mathematical object allows us to encode it on a variety of physical platforms. The qubit can be implemented in several ways: electrons (spin up and down), Josephson junctions (using the charge or the direction of the current), nuclear spins (up or down), ion traps (ground and excited state) and, as we will see in the next section, single photons [17, 18]. Some of these physical systems are listed in Table 1.1, illustrating the platform and the encoding methods.

System	Observable	Encoding
Single photon	Polarization Orbital angular momentum Number Time	Horizontal/Vertical Left/Right 0/1 Photons Early/Late
Continuous-variable fields	Quadratures	Amplitude -/Phase - squeezing
Josephson junction	Charge Current Energy	0/1 Cooper pair Clock -/Counter - clockwise Ground/Excited state
Quantum dot, Optical lattice, Nuclear spin	Spin	↑/↓
Electrons	Charge Spin	0/1 electrons ↑/↓
Non-abelian anyons	Topology	Braidings

Table 1.1: This table represents the most promising technologies adopted for the physical implementation of a qubit, illustrating the physical platforms and the encoding method. Table adapted from [17].

To realize a quantum computer, the qubit must be initializable, measurable, and manipulable so that a universal set of quantum logic gates can be built on top of it. It must also be a scalable technology, so that it can keep up with the computational power of state-of-the-art supercomputers. Just as logic gates form the basis of classical computation, so quantum logic gates form the basis of quantum computation. They are distinguished into single quantum gates and multiple quantum gates. Single quantum gates act on a single qubit, namely the information comes in from one input, is transformed and then exits the output. On the other hand, multiple quantum gates act on two or more qubit, which means that the output depends on the states of two or more qubits. Quantum computation has multiple single qubit gates, unlike the classical analogue, which has only two single gates (Identity gate and NOT gate). To represent logic gates at the quantum level, matrix notation is used and the only restriction is that the matrix U representing the gate must be unitary, i.e. $U^\dagger U = 1$, where $U^\dagger$ is the *adjoint* of U. Any matrix can be a logic gate, as long as it is unitary, which results in another difference to the classical analogue: quantum gates are reversible [3].

A set of universal logic gates is required to perform complex operations. For quantum computing, it has been shown that to build a set of universal gates it is sufficient to employ some one-qubit gates and at least one two-qubit gate [19, 20]. An example of a universal set of quantum gates can be composed by the following gates:

- The single qubit Hadamard gate, defined as:

  $$H = \frac{1}{\sqrt{2}} \begin{bmatrix} 1 & 1 \\ 1 & -1 \end{bmatrix}, \tag{1.2}$$

  this gate prepares a superposition state from a basis state, namely if the input state is $|0\rangle$ the output turns into $|+\rangle = \frac{1}{\sqrt{2}}(|0\rangle + |1\rangle)$ and if it is $|1\rangle$ it becomes $|-\rangle = \frac{1}{\sqrt{2}}(|0\rangle - |1\rangle)$.

- The $\pi/8$ phase shift gate:

  $$R = \begin{bmatrix} 1 & 0 \\ 0 & e^{i\frac{\pi}{4}} \end{bmatrix}, \tag{1.3}$$

  designed to change the quantum relative phase, without altering the amplitude.

- The controlled-NOT gate:

  $$CNOT = \begin{bmatrix} 1 & 0 & 0 & 0 \\ 0 & 1 & 0 & 0 \\ 0 & 0 & 0 & 1 \\ 0 & 0 & 1 & 0 \end{bmatrix}, \tag{1.4}$$

  a two-qubit gate devised for flip the state of a qubit (target) if the other qubit (control) is $|1\rangle$.

1.1.1. Photonic Based Quantum Computing

As we have briefly discussed above, quantum computing can be developed on different platforms. Among them, photonic platform represents a very promising solution. Indeed, photons can be an excellent choice for transporting information thanks to their low decoherence and weak interaction with the surrounding, keeping the information preserved for long-haul communication. In addition, due to these properties, photons can be used as carriers of quantum information without necessarily depending on the use of cryogenic temperatures or ultra-high vacuum.

In photonics, single quantum gates can be easily implemented through the use of waveplates, polarizers, beam splitters and phase shifters. For example, to realize the Hadamard gate a 22.5° oriented half waveplate is sufficient in case of polarization encoding [21] or can be implemented by using a beam splitter with a phase shifter if path encoding is used, while to realize the $\pi/8$ phase shift gate it is sufficient to change the phase to a qubit through delay lines or actively using thermal phase shifters [22]. On the other hand, multiple gates are very difficult to implement in quantum optics. While on the one side the characteristic of being weakly interacting with the surrounding makes the photon a very good qubit because it preserves the state, on the other side it is also its biggest drawback, since the implementation of a multiple gate requires the interaction between two or more photons. However, photon-photon interaction is only possible under strong nonlinearity regimes. Despite this, the development of a universal photonic processor requires the implementation of at least one multiple gate or, as mentioned before, the implementation of the CNOT gate. In 2001 Knill, Laflamme and Milburn showed that it is possible to achieve scalable quantum computing only by using single photons sources, detectors and linear optical circuits and so proving the implementation on a two-qubit gates without nonlinearity [23]. So, by exploiting an ancilla photons it is possible, using linear optical element, to realize a probabilistic CNOT gate, with a success probability of 1/9 [24]. However, the probability of success can be boosted by harnessing quantum teleportation [21]. Otherwise it is possible to build CNOT gates through nonlinear optical elements, for example by employing a strongly coupled quantum-dot-nanocavity system [25]. Recently, hybrid approaches have also been developed. Among these we find the use of two-photon absorbers together with the probabilistic CNOT gate. In this way, by exploiting the quantum Zeno effect, it is possible to avoid the failure mode of the probabilistic CNOT gate, by inhibiting the emission of two photons into one of the outputs. This increases the probability of success by 100% thus obtaining a deterministic CNOT gate [26].

Another two important aspects in quantum photonics, as in other platforms, are the losses and the scalability. As regard the losses, due to the no-cloning theorem, if a photon is lost, the information it contains is lost irreversibly. This feature still represent one of the major bottlenecks in photonics quantum computing. The other important feature for the implementation of quantum computation is the scalability. Bulk optics still use elements that are hardly scalable, while adopting an integrated approach this problem could be overcome. Integrated approach will be discussed in details in the next section.

A general scheme for a quantum photonic processor should encompass three main stages, as depicted in Figure 1.1. First of all, a single-photon source (SPS) is needed. The ideal source should emit one photon at a time, on demand, with a high generation rate. In addition, several sources must emit photons that are indistinguishable from each other, and for many applications it is required that they be emitted simultaneously [17]. At the moment, finding a source that satisfies all requirements keeping high performances is a difficult task. Typical single photon sources are differentiated into probabilistic and deterministic sources. Some of the deterministic source include quantum dots [27], trapped ions [28] and colour centres [29]. As regards probabilistic sources, they are typically obtained by exploiting nonlinear effects in optical materials. When an intense pump laser interacts with a $\chi^{(2)}$ (or $\chi^{(3)}$) material, one (or two) photons of angular frequency ω_p are annihilated and a pair of daughter photons is generated. The $\chi^{(2)}$ process is called spontaneous parametric-down conversion (SPDC), while the $\chi^{(3)}$ one is called spontaneous four wave mixing (SFWM). These processes produce photons randomly distributed over time, which is why they are probabilistic sources, but usually one photon of the pair (heralded photon) is used as a trigger to detect the other (heralded photon), so as to know where and when it was generated. Among the different methods, photon pairs can be generated either by SFWM in optical waveguides [30] and microdisks [31] or by SPDC in bulk crystals, semiconductors or microresonators [32]. Up to date, SPDC in nonlinear crystals represents the most employed method for generation of indistinguishable photon pairs.

The second stage is devised for manipulating the information carried by photons, making them interfere. Generally, this part involves the implementation of an arbitrary unitary matrix U, which can be implemented through the use of interferometric networks. So any discrete unitary operation can be achieved by connecting several linear optical components such as beam splitters and phase shifters. In order to make photon interfere, they must not undergo any modification in their path, so the system must be highly stable. Furthermore, as high computing powers require the use of multiple photons, the matrix needs to be implemented with scalable technologies. Initially the realization of the matrix U involved a series of bulk optical components, but were affected by problems of stability, scalability and implementation convenience. To overcome these problems, the technology has evolved to an integrated optics approach, based on a series of directional couplers and phase shifters designed to provide the U matrix. An ideal platform should feature low propagation losses, good coupling coefficient and the capability to integrate efficient phase shifters. Some of the most promising technological platforms are Silicon-on-insulator (SOI) [33], Silica on Silicon (SoS) [34], Silicon Nitride (Si_3N_4) [35], UV writing [36] and Femtosecond Laser Writing (FLW) [37].

Finally, a quantum photonic computer should be able to detect single photons in order to retrieve the information processed. A single photon detector (SPD) is a device that converts the energy of a single photon into an electrical signal. These devices require a high probability and reliability of detection. There are two types of photodetectors: those that are able to discriminate the number of photons detected, photon number resolving detectors (PNR), and those that detect at least one photon (non-PNR). Non-PNRs include single-photon avalanche photodiodes (SPADs) [38], quantum dots [39], negative feedback avalanche diodes (NFAD) [40] and superconducting nanowires (SNSPDs) [41], while PNRs include parallel SNSPDs [42], multiplexed SPADs [43], organic field-effect transistors [44] and transition-edge sensors [45].

Given a photonic processor, several quantum algorithms can be implemented. In this thesis, we will focus on boson sampling, which has been widely investigated in the last decades thanks to its ability to solve a problem otherwise intractable by classical computers in an efficient way, exploiting interference between photons.

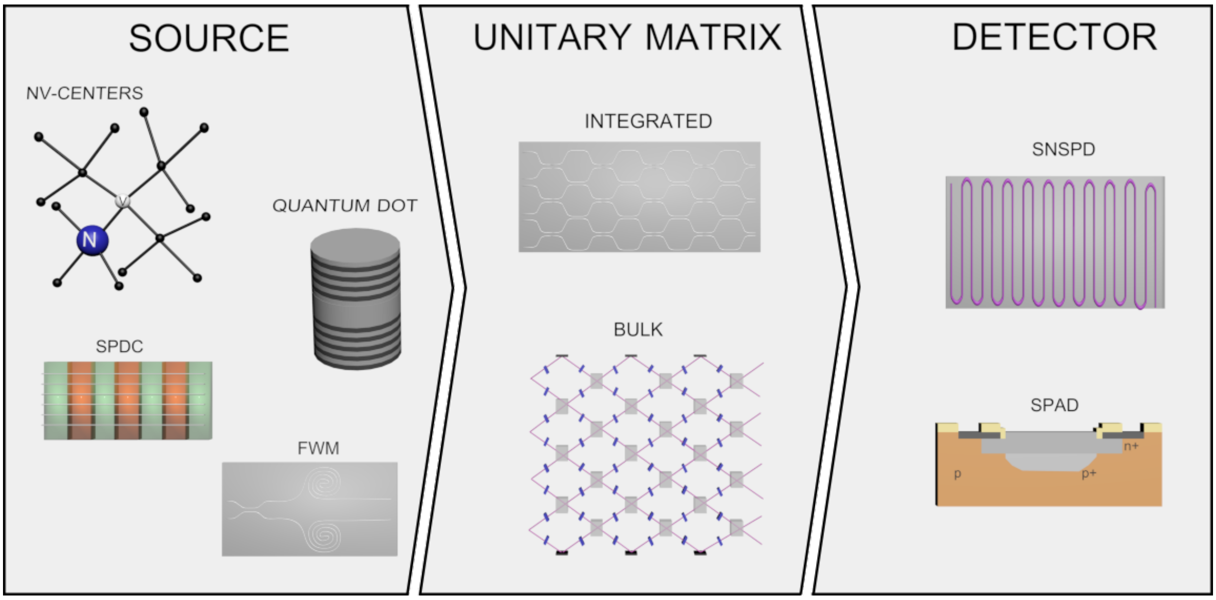

Figure 1.1: The three main stages that compose a photonic quantum processor. Several platforms for the implementation of each stage are show in this figure. As regards source, the main platforms involve NV-centers, Quantum Dot and generation via nonlinear effects such as SPDC and FWM. For the core of the photonic processor, in which the information is manipulated, two different approach are typically proposed: bulk and integrated approach. Finally, in the detector stage only SPADs and SNSPDs are reported. They represent the most mature technology for detecting single photons.

1.2. Boson Sampling

Boson sampling is a quantum computational model developed by Scott Aaronson and Alex Arkhipov (AA) that exploits the interference of noninteracting bosons to solve a classically intractable problem [46]. This model can be of practical interest in various applications such as calculating the vibronic spectra of molecules [47], simulations of spin Hamiltonians [48], or simulations of molecular quantum dynamics [49]. The method consists of sampling from the output distribution of indistinguishable bosons scattered from a linear interferometer, where the probability distribution depends on the permanent of complex matrices. Standard boson sampling, introduced by Aaronson and Arkhipov, is performed using photons. Photons are particularly suitable for performing boson sampling, since the model relies on noninteracting bosons and thus the problem of photon-photon interaction does not arise, bypassing one of the major problems in implementing a photonic quantum computer. This model does not show how to make a universal quantum computer, but it does demonstrate a clear advantage in solving an algorithm that would have been inefficient in the classical context, thus experimentally validating quantum supremacy.

As a matter of fact, it is known that the probability amplitudes for n-boson are proportional to the permanent of $n \times n$ matrix [50], similarly the amplitudes for n-fermion are proportional to the determinant. However, the former belongs to a $\#P$-complete class of computational complexity, while the latter to the P-class [51]. This means that for the computation of the permanent there is no algorithm that solves it in polynomial time. The best known classical algorithm is the Ryser's algorithm which solves it in $2^{n+1}n^2$ operations, e.g. if $n = 10$ it would mean $200,000$ operations, if $n = 30$, about 2 trillion. In 1996, Troyansky and Tishby devised a quantum algorithm to calculate the permanent exactly, but it was not efficient as an exponential number of samples would be needed for a good result [50]. Actually, in their seminal paper on boson sampling Aaronson and Arkhipov did not show how to calculate the permanent, but rather deals with sampling from a probability distribution, where this probability is proportional to the square of the permanent of a submatrix that describe the transition of photons from input to output. This is still a classically intractable problem, but, in the quantum framework, it is solvable almost-instantaneously due to the intrinsic nature of photons. So far, the best algorithm for boson sampling has been proposed by P.Clifford and R.Clifford, that unlike previous algorithms, adopts a number of innovative points, such us the exploitation of Laplace expansion, improving the time complexity of $O[n2^n{+}\text{poly}(m,n)]$ (see the article [52] for details). According to Clifford and Clifford, boson sampling starts to become unfeasible for classical computer processing around 50 photons [52].

Consider a system with n photons and m modes, the initial state can be described as follows:

$$|S\rangle = |s_1, s_2, ..., s_\text{m}\rangle\,, \tag{1.5}$$

where we have non-negative integers representing the number of photons in each mode. In each mode there can only be one or zero photons, which means it describes a no-collision state. This state enter to an m-mode linear optical interferometer that is described by a Haar-random unitary matrix U. Finally the output state is described as $|T\rangle = |t_1, t_2, ..., t_{\mathrm{m}}\rangle$. The transition probability between input and output state is defined as follows:

$$Pr[S \to T] = \frac{|Per(U_{\mathrm{S,T}})|^2}{s_1!...s_{\mathrm{m}}!t_1!...t_{\mathrm{m}}!}, \tag{1.6}$$

where $U_{\mathrm{S,T}}$ is a submatrix of U obtained by taking t_{i} copies of the i-th row of U and s_{i} copies of its j-th column.

The output photons are then measured by photon-counting detectors. The detectors will be placed on each output and must reliably measure the number of photons per output. In case the number of photons is much smaller than the number of modes, it is sufficient to use a photodetector that discriminates between a vacuum state and a photon, since if $m \gg n$ the probability that more photons come out of the same output is negligible. A representation of the process and the $U_{\mathrm{S,T}}$ submatrix is shown in Figure 1.2a.

From another viewpoint, we can consider boson sampling as the Hong-Ou-Mandel experiment [53], but with n=3, or more photons. In the Hong-Ou-Mandel experiment, if two indistinguishable photons (imagine photons of the same colour in Figure 1.2b) are injected, the output corresponds to the superposition of four states, depicted in Figure 1.2b, where two states cancels out by the opposite sign, namely the initial state $|1, 1\rangle$ evolves into

$$\frac{|2, 0\rangle - |0, 2\rangle}{\sqrt{2}}. \tag{1.7}$$

The amplitude of the basis state $|1, 1\rangle$ becomes 0, in fact the permanent

$$Per \begin{pmatrix} \frac{1}{\sqrt{2}} & \frac{1}{\sqrt{2}} \\ \frac{1}{\sqrt{2}} & -\frac{1}{\sqrt{2}} \end{pmatrix} = 0, \tag{1.8}$$

demonstrating destructive interference between the two paths [46].

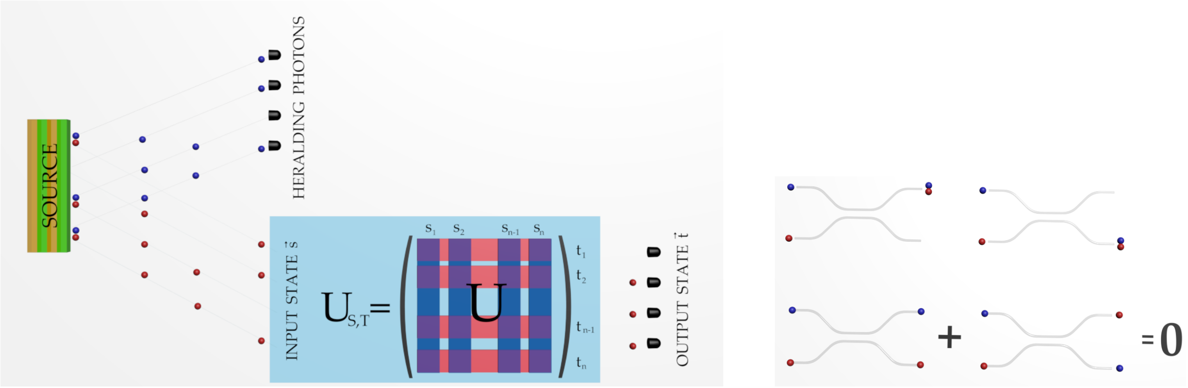

(a) Boson Sampling Submatrix

(b) Hong-Ou-Mandel possible outcomes

Figure 1.2: a) Representation of the input and output states and the generated submatrix. The probability of distribution is proportional to the permanent of the submatrix $U_{\mathrm{S,T}}$. The source emits a pair of photons in order to announce the input state by heralding photons. b) Four possible outcomes from the Hong-Ou-Mandel experiment. Since the photons are indistinguishable (imagine they have the same colour) the combinations at the bottom of the figure would cancel out, i.e. destructive interference. This would leave only the two results shown at the top of the figure.

Although there have been advances in the evolution of deterministic sources, such as quantum dots, achieving 50 or more photons generated simultaneously in a deterministic way is still far beyond the current capability of these sources. Up-to-date, the most widely used technique for generating single photons remains SPDC. This is because it guarantees high indistinguishability and an easy-to-implement setup. However, it is a probabilistic source and also requires low pump intensity to avoid multiple-photon generation. Given the spontaneous process, one never knows when the single photon will be generated. If we assume that the probability of generating a single photon is ϵ, the probability of generating n simultaneous photons is ϵ^n, which means that to prepare an input state with several photons one has to wait a very long time. For this reason, variants on classic boson sampling have been introduced to improve the probability of success of the experiment. Lund *et al.* devised the Scattershot Boson Sampling (SBS) [54]. This technique consists of placing more sources than the number of photons to be generated, placing one source at each input of the m-mode interferometer. For this setup the probability of generating one of the n-photon input configurations is $\epsilon^n(1-\epsilon)^{m-n}$ and the number of possible output configurations is $\binom{m}{n}$ thus obtaining a total generation rate equal to $\epsilon^n(1-\epsilon)^{m-n}\binom{m}{n}$ [54]. If $m \gg n$ an exponential improvement is obtained. To perform this, it is necessary to also sample the input state. This method is particularly suitable for SPDC, since by generating a pair of photons, namely signal and idler, one heralds the input port and the other enters the interferometer. Another variant is the so-called Gaussian Boson Sampling (GBS), developed by Hamilton *et al.* Instead of using single photons as input it exploits single-mode squeezed states and instead of calculating the permanent computes the Hafnian of a matrix, which always remains a problem in $\#P$ complexity class. In addition to containing information about the interferometer, the Hafnian contains information about the squeezing parameters and the phase of the Gaussian input states. This technique allows to exploit a higher pump intensity and a smaller sampling space since it does not require to sample input variables, but, unlike the original boson sampling proposed by Aaronson and Arkhipov where there is no phase relation between single photons, the GBS require phase control of the all photon number state in the single-mode squeezed states.

Two different optical approaches can be used to tackle the boson sampling problem: bulk and integrated. In the following, the state of the art of these two approaches and the advantages and disadvantages they provide are presented.

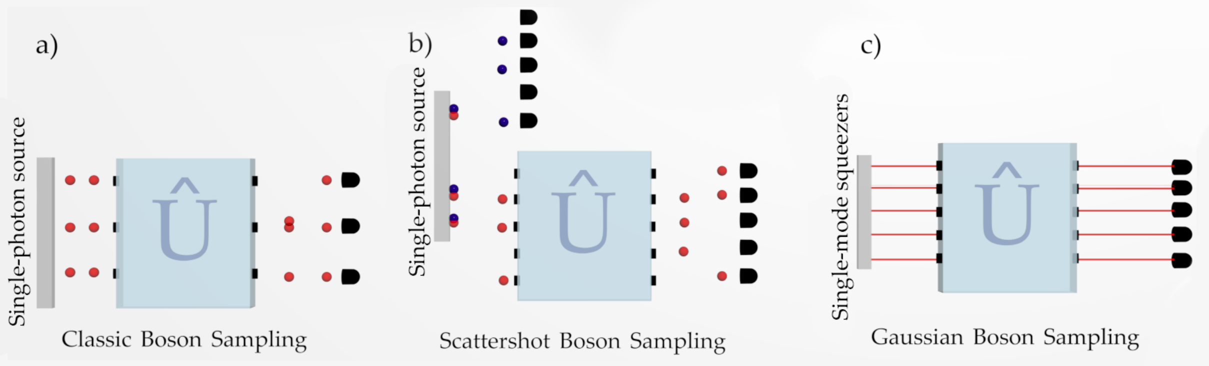

Figure 1.3: Boson sampling and its variants. a) Classic Boson Sampling, b) Scattershot Boson Sampling that exploit the heralding photon to increase the probability of possible input, c) Gaussian Boson Sampling, that exploit Gaussian state by single-mode squeezers. The red dots represent the single-photon input, the blue dots the heralding single-photons and the red lines the single-mode squeezed states.

1.2.1. Bulk Approach

Historically, all photonics experiments were carried out using a bulk approach. This consists of manipulating photons through optical components, such as mirrors, beamsplitters, polarizers and waveplates, which are therefore human-friendly in size, easily moved and positioned, and which generally involve low losses, if compared to the integrated approach. The mature knowledge of the technologies developed behind the bulk approach make it possible to perform significant experiments. Some of the most important results in boson sampling have been achieved through bulk optics. So far, the most important achievement, announced on 3 December 2020, is the Gaussian Boson Sampling performed by the GBS machine *Jiuzhang*, the photonic quantum computer developed by the University of Science and Technology of China (USTC) [14]. *Jiuzhang* is the first photonic quantum computer able to demonstrate quantum supremacy and, according to the USTC, is much more efficient than *Sycamore*, the quantum computer developed by Google [55]. This computer is capable of generating up to 76 photons simultaneously, which corresponds to an output space-state dimension of 10^{30} and thus a computing power $\sim 10^{14}$ times greater than the best supercomputer ever made [14]. In particular on *Jiuzhang* they performed GBS using threshold detectors, so the output distribution is related to a matrix function called Torontonian [56], and not to the Hafnian of classical GBS. However, it remains a problem in $\#P$, and so far the best algorithm takes two days to calculate a Torontonian involving 50 photons.

Zhong *et al*, for input generation, used 25 crystals of periodically poled potassium titanyl phosphate (PPKTP) to generate 25 two-mode squeezed states, which due to hybrid spatial-polarization encoding is equivalent to 50 single-mode squeezed states. These Gaussian states, controlled by a phase-locking system, are then sent into a 100×100 interferometer and finally detected by 100 superconducting nanowire single-photon detectors. A total of 300 beamsplitters and 75 mirrors were used to built the entire setup. A photograph depicting the entire setup is shown in Figure 1.4. The time cost of calculating the Torontonian scales exponentially as a function of the number of coincident photons generated. In 200 seconds, *Jiuzhang* generated $3,097,810$ events of 43 coincident photons and one of 76 coincident photons. It has been estimated that the *Fugaku* supercomputer would take 0.6 billion years to perform the same calculation [14].

A year later, the same research group achieved a new record. They developed version 2.0 of *Jiuzhang* [1]. Unlike the former, in the latter the GBS is programmable by tuning the phase of the input light. This new computer is capable of generating up to 113 photons click that pass through a 144-mode interferometer corresponding to a space-state dimension of 10^{43} and performing 10 billion times faster than the previous version.

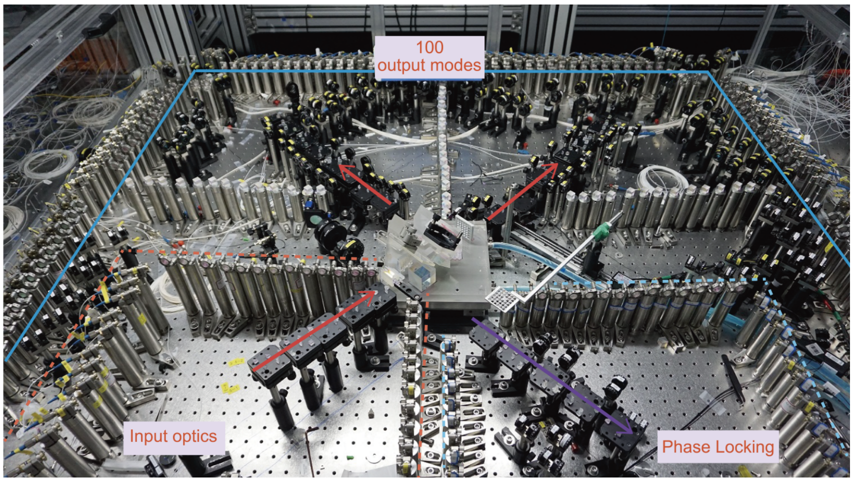

Figure 1.4: The photograph shows the entire setup. It occupies a total space of 3 square metres and consists of 25 two-mode squeezed states sources, in the bottom-left-corner, 25 phase-locking systems, in the bottom-right-corner, and multiple mirrors and polarizing beam splitters to achieve a total of 100 output modes, on the top part of the figure. Image taken from [14]

1.2.2. Integrated Approach

The incredible result achieved by Zhong et al. demonstrated quantum supremacy, breaking all records so far. However, it was seen that the size of the whole setup is not negligible. As the number of components increases in order to reach higher and higher computing powers, it becomes essential to have more compact and high-stable elements. The solution lies in the implementation of integrated optics, where several components can be built on one chip. Moreover, the *Jiuzhang* is a task-driven experiment, i.e. designed specifically to demonstrate quantum supremacy, having few other practical uses. While a more versatile approach can be achieved by making reconfigurable integrated circuits, i.e. circuits which, by means of for example thermal phase shifters, are able to change the U-matrix as desired just by varying the voltage from a driver. The foresight of reconfigurable integrated circuits lies in the fact that in addition to greatly reducing the size of the experiment, making it portable and scalable, multiple algorithms can be performed on it, going beyond the task-driven experiment and finding solutions to more practical tasks.

In order to build the integrated version of the multimode interferometer, waveguides are inscribed with different techniques on different platforms (see section 1.1.1) that can manipulate the beam while limiting losses as much as possible. In the integrated approach, beam splitters are replaced by directional couplers. A directional coupler consists in two waveguides placed close together that redistribute the light propagated by the coupling of the evanescent field.

Several boson sampling experiments have been conducted in the literature using integrated multimode interferometers: Crespi *et al.* [57] injected 3 simultaneous photons into a 5-mode interferometer built with FLW, Spring *et al.* [58] used 3 photons, but in a 6-mode interferometer built with UV writing, Zhong *et al.* [59] performed boson sampling with 5 photons in a 12-mode interferometer. However, these experiments carried out on integrated chips are still a long away from using the 50 photons needed for quantum advantage. All the above mentioned experiments were powered by a SPDC source bulk implemented. To further reduce the size and increase the number of sources, Paesani *et al.* [60] performed standard boson sampling, SBS and GBS by integrating not only the interferometer, but also the source, all fabricated on one chip, as shown in Figure 1.5. To perform SBS, the research team generated single photons through FWM using four spiral waveguides (to increase the nonlinear interaction path), then used two asymmetric Mach-Zehnder interferometers to filter the pump, signal and idler photons. Finally, four photons were heralded and four entered into a 12-mode interferometer. The photons are then detected by 16 SNSPDs, measuring for the SBS about four events per hour.

Although the numbers of photons used in these experiments are small, the use of an integrated approach opens the door to more and more complex experiments that will involve more and more photons. To achieve a fully integrated circuit also requires a photon generation stage that is also integrated, in fact on-chip photon generation lead to a series of advantages, but the implementation may arise some difficulties, as discussed in the following.

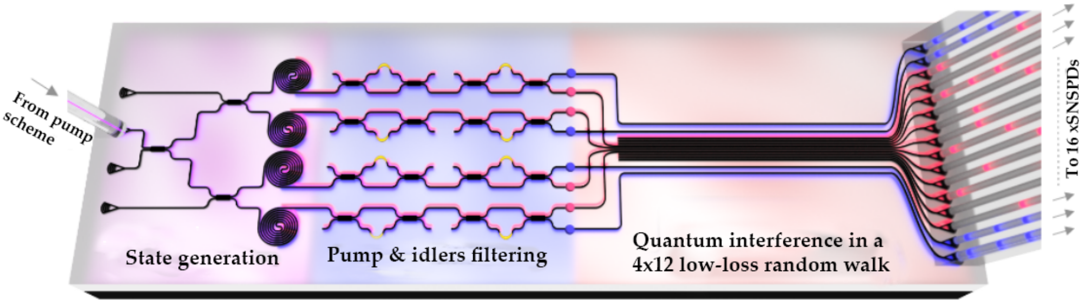

Figure 1.5: Diagram displaying the integrated boson sampling experiment developed by Paesani *et al.* Image taken from [60].

1.3. Integrated Sources

Single photon sources are the basis of quantum photonics technologies. This component is essential to provide quantum processors with information carriers and thus perform algorithms. Furthermore, if generation takes place on-chip, the coupling losses that are inevitable with the bulk approach are eliminated, and all the advantages of integrated technology such as miniaturisation, portability, scalability and stability are achieved.

As briefly mentioned in section 1.1.1 a source must have certain characteristics to be ideal. It must be able to deliver photons **on demand**, with a single-photon probability of 100% and a multiple-photon probability of 0%. The emitted photons must be **indistinguishable** to exploit quantum interference and the source must be **reproducible** so more sources can emit multiple indistinguishable photons simultaneously. Finally, it must have an appreciably high **repetition rate**.

To fully understand the characteristics of a single photon source, it is first necessary to define a statistical property of light, namely the second order correlation function, defined as follows:

$$g^{(2)}(\tau) = \frac{\langle E^{(-)}(t)E^{(-)}(t+\tau)E^{(+)}(t+\tau)E^{(+)}(t)\rangle}{\langle E^{(-)}(t)E^{(+)}(t)\rangle^2}, \tag{1.9}$$

where E is the electric field operator. If we consider a Hambury Brown Twiss interferometer, i.e. a device in which a stream of photons is divided equally by a 50:50 beam splitter and then two detectors measure the coincidences, diagram in Figure 1.6a, the $g^{(2)}(0)$ refers to the probability of detecting two photons simultaneously. The value of $g^{(2)}(0)$ differentiates three different regimes: sub-poissonian, poissonian and super-poissonian. In the case of $g^{(2)}(0)>1$ we are in the so-called super-poissonian regime, i.e. we are dealing with thermal light. In this case the emitted photons are less equally spaced than those emitted in coherent emission, so we speak of photon bunching. If $g^{(2)}(0)=1$ we are in the poissonian regime, i.e. with randomly spaced photon emission, it corresponds to coherent light emission, laser light. Finally, if $g^{(2)}(0)<1$ we are in the sub-poissonian regime, i.e. the emitted photons are more equally spaced than those emitted in coherent light, in this case we refer to photon antibunching. For an ideal single-photon source the cross-correlation $g^{(2)}(0)$ is equal to 0, i.e. the probability of emitting two or more photons at the same time is zero. This quantity generally determines the purity of a single-photon source, namely how close the real photons are to the ideals one, defined as $b = 1 - g^{(2)}(0)$ [61]. Another figure of merit that characterises a single photon source is indistinguishability. This quantity is measured by making the two photons bunch, i.e. with the Hong-Ou-Mandel experiment explained in 1.2. The two photons interfere with each other and if they are indistinguishable they will exit the same branch, resulting in no coincidence between the two detectors, giving rise to the classic dip in the coincidence graph, as shown in Figure 1.6c.

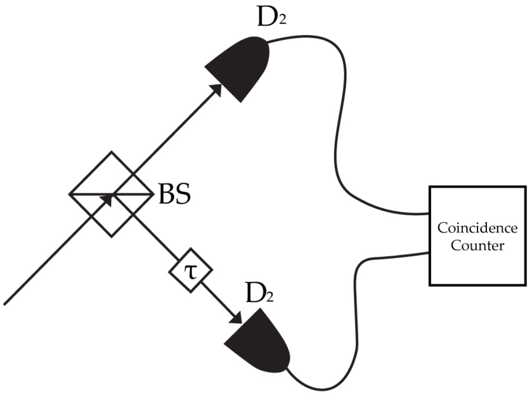

(a) HBT interferometer

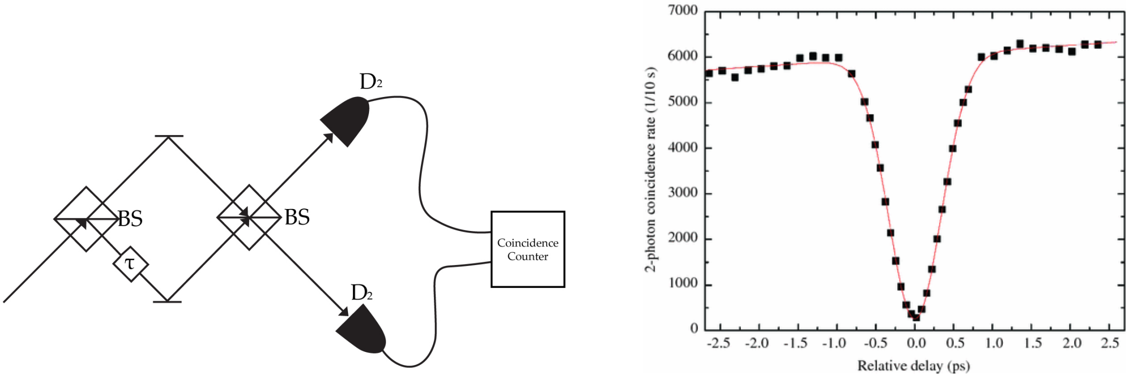

(b) HOM interferometer

(c) HOM dip

Figure 1.6: a) Hambury Brown Twiss interferometer. Setup used to measure the purity of a single-photon. The stream of photons goes through the 50:50 beam splitters (BS) and then are revealed by the two detectors D_1 and D_2, to measure the coincidences. For ideal single-photon at $\tau = 0$ there must be no coincidences. b) Hong-Ou-Mandel interferometer. The setup is similar to the HBT, but this setup is typically used to measure the indistinguishability between photons. The τ represent relative delay between two photons, if $\tau = 0$ the two photons enter the second BS at the same time. In section 1.2 the BS are depicted by DC (i.e. the integrated version). c) Typical graph representing the HOM dip. Image taken from [62].

The optimal source varies depending on the experiment to be performed. Probabilistic sources are easily implemented and ensure high indistinguishability between photons generated by the same crystal, nevertheless produce photons randomly distributed over time with a very low probability of generation. However, in an integrated approach, the pump beam is confined in a waveguide, so the light-matter interaction increases, thus resulting in enhanced brightness of the source

The generation probability of n-photon pairs varies depending on a term $|\lambda|^2$ proportional to the pump power as follows:

$$P(n) = \frac{1 - |\lambda|^2}{|\lambda|^{2n}}, \tag{1.10}$$

and the probability of create a $(n + 1)$ photon pairs is described as:

$$P(n + 1) = |\lambda|^2 P(n), \tag{1.11}$$

and so to avoid multiphoton generation, low pump power and low average single-pair production must be ensured. Furthermore, lowering the average single photon production lowers $g^{(2)}(0)$, thus increasing purity. This results in a trade-off between purity and brightness.

Probabilistic sources are based on nonlinear phenomena such as SPDC and FWM. SPDC is a second-order $\chi^{(2)}$ nonlinear phenomenon that occurs in non-centrosymmetric nonlinear materials. Through this phenomenon a more energetic pump photon is converted into a pair of less energetic photons, i.e. signal and idler. During the process, energy and momentum are conserved, as illustrated in Figure 1.7. Depending on the polarization of the three photons involved, three different types of SPDC can be distinguished: type 0, all photons have the same polarization, type I, signal and idler are orthogonal to the pump, and type II, where signal is orthogonal to the idler and one of the two is parallel to the pump photon. For some nonlinear crystal periodic poling ensures an additional knob for controlling the down-converted process and obtaining daughter photons with the desired wavelength and the right phase-matching properties. Periodic poling consists in periodically reverse the ferroelectric polarization of the nonlinear crystal, in order to induce a periodic inversion of the sign of the second order nonlinear coefficient. In this way, the crystal can be engineered to achieve a phase-matching condition that is otherwise unattainable [63].

In centrosymmetric materials, such as glass, which therefore do not present second-order $\chi^{(2)}$ nonlinear interactions, the dominant process is FWM. In fact, it is a third-order $\chi^{(3)}$ phenomenon, and involves four photons. Two pump photons are converted into two correlated photons, always known as signal and idler. Since it is a third-order phenomenon, the probability of generation is lower than SPDC and therefore requires long interaction paths in the material for efficient generation.

Several types of integrated probabilistic sources are reported in the literature, using SPDC in nonlinear waveguides [64] (Figure 1.8) or exploiting FWM in silicon photonics [60] (Figure 1.5) or glass waveguides [65]. Probabilistic sources can provide high-quality single photons with high levels of purity and high indistinguishability. In the state-of-the-art, purity levels >99% [66, 67] with indistinguishability >98% [66] can be found. For a more complete list of state-of-the-art purities, refer to review articles like [68–70]. However, a probabilistic source has a low emission probability, typically $p = 0.01-0.015$ per excitation pulse [71], and for some applications on-demand emission and high generation rate is required, for this reason several integrated deterministic sources have been developed.

An example of deterministic integrated source is NV centres in diamond, i.e. a nitrogen atom paired with a nearby vacancy. This structure can then be integrated directly on a chip with guides written into the diamond or, through the pick-and-place technique, it can be transferred to different substrates such as SiN or GaP creating hybrid devices [69, 72]. Other colour centres such as SiV [73], GeV [74] and SnV [75] can be used as single photon emitters. Since NV centres are not identical the scalability in the number of sources based on defects is limited, to compensate this a tuning of the spectrum can be carried out by applying an external electric field. High levels of purity are difficult to find for these sources. Among them we can find values of $g^{(2)}(0) < 0.3$ [76–78]. This is because NV-centres are very susceptible to external variations and are not very stable during the emission of subsequent photons. Due to this problem, scientific efforts have been made to develop deterministic sources based on quantum dots (QDs). This deterministic source is a three-dimensional nanostructure consisting of a semiconductor material with a low-band-gap integrated in a semiconductor with a high-band-gap. These objects are embedded in solid-state mediums and usually are composed by III-V elements, for example InGaAs in GaAs or InP in GaInP. They can be integrated into GaAs photonics chips [79], into SOI platforms [80] or in Si_3N_4 substrates [81]. A special feature of this emitter is that the wavelength of the emitted photon depends on the size of the quantum dot, due to quantum confinement. On the other hand, quantum dots are difficult to reproduce, it is tricky to create multiple identical QDs such that they emit indistinguishable photons, so fine tuning of a single emitter is necessary. Good purity values are generally found in the literature, for example InAs QD integrated in GaAs nanobeam waveguide shows a value of $g^{(2)}(0) = 0.05$ [82] or InGaAs in the same platform $g^{(2)}(0) = 0.006$ [83], with indistinguishability of 0.77. For more example, refer to review article [69]. Recently, has been realized a QD source emitting single photons at high purity, with a $g^{(2)}(0) = 0.0028 \pm 0.0012$ and a near-unity indistinguishability (0.9956 ± 0.0045). Although photons generated by the same QD show high levels of indistinguishability, the value drops considerably for photons generated by different QDs. One way therefore to obtain simultaneous multi-photon states would be to implement delay lines between photons from the same source.

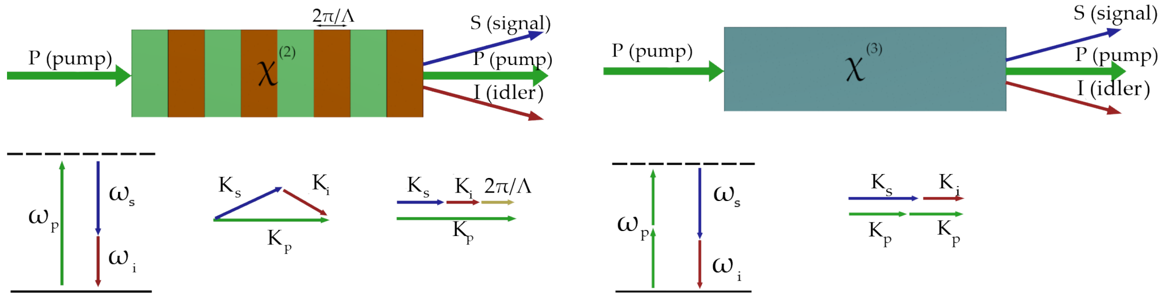

(a) Spontaneous Parametric Down Conversion. (b) Four Wave Mixing.

Figure 1.7: The two processes underlying probabilistic sources: a) SPDC, represented by a second-order $\chi^{(2)}$ nonlinear crystal, alternating two colours (to represent periodic poling). b) FWM, represented by a third-order $\chi^{(3)}$ nonlinear material, like glass. At the bottom of each figure, the energy conservation and momentum conservation are represented schematically. In the case of SPDC is also shown the quasi-phase matching condition (bottom right).

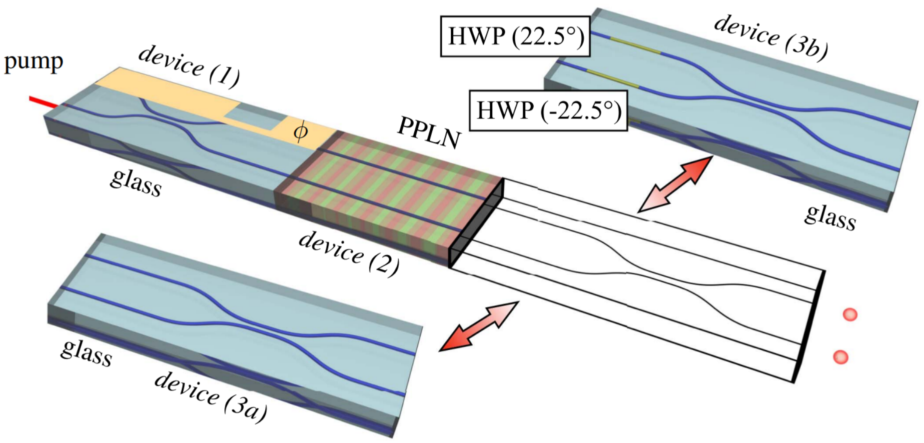

Figure 1.8: Integrated source of entangled photons, developed by Atzeni *et al.*. The source exploit SPDC by directly inscribing waveguides in a periodically poled lithium niobate (PPLN). Image taken from [64]

1.3.1. Heralded Integrated Sources for Boson Sampling

Once an overview of the possible single-photon sources has been given, it is necessary to identify the source that best suits the boson sampling experiment. In order to perform boson sampling, it is necessary that all generated photons have high purity and are indistinguishable, otherwise the phenomenon of quantum interference would not occur. Moreover, it is desirable to have a sufficiently high generation rate of photons in order not to have to wait too long time to prepare an array of simultaneous single photons, since the time increase exponentially with the number of simultaneous photons.

Probabilistic sources, given their characteristics, are still the workhorse for the generation of single photons. However, the need for more and more complex input states goes against the characteristic of generating photons randomly distributed in time. One solution is represented by the heralded integrated sources, which announce the input state thanks to twin photons. Thanks to this solution, scattershot boson sampling can be implemented, exponentially increasing the event rate. Both SPDC and FWM generate a pair of photons in order to herald the input photon. The waveguide-based generation of single-photon permit, with multiplexed parallel sources, to prepare complex input states. However, although they are inscribed in the same crystal to ensure high indistinguishability, between the different waveguides there may be some differences and thus compromise this property. These sources can also be easily integrated and assembled into photonic chips. Unfortunately, these two phenomena, being probabilistic, cannot generate photons on command and single photons are rarely generated, to give an idea usually about 1 pair of single photons is generated every 10^6 pump photons [84]. Therefore the probability of obtaining n simultaneous photons decrease exponentially with n and hence inversely increase the time [85]. Due to this reason, it is necessary to build a chip with very low losses so as not to lose the few pairs of photons generated and then waiting too long. This aspect will be discussed further in section 6.1. In general, it is possible to increase the number of generated pairs by increasing the pump power, but at the same time increases the probability of multi-photon generation. Using low pump power, $g^{(2)}(0)$ purities of around 10^{-3} can be achieved. One particularly important thing to take into account with heralded sources is the propagation losses. In fact, it may happen that a heralded photon is lost, resulting in a null detection and therefore an unheralded photon will be emitted, disturbing the photon number distribution. One way to overcome this problem is to open the channels of the heralded photons only in case of a trigger of a herald photon.

In the integrated approach, in which the nonlinear effects for photon-pairs generation occur in a waveguide, pump, signal and idler photons propagate in the same spatial mode. The pump photons must be removed from the waveguides containing the signal and idler photons because as the pump photons are orders of magnitude larger than the signal and idler, they would instantly saturate the detectors. Therefore a long-pass filter to cut off the pump photons is required. Filtering the pump requires an extinction of about 100 dB [86] and implementing such an integrated filter is a tricky task. Nowadays in integrated photonics some methods to filter the pump are ring resonators [86], Bragg gratings [86], asymmetric Mach-Zender interferometers [60], Fabry-Perot cavities [87], high/anti-reflective (HR/AR) coatings [88] as illustrated in Figure 1.9 or more recently filter based on lateral leakage as in the work of Boes *et al.* have been developed [89].

After this, it remains to separate the idler photons from the signal photons, so as to use the idler photon as a trigger to announce where and when the signal photon has been generated. In the state of the art there are several solutions, such as the use of wavelength division multiplexing (WDM) [88], as will be extensively explained in section 4.3, or asymmetric Mach-Zender interferometers, as in the work of Paesani Figure 1.5 *et al* [60].

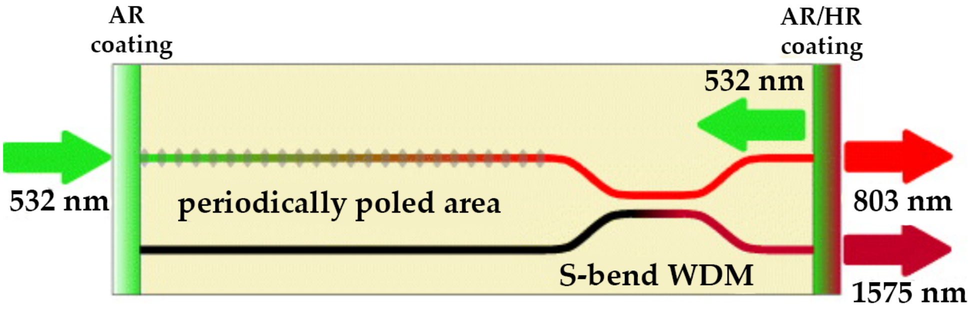

Figure 1.9: Integrated source in titanium-indiffused periodically poled Z-cut lithium niobate waveguides for heralded single photons. Signal and idler are separated by a WDM and filtered from the pump photons through high-reflection (HR) and anti-reflection (AR) coatings. Image taken from [88].

2 | Femtosecond Laser Micromachining

In this chapter a general overview about Femtosecond Laser Micromachining (FLM) is discussed. First, a brief introduction about the technique is presented, comparing it with other known state-of-the-art techniques and listing its advantages and disadvantages. Then the physical process behind this technique will be explained in section 2.1. Finally, in section 2.2 a subset of parameters that can be tuned during waveguide fabrication will be illustrated.

Introduction

It was in 1996 when Davis et al. first exploited a femtosecond laser to write waveguides in a glass [90]. In fact femtosecond laser pulses are capable of releasing enough energy, in the order of $10\,\mathrm{TW/cm^2}$, to produce nonlinear absorption effects in the dielectric material, so as to produce a permanent and localized refractive index increase. One of the main advantages of FLM lies in the fact that, relying on nonlinear absorption, only the volume portion where the laser is focused undergoes modification, as shown in the picture 2.1a. Aided by a computer-controlled motion system, the sample can be translated with respect to the focal point of the laser beam, allowing one to induce material modifications along an arbitrary three-dimensional path. It follows that it is possible to write optical circuits with 3D geometry, thus overcoming the planar writing limited imposed by photolithography. Furthermore, unlike photolithography, FLM is a one-step procedure, is maskless, does not require the use of clean room and expensive fabrication setup, thus making it a fast and easy to implement procedure and so a valid option for rapid prototyping of photonic integrated circuits. Additionally, relying on nonlinear interaction, it is theoretically possible to write on any transparent medium. However the refractive index contrast Δn that FLM can induce is in the order of 10^{-3}, lower than the one achievable with standard planar lithographic process in materials such as silicon [91] and silicon nitride [92]. The higher is the index contrast, the higher is the mode confinement and the lower is the achievable minimum bending radius at negligible bending losses. It follows that a higher index contrast leads to higher density of components per unit of length and a higher degree of miniaturization.

Up to now we have been talking about how to use this technology for the fabrication of waveguides for photonic integrated circuits application, but in 2001 Marcinkevicius et al. demonstrated that, by increasing the writing power, the laser-material interaction can lead to the formation of nanogratings. These structures can be then etched in an hydrofluoric acid solution to create microchannels, that find applications in optofluidics [93]. This highlights the versatility of FLM.

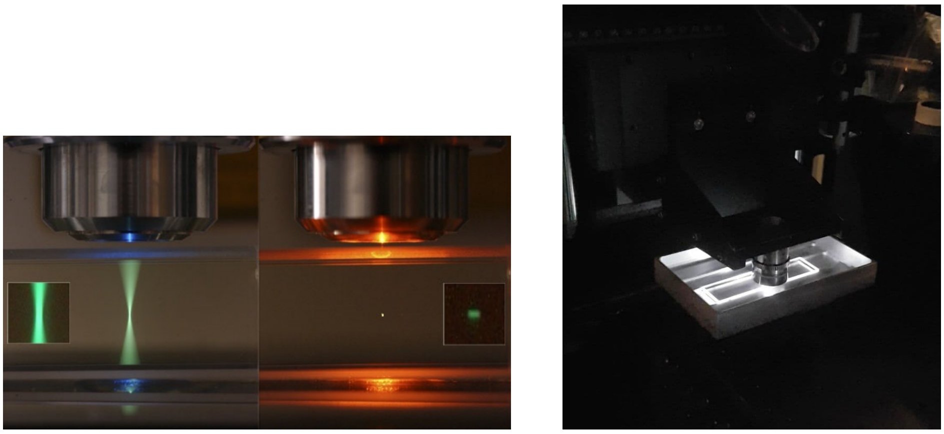

(a) (b)

Figure 2.1: a) Difference between linear absorption (left) and nonlinear absorption (right). In the latter, it can be seen that absorption, and therefore material modification, only occurs in the focal volume. Figure by UC Berkeley. b) Waveguide writing in glass substrate using the FLM technique.

2.1. Femtosecond Laser-Material Interaction

The mechanism behind the FLM can be summarised in three steps: firstly, there is the formation of the free-electron plasma, after that in a time interval of about ten picoseconds the energy is released into the lattice, this phenomenon is known as relaxation and finally the modification of the material takes place.

2.1.1. Free-electron Plasma Formation

Femtosecond lasers generally use wavelengths in the infrared or visible range, therefore they have insufficient photon energy to be linearly absorbed by the glass (the highest visible photon has 3 eV while glass energy gap is about 5 eV). It follows that nonlinear absorption is required to promote an electron from the valence to the conduction band. In particular, two phenomena occur: nonlinear photoionization and avalanche photoionization. These processes are represented in Figure 2.2.

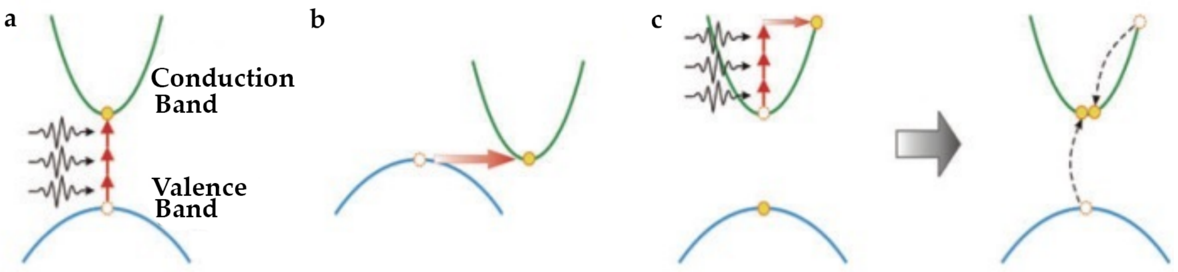

Figure 2.2: Nonlinear photoionization processes driving the FLM. a) Multiphoton ionization, b) tunnelling photoionization and c) avalanche photoionization including free carrier absorption and impact ionization. Image taken from [37].

Nonlinear Photoionization

It is possible to distinguish between two different processes in the nonlinear photoionization: multiphoton absorption and tunnelling photoionization. The former usually occurs at low laser intensities and high frequencies (but still less than the frequency of a single photon absorption). In order for multiphoton absorption to occur, several m photons must be absorbed simultaneously so that $mh\nu > E_{\mathrm{g}}$ where ν is the photon frequency and E_{g} is the energy band gap of the material. On the other hand if we are in a regime of high intensity and low frequency, tunnelling photoionization comes into play. In this case the strong field is able to distort the energy bands, reducing the potential barrier between the valence and the conduction band, so a direct band to band transition is then possible. The transition between these two regimes is described by the Keildysh parameter [94]:

$$\gamma = \frac{2\pi\nu}{e}\sqrt{\frac{m_{\mathrm{e}} c n \epsilon_0 E_{\mathrm{g}}}{I}} \tag{2.1}$$

where ν is the laser frequency, I the laser intensity, E_{g} the energy band gap of the material, e the electron charge, m_{e} the effective electron mass, c the speed of light in vacuum, n the refractive index and ϵ_0 the vacuum permittivity.

If $\gamma >> (<<) 1.5$ multiphoton absorption (tunnelling photoionization) takes place. Considering standard processing parameters in the formula (2.1) it turns out that $\gamma \sim 1$ and thus both phenomena should be taken into account.

Avalanche Photoionization

Once an electron is promoted in the conduction band, it can linearly absorb impinging photons in a process called inverse bremsstrahlung and acquire an energy greater than the band gap. The accelerated electrons can now transfer their energy by collision to an electron in the valence band, promoting it in the conduction band. At this stage, we have two electrons in the conduction band. In turn, these two electrons can undergo the same phenomenon and so on, as long as the laser is active, creating an avalanche of electrons. This process is called avalanche photoionization. As the process goes on, the density of free electrons increases until the laser frequency approaches the plasma frequency $\omega_\mathrm{p} = \sqrt{n_\mathrm{e}e^2/m_\mathrm{e}\epsilon_0}$, where n_e is the electron density. At this point, around n_e=10^{21} cm^{-3} [37], the electron plasma becomes strongly absorbing [95] and only a small percentage of the laser will be reflected. To trigger the avalanche photoionization a seed electron is required. Usually, these seed electrons are given by impurities ($\sim$1 electron per focal volume [96]), but in FLM they are given by the nonlinear photoionization, thus making it a deterministic process and therefore a controlled and reproducible technique [97].

One thing worth noting is that nonlinear photoionization has a threshold intensity for optical breakdown that is highly dependent on the bandgap of the materials. Therefore, if it were the only process going on, FLM would be specific only to certain materials. However avalanche photoionization is also present in the absorption process and is linearly dependent on laser intensity [98]. The sum of these two phenomena allows the optical breakdown threshold to be reached with little dependence on the band gap of the material, making FLM a technology that can be use on a wide range of materials [37].

2.1.2. Relaxation and Modification

Once the hot electron plasma has been created, energy is released to the lattice within a period of about 10 ps [99]. A further advantage of using subpisecond pulses is that absorption and relaxation are two temporally separate phenomena, the heat transfer occurs when the laser is already gone and this allows one to induce a more precise and confined modification. The mechanism behind the material change is not trivial to explain and depends on the laser-matter interaction. However, it has been seen that by changing the writing parameters, such as laser power, scan speed, pulse duration or by changing the dielectric material, different types of modifications can take place. In particular, for glass substrates, these modifications can be divided into three regimes [100]:

- **Smooth change in the refractive index**: With low-energy pulses, the change occurs isotropically, which is ideal for low-loss optical waveguides. The main mechanism behind the material modification is rapid quenching of the melted glass at the focal point, which has been shown to increase the density of the glass and consequently also increase the refractive index [101]. Other mechanisms can play an important role in the modification of the substrate, such as colour centres formation [102] or ion migration [103], and each of these contributes differently depending on the material used.

- **Birefringent Refractive Index Change**: As the deposited energy increases, a change in birefringence can be observed, due to the formation of period nanostructures by means of the interference of the laser with the electron plasma. In addition, layers with periodically different refractive indices perpendicular to the polarization of the laser are formed, and these, once etched with HF, can form microchannels that find applications in microfluidic [104].
- **Void Formation**: For high-energy pulses, after the transfer of energy from electron to lattice, a shockwave is created that can form a hole in the material [105]. These voids can be used for 3D memories [106] or photonic bandgap materials [107].

2.2. Fabrication Parameters

So far we have only discussed the effects of varying the deposited energy, but for writing and optimising optical waveguides it is necessary to consider other parameters as well.

2.2.1. Focusing

The incident laser is focused into the transparent material to reach a small micrometer spot size and trigger nonlinear absorption. If we consider linear propagation of a Gaussian beam in a dielectric of refractive index n and we neglect aberrations, we can derive the spatial intensity profile of the spot in terms of the diffraction-limited minimum waist radius w_0 (1/2 of the spot size) and the Rayleigh range z_0 (1/2 the depth of focus) as follows:

$$w_0 = \frac{M^2\lambda}{\pi NA} \tag{2.2}$$

$$z_0 = \frac{M^2\lambda n}{\pi NA^2} \tag{2.3}$$

where M^2 is the Gaussian beam propagation factor, λ the wavelength of the radiation and NA the objective numerical aperture. However, there are also chromatic and spherical aberrations that can cause distortions in the laser beam and thus alter the intensity distribution. Microscope objectives are usually used to overcome this problem. In particular, when writing in a substrate with a refractive index n, spherical aberrations are induced by the difference in the refractive index at the air-substrate interface, which results in a strong dependence in the writing depth. This phenomenon mostly affects high NA objectives. To mitigate this, water- or oil-immersion objectives are usually employed. As the ratio w_0/z_0 (see equations (2.2) and (2.3) as reference) is proportional to NA/n, it follows that the shape of the spot can be varied accordingly to the numerical aperture of the focusing system (i.e. a large NA should be employed in order to have more circular spots). In waveguide fabrication the refractive index of the substrate, since glass-based substrates are adopted, is usually around 1.5 while the NA is typically $<$1.5, thus leading to an axially elliptical spot.

In case of high electric fields, the nonlinear refractive index n_2 of the dielectric get involved. If the power exceeds the self-focusing value P_c=$3.77\lambda^2/8\pi n_0 n_2$ Kerr-effects takes place and the pulse is further focused. The increased intensity is able to nonlinear ionized the material to produce free electron plasma which acts as a diverging lens. The Kerr-lens combined with plasma defocusing leads to filamentary propagation and thus an axially stretched modification [37].

2.2.2. Repetition Rate

Varying the number of pulses per second, i.e. the repetition rate, means greatly change the properties of the guide. In particular two regimes can be identified [108]: one where the time elapsed between two pulses is greater than the heat diffusion time (around $1\,\mu s$) and one where it is smaller. In a regime of low repetition rate $<$250 kHz the pulses are independent of each other, no thermal build-up takes place during the laser-material interaction. In single pulse interaction the shape of the modification is similar to the shape of the focus, so they have an asymmetrical cross-section, which is not optimal for waveguides fabrication [109]. Another disadvantage encountered when operating in this regime is the low scanning speed (a few μm/s) and consequently long fabrication times. Nevertheless, this regime is widely used due to the availability of regeneratively amplified Ti:Sapphire lasers, which provide highly energetic pulses at low repetition rate.

On the other hand, by increasing the repetition rate up to some MHz, the next pulse arrives while heat diffusion is still taking place, so thermal accumulation phenomena occur, as illustrated in the Figure 2.3 at 1 MHz. In this regime, since high repetition rates are associated with low energies per pulse, tight focusing, and thus the use of large NA, is required to reach the nonlinear absorption. High repetition rates enable more uniform and symmetrical modification, increasing the quality of the waveguides; in addition, scanning speeds can be increased up to 50 – 100 mm/s, reducing fabrication time.

Between 100 kHz and some MHz there is also an intermediate regime in which the positive effects of both previous regimes add up, i.e. pulses energetic enough not to require special focusing and thermal accumulation phenomena. In this regime, it is possible to produce waveguides with higher refractive index contrast, with uniform and symmetrical profile and low losses, while maintaining high scanning speeds. Nowadays, the lasers used in this regime are Yb-based laser system operating at around 1 MHz with pulses of a few μJ.

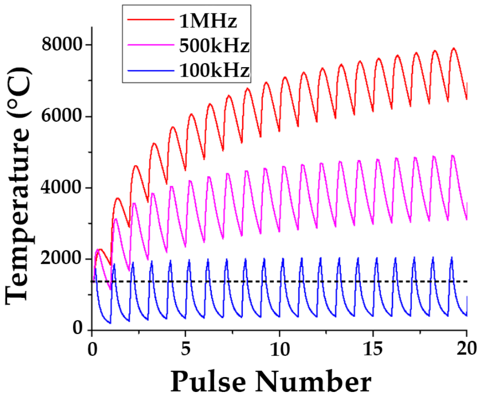

Figure 2.3: Effect of the repetition rate on the thermal accumulation. At 100 kHz no thermal accumulation occur, at 1 MHz the cumulative heating take place and at 500 kHz an intermediate regime where thermal accumulation is present, but still no special focusing is required. Image taken from [110].

2.2.3. Writing Geometry

The writing configuration describes the translation between the beam and the substrate. There are two different writing configurations for writing inside the sample: longitudinal and transversal. Panel a of the Figure 2.4 shows the **longitudinal configuration**; in this writing geometry the sample is translated along the direction of propagation of the laser beam and therefore waveguides with symmetrical cross-sections will be obtained, since they follow the transverse symmetry of the Gaussian intensity profile. The disadvantage of this geometry lies in the fact that the length of the waveguides is limited by the working distance of the lens, which for high numerical apertures is only a few mm.

For this reason, the most commonly used geometry is the **transversal configuration** (shown in the panel b of the Figure 2.4). In this mode the sample is translated perpendicularly to the laser beam and therefore the whole 3D space inside the sample can be fully employed. Indeed, the sample thickness is usually smaller than the working distance (of about few mm) of the lens. The disadvantage of using this configuration is that the modification will take place in an asymmetrical way, tending to be elliptical in the axial direction, due to the ratio of waist-radius w_0 (2.2) to Rayleigh range z_0 (2.3), which is usually less than 1. An elliptical modification supports elliptical modes which will therefore result in higher coupling losses and birefringence, a property that may or may not be desired depending on the application. To overcome this problem, beam shaping and multiscan techniques can be exploited [111].

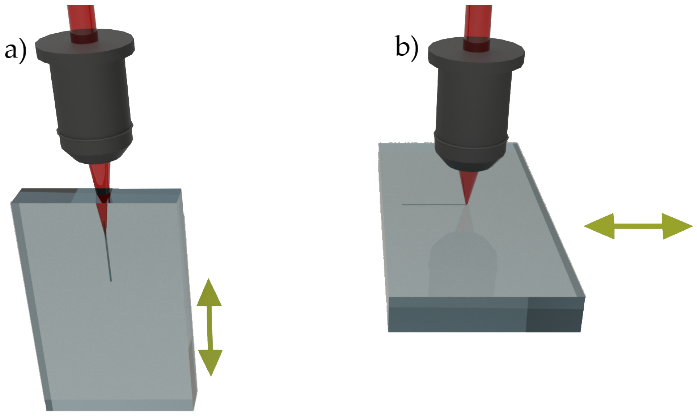

Figure 2.4: Two different writing geometries. The longitudinal configuration a), where the sample is translated along the direction of propagation of the laser, and the transversal one b), where the sample is translated in the plane perpendicular to the beam.

2.2.4. Other Parameters

In addition to the parameters listed above, other parameters can be adjusted to optimise the waveguide. For example, varying the writing speed changes the density of energy deposited in the material, while increasing the number of scans may lead to an increase of the index contrast and thus a higher mode confinement. Other parameters such as writing direction [112], laser polarization [113] and laser wavelength [114] can change the properties of the guide.

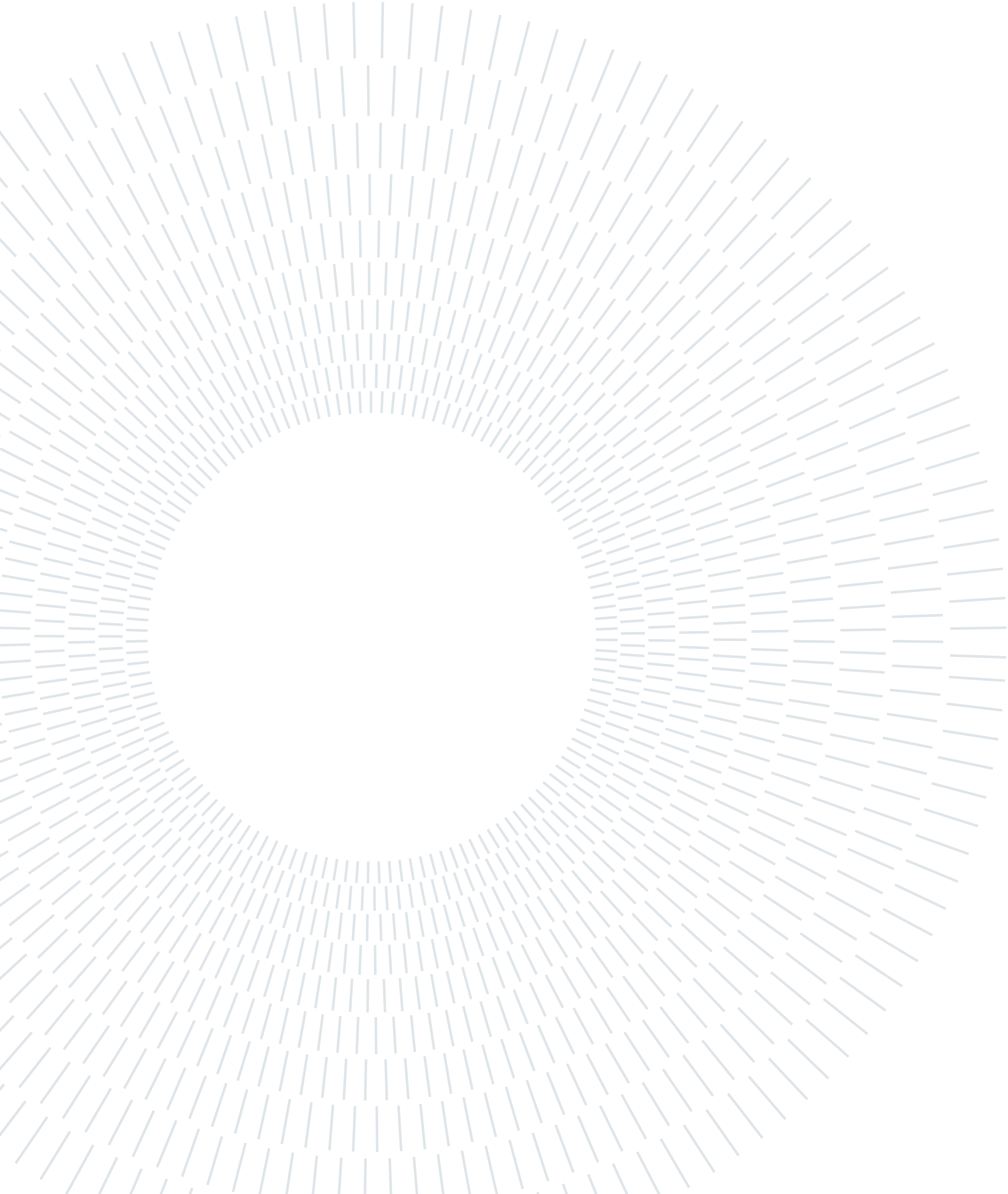

3 | Experimental Setup and Methods

The entire setup e methods used for the fabrication and characterization of the optical devices are discussed in this chapter. Section 3.1 explains the fabrication procedure by describing the writing setup and the subsequent steps to obtain a sample ready for characterization, i.e. annealing, cut and polish. Then in section 3.2 the methods and setups for the characterization of the optical circuits including microscope analysis, device coupling, mode analysis and loss measurement will be disclosed in detail.

3.1. Fabrication Process

The fabrication of an optical device requires several steps. In fact, after the inscription of the optical circuits by means of a femtosecond laser (Section 3.1.1), the sample is then annealed (see Section 3.1.2) and finally polished as described in Section 3.1.3.

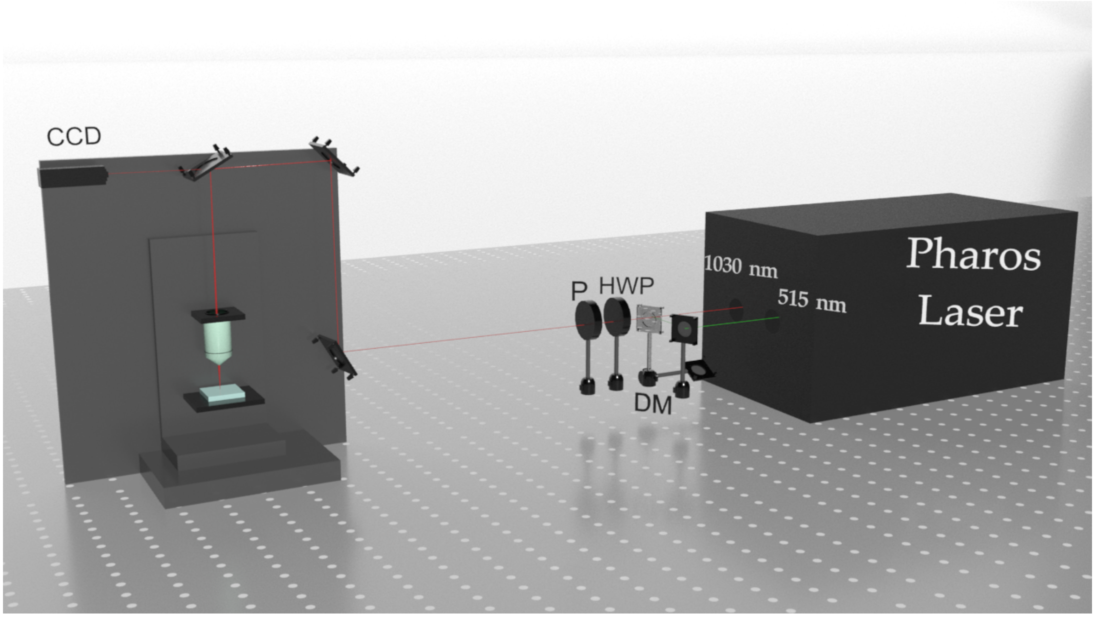

Figure 3.1: Schematic of the fabrication setup. The femtosecond laser beam at 1030 nm emitted by Pharos is steered into a half-wave plate (HWP) and then into a polarizer (P). Through the use of dielectric mirrors (DM), the beam is directed into the objective, which focuses the laser beam into the sample. To exploit the second harmonic, a series of flip mirrors is used to direct the beam along the optical path, before entering the half-wave plate. Finally, a CCD camera is mounted behind a dielectric mirror in order to find the focus on the surface of the sample.

3.1.1. Writing Setup

The schematic of the setup used to fabricate the optical circuits shown in this thesis is illustrated in Figure 3.1. A femtosecond pulsed laser beam at 1030 nm, through a system of mirrors, is directed into the microscope objective which will focus the laser beam inside the substrate. The latter is glued on top of a support fixed to a three dimensional linear motion system, driven by the computer via the software A3200 CNC. Thanks to a set of mirrors and mirror holders mounted on the motion system, it is possible to achieve precise alignment of the laser beam. In addition, a CCD camera is mounted in the optical path behind a mirror to collect the collimated back-reflection in order to focus, with micrometric precision, the laser on the surface of the substrate and thus make the fabrication process reproducible. A range of objective ranging from 0.3 to 1.4 (oil immersion) numerical aperture is available to optimize fabrication. The laser power is controlled by both software of the laser or by a polarizer and a half-wave plate (controllable by software A3200 CNC) placed along the laser path. This allows the irradiation conditions to be varied during writing. The laser system is equipped with a second harmonic stage, giving a choice of whether to fabricate at the fundamental wavelength (1030 nm) or at its second harmonic (515 nm). An internal shutter synchronised with the motion stage allows the laser to be blocked or opened quickly during the fabrication process.

The laser source

The laser source used in this thesis is the PHAROS commercial model of LIGHT CONVERSION. The laser system is based on laser diodes pumping Yb medium ($KY(WO_4)_2$ doped with Ytterbium at 5% concentration) and its emission wavelength is at 1030 nm. This laser is able to reach a maximum average power of 10 W for the fundamental wavelength and a maximum average power of 3 W for the second harmonic at 515 nm. The versatility of this model lies in the fact that through the software it is possible to change the parameters as pulse duration (from some ps to 190 fs) and repetition rate (from single shot to 1 MHz). In addition, the beam can be spatially manipulated using a liquid crystal Spatial Light Modulator (LCOS-SLM, Hamamatsu). In particular, for the fabrication of the optical circuits disclosed in this thesis, the parameters are the following: pulse duration of 172 fs, central wavelength of 1030 nm with spectral FWHM of 12 nm and M^2 quality factor of 1.1.

The motion system

The specimen is glued on top of a sophisticated motion stage (Aerotech ABL1500) equipped with air bearings and linear brushless electric motors that make it move with an accuracy of 100 nm in a smooth and linear manner and translate at a speed up to 100 mm/s. It has a translation movement of 10 cm x 15 cm in the plane and 5 cm in the vertical direction. There are also optical encoders to monitor the position of the stages in real time, with an accuracy of 1 nm. Specimen holders are also designed for in-water fabrication. Slide movements are programmable via software by A3200 CNC programme, using G-Code language.

3.1.2. Annealing

During fabrication, the laser-material interaction in the focal volume locally heats the substrate to temperatures of thousands of degrees Celsius [115]. After the laser is moved away, the material quickly returns to room temperature. This process and the resulting thermal shock induces internal stresses in the material, thus making it more brittle. After fabrication, a thermal annealing is usually performed in order to relax the internal stresses. Therefore annealing consists of a thermal process that serves to reduce the internal stresses in the glass through rapid heating and then gradual cooling of the sample. In amorphous materials, as the glasses employed in this thesis, the breaking of chemical bonds occurs over a range of temperature. It follows that a melting temperature is not defined, and the glass gradually softens as it heats.

To better explain the behaviour of glass, it is convenient to introduce some important points related to the viscosity of the material [116]. At a viscosity of about 10^{14} Poise, the glass reaches the **strain point** where internal stress relaxes in a few hours, under that temperature permanent strain cannot be introduced. Increasing the temperature the glass reaches the **annealing point**, which corresponds to about 10^{13} Poise, where internal stresses relax in a few minutes. Increasing the temperature further, the viscosity decreases and when it reaches $10^{7.6}$ Poise, the **softening point** is reached. In this regime a 1 mm diameter glass fibre deforms under its own weight at a rate of 1 mm/min when suspended vertically. Finally, at a viscosity of 10^4 Poise, the **working point** is reached, here the glass is suitable for working or forming. A typical annealing process for FLM fabricated devices is reported in Figure 3.2. First there is a rapid heating above the annealing point, then the temperature is kept constant for a few minutes in order to release all internal stresses, then a gradual drop in temperature (a few °C/h) begins until a point below the strain point is reached. This ramp at low rate is important in order to not add further stress during the cooling procedure. Finally, cooling of the sample is performed at higher rate till room temperature is reached. It is worth noting that as each glass has different chemical compositions, it is necessary to optimize the annealing procedure for each glass.

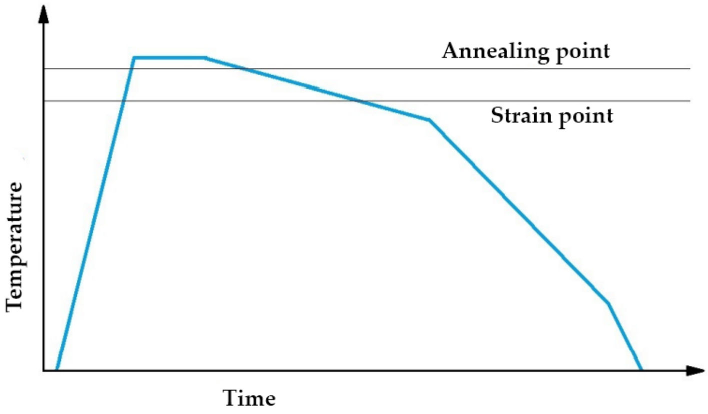

Figure 3.2: Example of an annealing process.

In addition, annealing was shown to have beneficial effects on the waveguides, increasing their quality. This was first demonstrated by Arriola et al. in 2013 [117], where they showed that annealed guides had lower bending losses and a more Gaussian-like refractive index profile, which is known to have good light propagation properties as it is similar to the step-index profile [117]. In the paper, a two-step procedure was illustrated. First, guides with higher energy and lower writing speed than normal single-mode guides were manufactured, thus producing multi-mode guides, then the second step was annealing. From image 3.3a it can be seen that before annealing, starting from the outside, there is a lighter ring, a darker corona and the lighter guiding region, which correspond respectively to a slight increase, a decrease and again a more pronounced increase of the refractive index (as shown on the left side of the Figure 3.3c). After annealing (Figure 3.3b) there is the disappearance of the outermost ring and a small variation of the refractive index in the guiding region (right side of the Figure 3.3c), making the profile more similar to a Gaussian one. This profile is shown to be effective for producing single-mode guides with a significant decrease in bending losses. Furthermore, the annealing process decreases the inevitable birefringence of the waveguides that are formed using FLM [117].

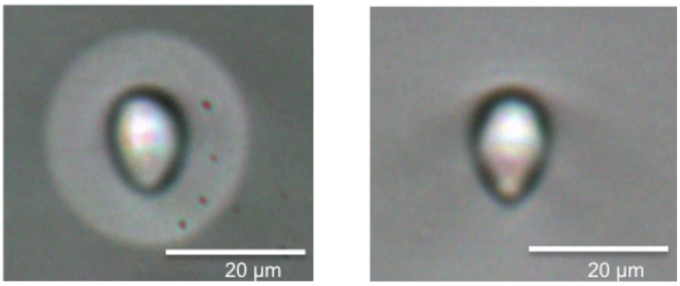

(a) Section before annealing. (b) Section after annealing.

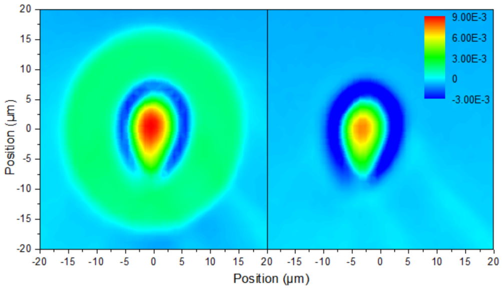

(c) Refractive index profile.

Figure 3.3: The figure shows the cross-sections before (a) and after (b) annealing and the corresponding refractive index profile (c), where the complete disappearance of the outer ring and the appearance of a Gaussian-like profile can be seen. Images taken from [117].

3.1.3. Cut and Polish

After the annealing process, the sample is almost ready for characterization. The last step to make the sample characterisable is the cut and polish process. Usually the ends of the sample, input and output, are cut by 1 or 2 mm in order to cut edge effects or tapering in the waveguides. Tapering refers to a waveguide that progressively narrows [118], as shown in Figure 3.4a. This phenomenon occurs when the laser enters the glass and has yet to form a plasma, leading to a slight modification of the material, jeopardising the propagation of light. After cutting, the input and output facets show roughness in the surface, leading to light scattering and not allowing characterization. They therefore require polishing. This can be done manually or by using an automatic machine (KrellTech FLex Waveguide Polisher). The method consist of polishing the facet in circular motions, starting with higher roughness abrasive discs ($30\,\mu m$) up to very fine roughness ($3\,\mu m$), until it reaches a facet without scratches and roughness.

Alternatively, a faster but often more inaccurate method is to use a cleaving machine. This method consists in a controlled breakage of the glass, initially by introducing a crack, with materials such as diamonds or sapphires, and then applying a tensile force so as to section it perfectly. In this way, an already polished facet is obtained.

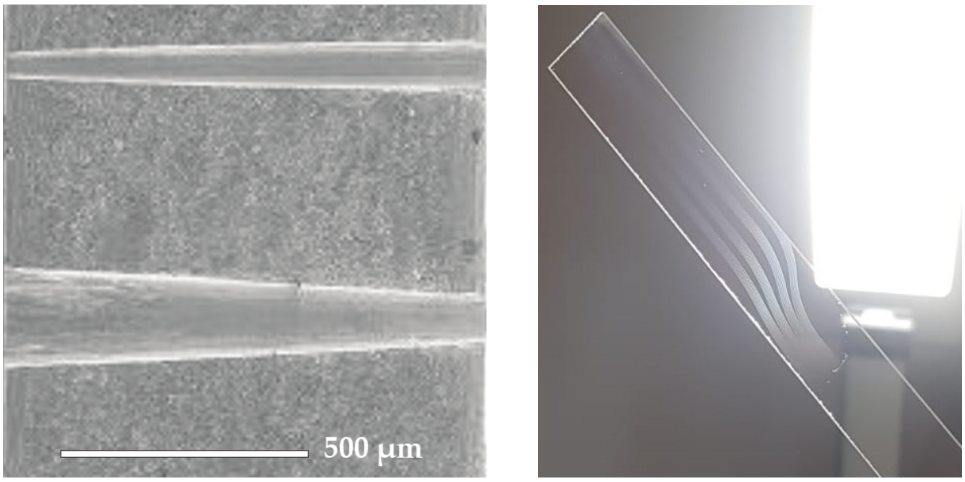

(a) (b)

Figure 3.4: a) Tapering effects on a waveguide. Image taken from [119]. b) Final sample obtained after all the fabrication processes explained in section 3.1. The sample contains bending waveguides. Four groups of waveguides with different radii of curvature can be appreciated inside the sample. Each group contains several waveguides.

3.2. Characterization Setup

After fabrication, several characterization steps are necessary to analyse the properties of the guides and to check the correct functioning of the device. They will be explained in detail in the following subsections.

3.2.1. Microscope Analysis

The first characterization to be carried out is inspection under an optical microscope. This is a quick method that allows the correct geometry to be verified and the condition of the waveguides to be assessed qualitatively. In fact, from a top surface observation it is possible to see if there have been any interruptions during manufacture, for example due to dust grains on the surface or, if the sample is immersed in water, due to bubbles on the surface. To reduce the possibility of small interruptions we usually write the waveguides close to the bottom surface of the substrate. Indeed, this method allows us to avoid severe distortions induced on the beam profile by dust particles present on the top surface of the substrate, since the laser beam is not yet focused when it crosses such defects. After cutting and polishing, the sample facets are brought to optical quality. This is done for allowing the following optical characterization of the devices without experiencing additional coupling losses induced by scattering given by roughness and defects on the input/output facets. In addition, the polished facets can be observed with an optical microscope. This optical evaluation of waveguides' cross-section allows us to retrieve qualitative information on the refractive index change induced during fabrication, as well as on the quality of the polishing procedure.

For this purpose, a Nikon ME600 microscope equipped with an optional Differential Interference Contrast (DIC) module was used, which allows enhanced vision of small index contrasts by exploiting interference phenomena. In addition, a high-resolution CCD camera (PixeLINK B871) is mounted above the microscope for computer picture acquisition.

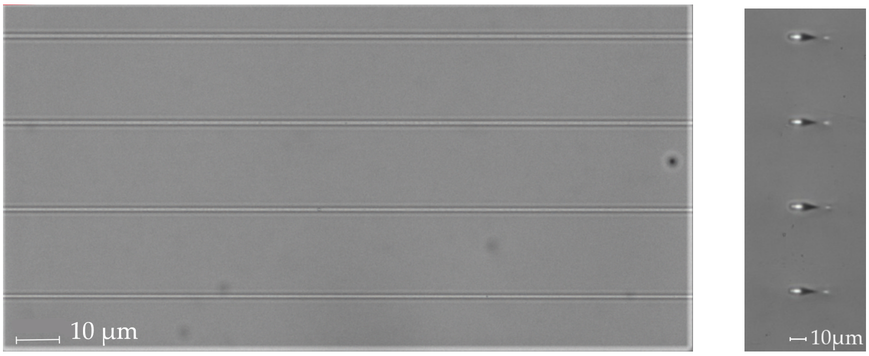

(a) (b)

Figure 3.5: Microscope inspection of waveguides. a) Top view of four waveguides. b) Cross section of four waveguides.

3.2.2. Device Coupling

To measure the properties of the guides, it is necessary to couple the device to coherent light. In this thesis several laser diodes were used for the characterization of PICs. In particular, Thorlabs laser diodes at 1310 nm (L1310P5DFB) and 1550 nm (L1550P5DFB) and a Santec tunable laser from 1480 nm to 1600 nm (ECL-200). Among different methods for coupling light into an integrated optical circuit, two have been exploited in this thesis. The first is called *end-fire* and the second is called *fiber-butt*. With the first approach, the light from the diode is collimated by a microscope objective or an aspherical lens and directly steered to the input facet of the device. In order to maximise the coupling efficiency, the numerical aperture of the imaging system and the focal spot should match the numerical aperture of the waveguides (~ 0.1 in FLM waveguides) and the mode size, respectively. This approach is mainly used if one wants to make polarization measurements, as the objective does not change the polarization of the laser light. If, for example, we want to precisely measure the losses of the waveguides, the *fiber-butt* configuration is preferred. In this configuration the light collimated by the objective is coupled into a single mode fiber (SMF), which after being cut and peeled is coupled to the device by simply bringing it closer to the input facet. For both configurations, the light leaving the device is collected by another objective, typically with a large numerical aperture so as to properly collect light. The collimated light will finally be directed to a detector, which can be a powermeter (Ophir NovaII) for example for loss measurements or an infrared camera (Xenics Bobcat-640) for mode measurements.

Very stable and precise micropositioners are required for correct sample-to-fibre (or sample-to-objective) alignment. The sample is glued onto a four-axis micropositioner (Thorlabs MBT40) which allows translation in the plane perpendicular to the optical axis and adjustment of two independent tilts, pitch and yaw. The fiber or objective is fixed onto a manual three-axis micropositioner (NanoMAX Thorlabs) with a resolution of 50 nm on each axis.

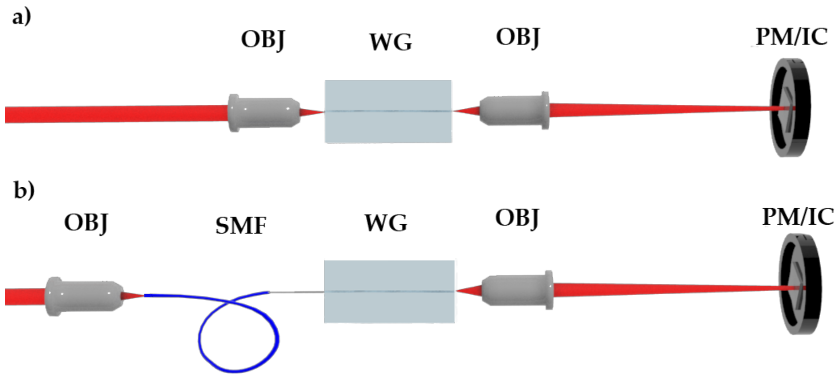

Figure 3.6: Setup for waveguides characterization. Two different coupling configuration: *end-fire* a) and *fiber-butt* b). In the *end-fire* configuration the laser beam from the diode is focused by an objective (OBJ) directly into the waveguide (WG) input facet. While in the *fiber-butt* configuration the beam is focused by the objective into the single mode fibre (SMF) and then into the waveguide (WG), simply bringing them close. For both, the light is then collected in a powermeter (PM) or an imaging camera (IC).

3.2.3. Mode Profile

The analysis of the spatial intensity profile I_{wg}(x,y) is a fundamental step for the characterization of the waveguides as it allows us to study the confining properties and to estimate the coupling losses. It also allows us to distinguish single-mode waveguides from multi-mode waveguides, as in most applications the use of single-mode is required in order to better engineer the evanescent field and thus couple waveguides. To measure the mode profile of the waveguides, a *fiber-butt* configuration was used and the near-field profile exiting the waveguides was measured using a high-sensitivity infrared camera (Xenics Bobcat-640). In order to exploit the full dynamics of the camera and not saturate it, the beam intensity has been attenuated either by decreasing the driving current of the laser diode or by using optical attenuators. To ensure that we are dealing with a single mode waveguide we observe whether only the fundamental mode or also higher order modes can be supported by the guiding structure. This operation is performed by observing the mode profiles in a CCD camera while varying the position of the impinging laser beam in the plane orthogonal to the optical axis.

Hereafter, we report on the full procedure for a correct measurement of the mode profile. After the guided mode is acquired, since the magnification factor of the collecting system is not known, we proceed acquiring an image of the guided mode of the single mode fiber used for coupling. Indeed, since the size of the fiber is well known (either by manufacturer specifications or by previous calibration), we use this method to calibrate the magnification of the system in terms of μm/pixel. To do so, we proceed by removing the device and making sure that the objective-camera distance remains unchanged, so as to maintain the same magnification. Finally, the two images are processed by a Matlab program that, after a numerical analysis, gives us the intensity profile of the modes I_{wg}(x,y) and allows us to calculate the overlap integral between the fiber mode and the guided mode, which is then used to estimate the coupling losses as reported in paragraph 3.2.4. Since theory guarantees that the fundamental mode of the waveguide does not present signs of inversion, we can neglect the absolute value in (3.1) and derive the electric field E_{wg}(x,y) from the formula (3.1).

$$|E(x,y)| = C\sqrt{I(x,y)} \tag{3.1}$$

Moreover the constant C is not relevant because what we are interested is the normalized profile.

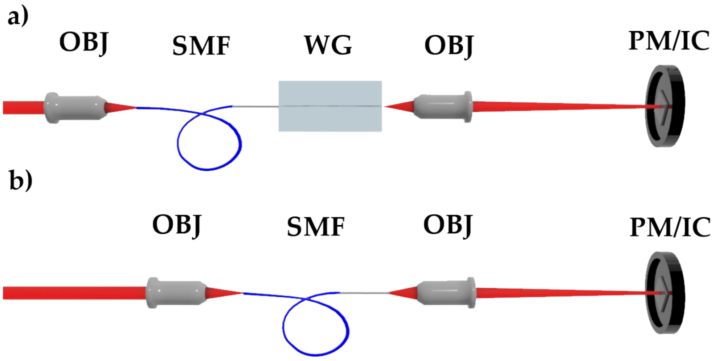

Figure 3.7: Scheme of process to measure the mode profile or to measure the losses of a device, coupled with the *fiber-butt* configuration. First a) the mode profile (losses) of the waveguides is measured by the imaging camera IC (powermeter PM), then the device is removed b) and the mode profile (losses) of the single mode fiber (SMF) is acquired.

3.2.4. Losses

In general, in optical devices, the losses are one of the bottlenecks that still need to be improved. Especially in quantum photonics, where the manipulation of single photons is required, having low losses is a key feature. Typically, the total losses of a PIC are quantified in Insertion Losses (IL). IL are defined as the total losses due to the insertion of the device and are measured in dB:

$$IL_{\text{dB}} = -10\ log_{10}\left(\frac{P_{\text{out}}}{P_{\text{in}}}\right), \tag{3.2}$$

where P_{in} and P_{out} are the optical powers at the device input and output respectively. In the case of more than one output ports, P_{out} is calculated by sum the power values measured at each port of the device. To measure IL the setup is mounted in fiber-butt configuration. After the power P_{out} is measured, the device is removed and the light of the fiber is collected by the objective and steered into the powermeter head, as reported in Fig 3.7, to measure P_{in}. It is worth noting that the measurement will also include the loss due to the objective, but since it represents a common term in both measurements it will not appear in formula (3.3). IL are the result of the sum of four different contributions: Fresnel Losses (FL), Propagation Losses (PL), Coupling Losses (CL) and Bending Losses (BL). All this term can be put together using the following formula.

$$IL_{\text{dB}} = CL_{\text{dB}} + 2FL_{\text{dB}} + PL_{\text{dB}} \cdot l + BL_{\text{dB}} \cdot l_{\text{c}} \tag{3.3}$$

In the following will be explained each term of Equation (3.3).

Fresnel Losses are caused by Fresnel reflection which occurs when light passes through two different materials and thus suffers a refractive index discontinuity, in our case the air-glass interface. It is defined by the following formula:

$$FL_{\mathrm{dB}} = -10\ log_{10}\left[1 - \left(\frac{n_2 - n_1}{n_2 + n_1}\right)^2\right], \tag{3.4}$$

where n_1 and n_2 are the refractive indices of materials 1 and 2 respectively. Note that the term inside the square brackets is transmittance, which is complementary to reflectance (in round brackets, including the exponential). Taking the glass and air values and substituting them into the Equation (3.4), we obtain a FL value of 0.177 dB. This value will be multiplied by two, considering that there are two interfaces to cross. Note, however, that a Fabry-Perot cavity is formed between the inlet facet and the fiber. In fact, they are placed very close to each other. This implies that, during the measurement, if we place at the point of maximum transmission, only the output FL contribution can be considered. Otherwise, to eliminate this value, a drop of index matching oil can be deposited between the fiber and the waveguide input facet.

Coupling Losses result from the mismatch between the electric field distribution of the waveguide mode and the electric field distribution of the light impinging the input facet. It is described by the formula (3.5).

$$CL_{\mathrm{dB}} = -10\ log_{10}\left(\frac{|\iint E_{\mathrm{wg}}E_{\mathrm{in}}\ dxdy|^2}{\iint |E_{\mathrm{wg}}|^2 dxdy \cdot \iint |E_{\mathrm{in}}|^2\ dxdy}\right), \tag{3.5}$$

where the term inside the parenthesis represents the overlap integral of the two electric field distributions. The two distributions are calculated numerically using the method seen in section 3.2.3.

Propagation Losses are the losses that light experiences when propagating along the guide. These losses are due to inhomogeneities in its core refractive index profile. In fact, the fabrication process can induce roughness in the waveguide profile, which can lead to light scattering and coupling to radiative modes. An additional reason could be the presence of absorption centres or defects. From theory we know that the propagation of light power can be described as follows:

$$P(l) = P(0)e^{-\alpha l}, \tag{3.6}$$

where l is the waveguide length, $P(0)$ the power at the beginning of the waveguide and α the attenuation coefficient. Propagation losses, on the other hand, are described by the formula (3.7)

$$PL_{\mathrm{dB/cm}} = -\frac{10}{l}\, log_{10}\left(\frac{P(l)}{P(0)}\right) \tag{3.7}$$

This time expressed in dB/cm as it is dependent on l. It is possible to relate the attenuation coefficient α to it using the formula $PL_{\mathrm{dB/cm}}= 10\ log_{10}(e)\alpha_{\mathrm{cm}^{-1}}\approx 4.3\ \alpha_{\mathrm{cm}^{-1}}$.

A practical way to derive PL is to invert the formula (3.3) and obtain the equation (3.8). After measuring IL and calculating CL and FL values, it is thus possible to retrieve PL. This method may introduce a high uncertainty because all the uncertainties of the other measurements are added up.

$$PL_{\mathrm{dB/cm}} = \frac{IL_{\mathrm{dB}} - 2FL_{\mathrm{dB}} - CL_{\mathrm{dB}}}{l}. \tag{3.8}$$

To assess propagation losses we also used another method called "cutback". In the cutback, the insertion losses of a sample of length L are measured. The chip is then cut in shorter length L_2 and L_3. For each length L_{i}, insertion losses are measured. After at least 3 points are acquired, a linear regression is performed. The intercept represents CL, while the slope represents PL. It gives more accurate values of PL, but it is a longer and sample-destructive process with respect to the one previously described.

Bending Losses occur when light experiences a curved trajectory. The guided field distribution is therefore distorted and a partial coupling with radiative modes occur. They increase exponentially by decreasing the radius R of curvature, as also shown in the formula (3.9).

$$BL_{\mathrm{dB/cm}} = C_1 e^{-C_2 R}, \tag{3.9}$$

where C_1 and C_2 are numerical constants that depends only from the waveguide mode profile and size [120]. Bending losses are higher for waveguides with lower refractive index contrast, due to their less confined guided mode. A practical way to measure bending losses and their exponential trend with R consist of fabricating waveguides with different radii R_{i} always maintaining the same bend path l_{c}, with also a straight waveguide (SWG), which will be taken as reference. The SWG (blue in figure) can be considered with a bend part l_{c} of infinite radius. The fabrication device is presented in Figure 3.8. Then the IL of the straight waveguides will be subtracted from the ILs of the different radius waveguides, in the approximation of h_{i} equal for all waveguides. Since the values of CL, FL and PL

are equal for both, only the bending term will remain, as explained by the formula (3.10).

$$(BL_{\mathrm{i}})_{\mathrm{dB/cm}} = \frac{(IL_{\mathrm{i}})_{\mathrm{dB}} - (IL_{\mathrm{SWG}})_{\mathrm{dB}}}{l_{\mathrm{c}}} \tag{3.10}$$

By fitting the BL data in dependence on R, it is possible to derive the exponential trend and thus retrieve the constants C_1 and C_2 of the formula (3.9).

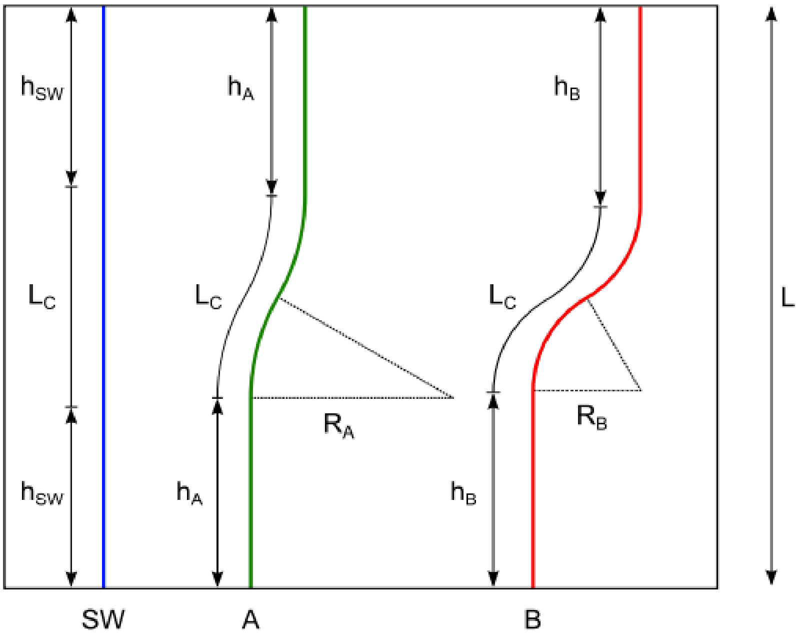

Figure 3.8: Image illustrating the device fabricated for calculating bending losses. Image taken from [121].

3.2.5. Extinction Ratio Measurement

Imagine having a laser beam incident on a beam splitter and wanting to direct the whole beam only in one branch, i.e. to obtain a transmission of 1 in one branch (P_1) and a transmission of 0 in the other (P_0). The extinction ratio (ER) is the ratio between the power of branch P_1 and the power of branch P_0 and is usually expressed in dB [122]:

$$ER = 10\ log_{10}\frac{P_1}{P_0} \tag{3.11}$$

In other words, the ER describes the goodness of separation of powers between the two branches, the wider the separation, the greater the ER. By adopting an integrated optics approach the beam splitter becomes a directional coupler 0:100 or 100:0 (discussed in detail in the chapter 4), i.e. total transmission in one branch and zero transmission in the other. In the following, the procedure for measuring ER will be explained.

After the device has been properly coupled, it is necessary to accurately measure the powers of the two branches. To do this, the light from the two branches is collected by a high sensitivity camera. The power is then measured according to the exposure time of the camera, taking as reference the value close to saturation. By varying the exposure time of the camera for the two powers, while maintaining the same level of saturation for both, it is possible to calculate ER using the Equation 3.11 and replacing the powers $\mathrm{P_1}$ and $\mathrm{P_0}$ by the exposure times $\mathrm{T_1}$ and $\mathrm{T_0}$. However, being a high sensitivity camera, the $\mathrm{P_1}$ branch would easily saturate the camera for any available exposure time of the camera, not allowing a correct measurement. For this reason an additional attenuation factor must be added. In our case we have added several optical density in series (OD) in the optical path of the P1 branch in order to achieve the desired attenuation. Finally we adapted the Equation 3.11 taking into account this modification, and thus calculating the ER through the following equation:

$$ER = OD + 10\ log_{10}\frac{T_1}{T_0}, \tag{3.12}$$

where OD is the value in dB of the attenuation due to the sum of the optical density in series. An illustrative picture of the ER measurement process is shown in Figure 3.9.

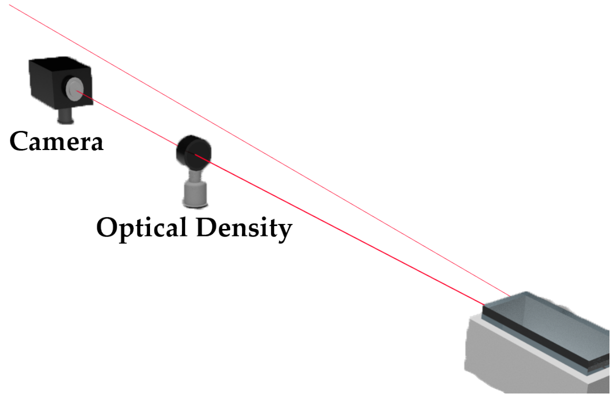

Figure 3.9: Setup to measure the extinction ratio. The most powerful beam is attenuated by placing optical density in the optical path. The measurement is described in detail in the text.

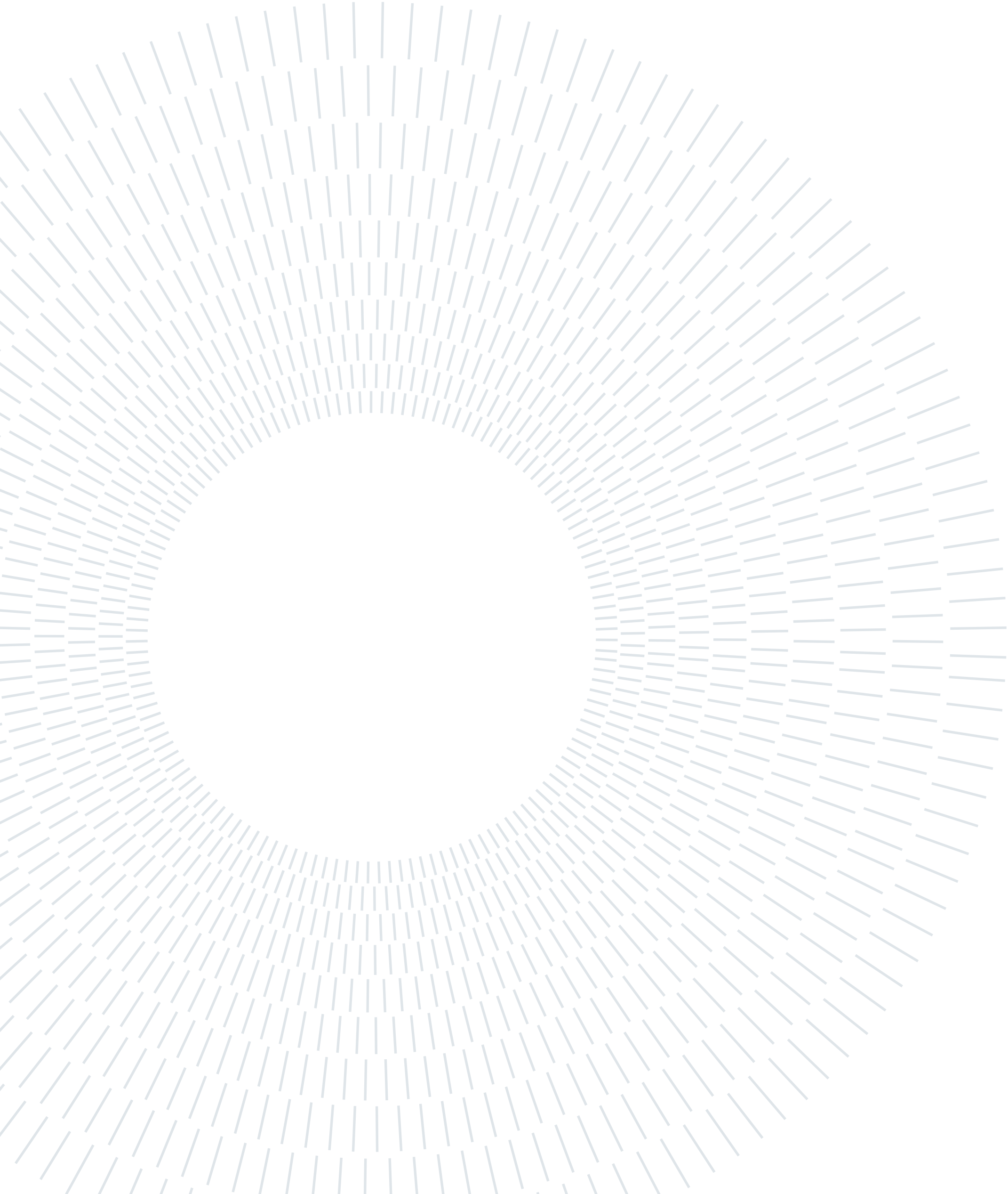

4 | An Optical Filter for Heralded Photon Source on Chip

This chapter deals with the general description of the thesis project. In section 6.1 the motivations behind the project are presented. Following in section 4.2 the design of the chip will be discussed and the various components that compose it will be described. In section 4.3 a more specific description of the WDM is provided, including description, working principle and the current state of the art in FLM.

4.1. Motivation

As stated in the previous chapters, quantum photonics in bulk suffer on scalability and stability issues, which can be circumvented through an integrated approach. Miniaturization, scalability and stability are the key requirements to build complex circuits and thus achieve computational complexities far beyond classical computation. In particular, it would be desirable to build a complete quantum photonic processor on a single chip. It follows that the ideal quantum photonic processor should encompass sources, devices capable of performing arbitrary unitary operations, and detectors on the same unit. Actually, progress and developments in recent years have convinced the quantum photonic community that it would be difficult to meet all the strictly requirements of such a processor on a monolithic platform and that a hybrid approach would represent the fastest way to achieve quantum advantage on chip. Indeed, hybrid photonic based on different materials and platforms promises to leverage the strengths of each photonic system while avoiding their weaknesses [123]. In this scenario, femtosecond laser micromachining represents a promising technique due to its capability both to process different materials and to produce optical interconnects with high coupling efficiency. In the general framework of the project, the aim is to create a standalone heralded integrated source. This device should be capable of generating pairs of pure single photons simultaneously, filtering the pump photons from the daughter photons and splitting the heralding photon from the heralded ones, all on a chip. Finally, this source should prepare an input state with a consistent number of indistinguishable photons for the implementation of a scattershot boson sampling experiment. This project is in collaboration with the Quantum Optics group of La Sapienza University in Rome.

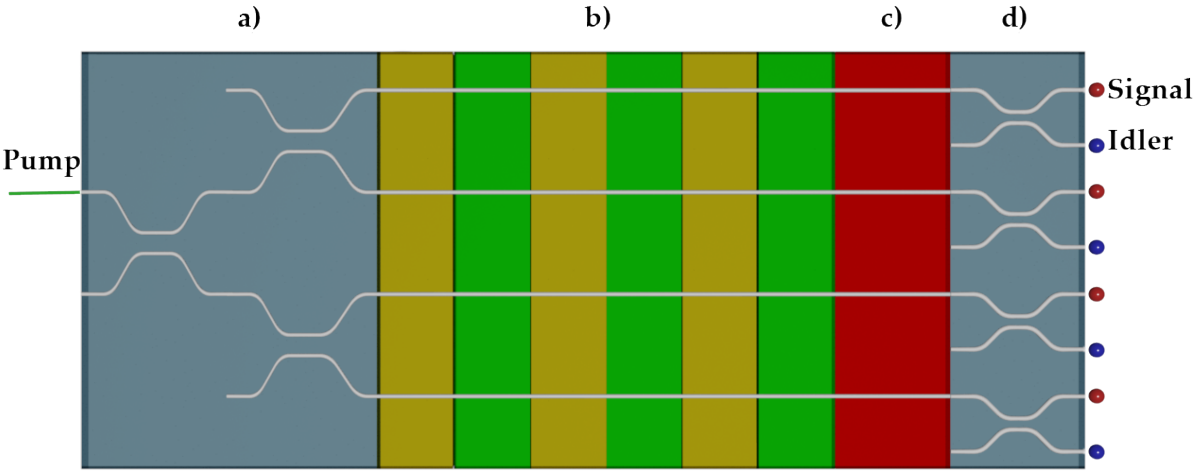

Figure 4.1: Schematic diagram of the heralded photon source on chip. The pump beam enters the chip and is split into several branches via cascaded DCs a). After that the beams enter the PPKTP crystal b) where the generation of single photon pairs by means of SPDC process takes place. Next, the photons are filtered by the pump photons c) and finally the signal photons are split from the idler photons d).

4.2. Chip Design

In the following, each individual part of the integrated heralded source will be explained. As a first step, the pump beam is divided in several branches, equal to the number of waveguides in the following nonlinear crystal. It is worth noting that beams in different arms should be phase locked, thus the integrated approach for splitting the pump beam. One method of splitting the initial beam is by bifurcation. To fabricate such a device in FLM, a waveguide is inscribed in the glass and at some point split into several waveguides. The guides must support the single mode, but in the bifurcation part the waveguide widens into an area called "tapered", which supports multiple modes. The bifurcation must occur smoothly, otherwise coupling to radiative modes will occur and consequently introduce large losses. Another method that can be employed is that depicted in Figure 4.1a, which consists of fabricating a cascade of 50:50 directional couplers. The directional couplers (DC), which will be discussed in more detail in section 4.3, redistribute the light due to the coupling of the evanescent field. A special case of DC is the 50:50 DC, or 3 dB DC, which divides the power of the incoming beam equally in the two output waveguides. Cascading N rows of DCs will result in 2^N branches. By using an appropriate radius of curvature for the bend sections, lower losses can be achieved compared to the bifurcation approach. The second step is the effective generation of pairs of single photons, part b) of the Figure 4.1. For this project, the generation will be done by means of the nonlinear SPDC effect. Specifically, the waveguides will be inscribed parallel to each other within a crystal of periodically poled potassium titanyl phosphate (PPKTP). Previous simulations have shown that PPKTP crystals can provide single photons with a high purity. The crystal will be then pigtailed to the glass to make a hybrid device. The third part of the source concerns the filtering of the pump photons, part c) of the picture. In fact, as mentioned in section 1.3, the SPDC from a more energetic pump photon generates a pair of less energetic photons, namely signal and idler. Since this process has a low conversion efficiency, it will result that at the output of the source the pump photons will be orders of magnitude higher than the number of signal and idler photons generated. Therefore, without appropriate filtering, they will saturate the detectors. So the implementation of an integrated long-pass or band-pass filter is needed. An efficient filtering of the pump requires 100 dB of extinction [86], a difficult task for current filters in the literature. Actually, for this experiment it is still to be defined how the integrated filter will be implemented. However, some examples can be found in the literature, as mentioned in section 1.3.1. Finally, the last part involves the division of signal from idler photons. Accordingly to the generation process, there can be several methods to split signal from idler photons. For example, in case of a Type II SPDC process, signal and idler photons can be discriminated according to their polarization. Indeed, the generated photons would have orthogonal polarizations and an integrated polarization beam splitter would allow one to separate them efficiently. Otherwise, in case of a nondegenerate SPDC process, the daughter photons can be divided according to their wavelength. In this project a pump with a wavelength of 780 nm will be used to generate two photons at two different wavelengths, in a range from 1100 nm to 1600 nm. An effective method to separate photons at different wavelengths is the Wavelength Division Multiplexer (WDM). Since in this thesis we focused on the fabrication of this building block and we worked on the optimization of WDMs by femtosecond laser writing, a complete description of WDM working principles and an up-to-date state of the art for this technology will be provided in the following section.

For the sake of completeness Figure 4.2 shows the complete chip for the scattershot boson sampling experiment, in which besides the source there is the U matrix and the detection part, elements outside the scope of this thesis.

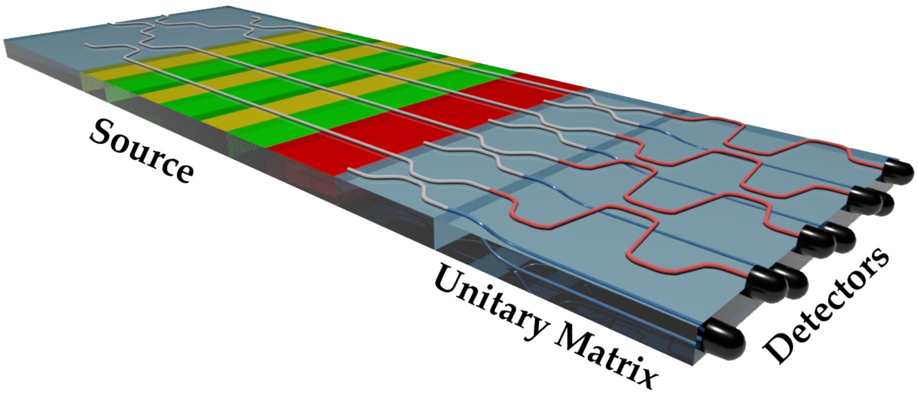

Figure 4.2: Final device to perform scattershot boson sampling. The device, operating at four photons, is for illustration purposes only. The chip encompasses, starting from the left, the source (as described in Figure 4.1), a unitary matrix and detectors. Exploiting the 3D capabilities of femtosecond laser writing, the heralding photons will propagate in a layer beneath the unitary matrix and will be detected by detectors in the bottom row, while the detectors in the top row sample the output state of the matrix.

4.3. WDM

A wavelength division multiplexer (WDM) is a device capable of dividing an optical signal composed of several wavelengths into signals composed of the individual wavelengths, Figure 4.3a. In integrated optics, there are various ways to implement such a device, e.g. WDM based on Sagnac interferometers [124] or WDM based on Bragg gratings [125] can be found in the literature. Another simple way, which is the one used in this thesis, to implement a WDM is through directional couplers.

As mentioned in the previous sections, a directional coupler (DC) is a component that redistributes optical power through evanescent field coupling. An illustration of a directional coupler is shown in Figure 4.3b. It consists of two non-interacting, parallel waveguides that approach each other via a curved section of radius of curvature r, remain close for an interaction length L at an interaction distance d and then return to the initial distance D. By changing the parameters d and L, it is possible to engineer the DC to achieve the desired power distribution at the two outputs. A DC is therefore a four-port component where if we consider the input from one branch, the output from the same branch is called reflection (R) or bar, while the output from the adjacent branch is called transmission

(T) or cross. So a WDM based on this approach is a directional coupler designed to split two different wavelengths (λ_1, λ_2), i.e. takes two wavelengths from the same input and divides them into the two different outputs, as depicted in Figure 4.3b.

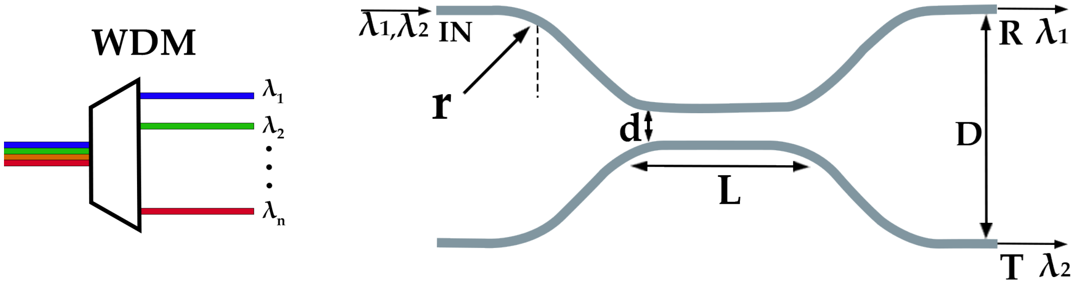

(a) (b)

Figure 4.3: a) Diagram of the operating principle of a WDM. b) Scheme of a WDM based on directional coupler.

4.3.1. Working Principle

The fundamental element of a DC, as of integrated optics in general, is the optical waveguide. Before going into a mathematical description of the functioning of a DC, it is necessary to understand the propagation of light within an optical waveguide. This element consists of a wire with a refractive index n_1 (core), embedded in a substrate with a refractive index n_2 (cladding), where $n_1 > n_2$. In this way the light is deflected inside through internal reflections. Analytically determining an expression for the propagation of an electromagnetic field within a waveguide is not possible, however, approximate solutions can be used, for example using Marcatili's method [126] or perturbative analysis [127]. Otherwise, thanks to available computing power, approximate methods can be replaced by numerical simulations [128]. In the approximation of weakly guiding dielectric waveguides, i.e. if $(n_1 - n_2)/n_1 << 1$, as in our case, it is possible to derive a scalar expression for the propagation of the electric field inside the waveguide. This equation is described as follows:

$$\mathcal{E}(x, y, z, t) = E(x, y) \cdot e^{i(\beta z - \omega t)}, \tag{4.1}$$

where ω is the angular optical frequency, $E(x, y)$ is the transverse spatial field profile (the mode shape) and β is the propagation constant. The equation above describes the propagation of the electric field within an independent waveguide, but the situation changes if two independent waveguides are placed close together, as in the case of a DC.

If two waveguides are placed close together at such a distance that the guided modes overlap, a power transfer between the waveguides can occur. Power is transferred due to the coupling of the evanescent field of the propagating mode, which is why this effect is called "evanescent waveguide coupling". This phenomenon can be studied in the weakly coupled approximation, which assumes that the guided modes of independent guides are not affected by the proximity of the other. On this approximation relies the coupled mode theory [129], thanks to which it is possible to derive the expression for the propagation of light within a waveguide when coupled to another waveguide. It can be seen that the effect of coupling to another waveguide leads to a modulation of the electric field amplitude obtained from the Equation 4.2, so in this case the equation can be rewritten as follows:

$$\mathcal{E}(x,y,z,t)_j = a_j(z) \cdot E_j(x,y) \cdot e^{i(\beta_j z - \omega t)}, \tag{4.2}$$

where the subscript j refers to waveguide 1 or 2 and $a_j(z)$ is the function that modulates the amplitude. In particular it can be proved that this two function can be derived by the following equations [129]:

$$\begin{cases} \dfrac{da_1(z)}{dz} = -i\kappa e^{i\Delta\beta z} \cdot a_2(z) & \text{(4.3a)} \\ \dfrac{da_2(z)}{dz} = -i\kappa e^{-i\Delta\beta z} \cdot a_1(z), & \text{(4.3b)} \end{cases}$$

where $\Delta\beta = \beta_1 - \beta_2$ is the detuning between the two waveguides, i.e. the difference in their propagating constant β_i. The latter is defined as $\beta_\mathrm{i} = \frac{2\pi}{\lambda}\Delta n_\mathrm{i}$, where $\Delta n_\mathrm{i} = n_\mathrm{i} - n_0$ is the refractive index contrast between the waveguide core and the substrate. Therefore $\beta_\mathrm{i} = \frac{2\pi}{\lambda}\Delta n_{1,2}$ where $\Delta n_{1,2} = \Delta n_1 - \Delta n_2$. While κ is the coupling coefficient and it is proportional to the modes overlap of the individual waveguides:

$$\kappa \propto \iint E_1(x,y)E_2(x,y)dxdy. \tag{4.4}$$

It is usual to describe mode coupling in terms of power, and so it is possible to convert the amplitude functions a_j into power functions simply by calculating their square modulus. So referring back to the directional coupler by injecting light from one input we can write the normalized mode power propagation of reflection and transmission as follows:

$$\begin{cases} R(z) = \cos^2(\sigma z) + \dfrac{\delta^2}{\delta^2 + \kappa^2}\sin^2(\sigma z) & \text{(4.5a)} \\ T(z) = \dfrac{\kappa^2}{\delta^2 + \kappa^2}\sin^2(\sigma z), & \text{(4.5b)} \end{cases}$$

where $\sigma = \sqrt{\delta^2 + \kappa^2}$, $\delta = \Delta\beta/2$. It is possible to notice that transmission is complementary to reflection, i.e. $T = 1 - R$ at any point. When the two waveguides are identical, namely $\Delta n_1 = \Delta n_2$, $\Delta\beta = 0$ and the directional couplers are called *synchronous*. In the case of *synchronous* DC we have that $\sigma = \kappa$ and therefore the power transfers completely from one waveguide to the other periodically, with a period $\Lambda = \pi/\kappa$. If, on the other hand, the waveguides are different, $\Delta n_1 \neq \Delta n_2$, $\Delta\beta \neq 0$ and therefore the directional couplers are called *asynchronous*. It follows that there will never be a complete power transfer, i.e. $R \neq 0$ always. The power will therefore be transferred up to a minimum of R periodically, with period $\Lambda = \pi/\sqrt{\kappa^2 + \delta^2}$. This trend can be noted in Figure 4.4.

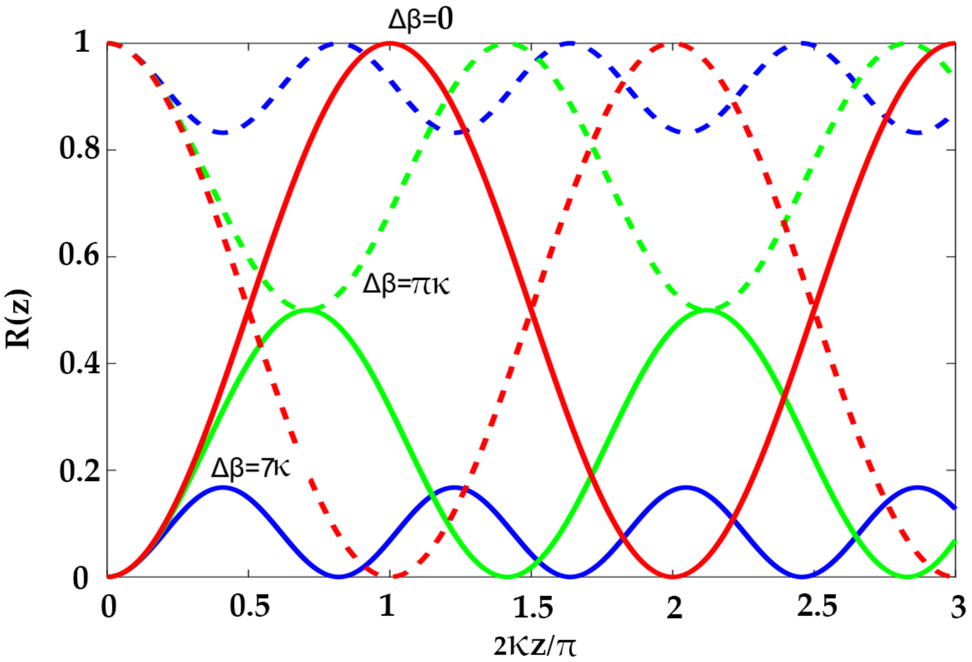

Figure 4.4: Optical power as a function of the coupling length (in units of $\pi/2\kappa$). It is possible to notice that for $\Delta\beta = 0$ there is a total transfer of power, while in the other case the power transfer is not complete. Image adapted from [121].

Note that to divide two wavelengths, a total power transfer is required. Therefore for the implementation of a WDM it is necessary to employ *synchronous* directional coupler. For this reason, only *synchronous* directional couplers will be referred to in the following.

So in the case of identical waveguides, the Equation 4.5 simplify as below:

$$\begin{cases} R(z) = \cos^2(\kappa z) & \text{(4.6a)} \\ T(z) = \sin^2(\kappa z). & \text{(4.6b)} \end{cases}$$

However, as the waveguides approach the curved section, partial coupling of the evanescent field occurs. It follows that the presence of the curved sections leads to the effective interaction length being greater than L. To take this into account, the residual coupling in the section L_{t} is calculated, as given by the equation below:

$$L_{\mathrm{t}} = \int_0^{\infty} e^{-\gamma(d(z)-d_0)} dz, \tag{4.7}$$

where γ is the attenuation factor of the evanescent field and $d(z)$ is the distance between waveguides in curved sections. The reason for the exponential in the formula is that κ decreases exponentially with the interaction distance, accordingly with the exponential trend of the evanescent field in the region between the two waveguides. Since we have two curved regions, the effective interaction length is $L + 2L_t$. Assuming a constant radius of curvature r, the distance between the waveguides in the curved path will be $d(z) \simeq d_0 + z^2/r$, thus the interaction length will be equal to:

$$L_{\mathrm{t}} = \frac{1}{2}\sqrt{\frac{\pi r}{\gamma}}. \tag{4.8}$$

Another way of considering the partial coupling occurring in curved sections is by adding a phase term ϕ. In fact, we can rewrite the values of R and T through the following formula:

$$\begin{cases} R(z) = \cos^2(\kappa z + \phi_0) & \text{(4.9a)} \\ T(z) = \sin^2(\kappa z + \phi_0). & \text{(4.9b)} \end{cases}$$

The underlying principle of WDM operation is that both κ and ϕ_0 are wavelength-dependent, as will be described in more detail in the section 5.2.

So in summary, for the implementation of a WDM it is necessary to achieve that the beam at wavelength λ_1 is totally transmitted in the reflection port, while the beam at λ_2 is totally transmitted in the transmission port. Therefore, the conditions to be imposed are the following:

$$\begin{cases} R_{\lambda 1}(z) = \cos^2(\kappa_{\lambda 1} z + \phi_{0\lambda 1}) = 1 & \text{(4.10a)} \\ T_{\lambda 2}(z) = \sin^2(\kappa_{\lambda 2} z + \phi_{0\lambda 2}) = 1 & \text{(4.10b)} \end{cases}$$

and therefore find a coupling length z that satisfies the equations.

In order to recognize a high-quality WDM we can refer to some figures of merit. In particular, a WDM must, first of all, have a good extinction ratio, so as to precisely divide the two wavelengths and avoid photons ending up in the wrong branch, compromising the input state. Another feature it must have is low propagation losses, a fundamental aspect of any integrated optical circuit, but in particular for this experiment, as better explained in the section 6.1. Furthermore, it should also have the ability to interface with other devices while maintaining low coupling losses, reason for which the FLM technique was used. In the next section some examples of state-of-the-art with their respective values are presented.

4.3.2. State of the art in FLM

Different technologies can be used to implement a WDM. An effective method is to employ Mach-Zehnder interferometers. Munk *et al.* develop a WDM fabricated by SOI technology and consist of an eight-channel WDM cascading Mach-Zehnder interferometers [130]. This device showed high ER values between the channels, the worst case scenario amounted to 22 dB. Propagation losses were 1.8 dB/cm, while when interfaced to a single-mode fibre it showed coupling losses of 10 dB at each end. Otherwise, in the source mentioned in section 1.3.1, Krapick *et al.* [88], developed a WDM through a directional coupler fabricated by photolithography using deep UV contact printing. The WDM divided the wavelengths of 1575 nm and 803 nm with an ER of 15 dB and 20.6 dB respectively. A good feature of this device was the low propagation losses which were of 0.07 dB/cm in average. Another method to select wavelengths is through Bragg grating (BG), i.e. multiple layers of two different refractive indices alternating. By engineering the grating period, the desired wavelength can be selected. However, alternating refractive indices can lead to increased losses, which is fatal for our experiment. A hybrid approach between coupler and BG has been demonstrated by Song *et al.* [131], fabricating a three-channel WDM based on directional coupler assisted by a BG. The research team fabricated a directional coupler by UV irradiations with inside BGs fabricated with the phase mask method. The device divides the two wavelengths 1310 and 1550 nm through the directional coupler and the beam at 1490 nm is reflected by the BG into the waveguide adjacent to the input and showed transmission losses of 0.07 dB, 0.19 dB and 2 dB, respectively. The average ER of the device was 18 dB. Regarding WDM exclusively fabricated in FLM, Meany *et al.* developed a heralded integrated source combining elements of different materials, namely a hybrid integrated source [132]. In this source there was a WDM written in FLM that divided the wavelengths of 1550 nm and 1312 nm. This source component had losses of 3 dB and was able to split signals from idlers with an average extinction ratio of 10 dB. Another example can be found in the integrated source developed by Vergyris *et al.* [67]. In this source the written WDM was able to filter the signal photons with 6 dB extinction ratio. The device was written in substrate Schott AF45 showing propagation losses at 0.1 dB/cm.

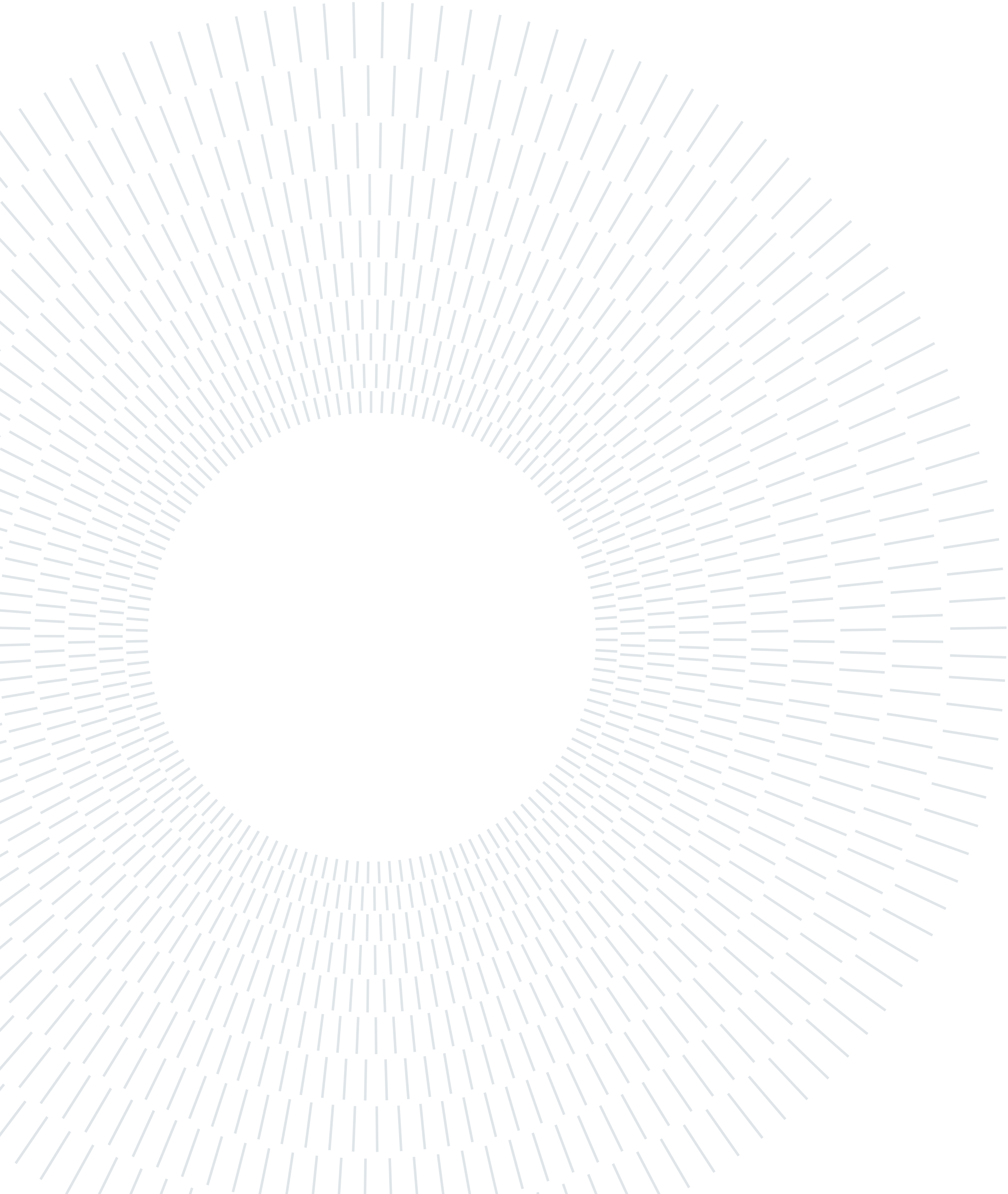

5 | WDM Fabrication and Optimization in EAGLE XG

This chapter deals with the fabrication and characterization of a WDM in EAGLE XG. In the first part, the whole procedure for the fabrication of a WDM is explained, from the analysis of the directional couplers to how to retrieve the coupling coefficient as a function of wavelength for designing the WDM till the actual fabrication of the device. In the second part, the fabrication and characterization of a WDM a for closer wavelengths is discussed, verifying its feasibility through a study of the wavelength dependence of the coupling coefficient for the range involved.

5.1. Direct Writing and optical characterization of WDM devices

The following WDMs were fabricated by exploiting femtosecond laser writing technique on a substrate of Corning EAGLE XG borosilicate glass. It was seen in section 2.2 that the FLM technique requires the optimization of several parameters in order to obtain a specific waveguide for our purposes. The optimization procedure requires time and the fabrication of several samples, for this reason and thanks to previous work, it was possible to start fabricating directional couplers with parameters optimized for both 1310 and 1550 nm waveguides. The fabrication parameters are shown in the table 5.1. The couplers have been fabricated using the transversal configuration, so as to exploit all the advantages explained in the section 2.2.3. With the parameters presented in the Table 5.1, it is possible to fabricate waveguides with propagation losses around 0.2 dB/cm and a single Gaussian mode of almost circular profile of $6.5\,\mu m$ and $8\,\mu m$ $1/e^2$ diameter for 1310 nm and 1550 nm respectively.

Fabrication Parameters	
Substrate	EAGLE XG
Laser System	Yb:KYW cavity dumped
Wavelength	1030 nm
Repetition Rate	1 MHz
Writing Power	475 mW
Translational Speed	10 mm/s
Number of Scans	5
Writing Depth	50 μm from bottom
Objective	20X WI, 0.5 NA

Table 5.1: Table containing the fabrication parameters.

The first step to develop the WDM is to define the geometry of the planar directional couplers, as describe in Figure 4.3b. The distance between the non-interacting waveguides of the DC is set at $127\,\mu m$, because it matches the standard outputs of the fiber arrays. The waveguides have been inscribed at a depth of $50\,\mu m$ starting from the bottom surface, as writing deeper has been shown to make the writing less sensitive to distortion in the shape of the laser profile, caused by dust or bubbles on the top surface. On the other hand, it has been shown by previous optimizations that writing closer to the bottom surface leads to higher propagation losses. The motivation has not been deeply investigated, but it can be related to the higher stress in the laser-substrate interaction. Another aspect to be taken into account for the writing depth is that some devices will be fitted with thermal phase shifters [22], so the more distance there is between the waveguide and the surface where the phase shifter will be deposited, the more heat you will need to dissipate to change the phase. So taking all these reasons into account, the writing depth was set at $50\,\mu m$ from the bottom surface. The interaction distance d, which is one of the parameter that most affects the coupling coefficient, is decided taking into account mainly two aspects. The smaller it is, the greater the coupling coefficient, thus transferring more power in less interaction length L, resulting in more compact devices. However, writing the second waveguide very close to the first one could cause modifications in the refractive index of the first written waveguide. This can cause both an increase in losses and a difference in the propagation constants of the two waveguides, thus leading to the fabrication only of asynchronous directional couplers, which are not suitable for working as WDMs since the power transfer cannot be complete (see Equation 4.5). Usually the optimal d is found by doing an interaction distance scan in a range of values comparable with the modal diameter. As regards the other parameters, the radius of curvature r only changes the initial phase ϕ_0 in Equation 4.10 and it is typically chosen by making a trade-off between compactness and losses. Indeed, high bending radii lead to longer devices and thus higher propagation losses, but if the bending radii are too small, bending losses occur. For these reasons, it was decided to use curvature radii of 30 mm. Finally, the interaction length L is chosen in order to obtain a total power distribution in the bar branch for one wavelength and a total power distribution in the cross branch for the other wavelength.

The first fabrication was done inscribing a set of couplers with L equal to 0 and varying d from 6 to $11\,\mu$m in steps of $0.5\,\mu$m. We perform the fabrication varying d and keeping L fixed in order to study the behaviour of κ in function of d. In fact, as explained in section 4.3.1, κ decreases exponentially with d, accordingly with the exponential trend of the evanescent field in the region between the two waveguides. Therefore, using a Matlab program, it is possible to derive the parameters a and b of the exponential trend:

$$\kappa(d,\lambda) = a(\lambda) \cdot e^{-b(\lambda)\cdot d}. \tag{5.1}$$

This program, by setting the geometrical parameters of the coupler, calculates the coupling coefficient for each segment dL of the curved section by making a guess on the parameters a and b and varying them in an iterative way until it finds the values that best fit the data obtained experimentally. The parameters a and b will later be used to simulate the power transfer trend for both wavelengths. Since κ changes with the wavelength, it follows that a and b will also change accordingly. In the fabrication L is fixed at 0, so that the initial phase can also be easily derived. In fact, just by inverting the formula in Equation 4.9a it is possible to derive the initial phase using the normalized power of bar at $L = 0$, as displayed in the following formula:

$$\phi_0 = \arccos\left(\sqrt{R_0}\right), \tag{5.2}$$

where R_0 is the normalized power at the reflection output port at $L = 0\,\text{mm}$ interaction distance.

After mounting the sample in the *fiber-butt* configuration, each coupler was then characterised by measuring the reflection (or bar transmission) according to the following formula:

$$R = \frac{P_{bar}}{P_{bar} + P_{cross}} \tag{5.3}$$

where P_{bar} and P_{cross} are the power measured by a powermeter at the bar and cross branch. The sum of P_{bar} and P_{cross} gives the input power P_{in} in the absence of losses.

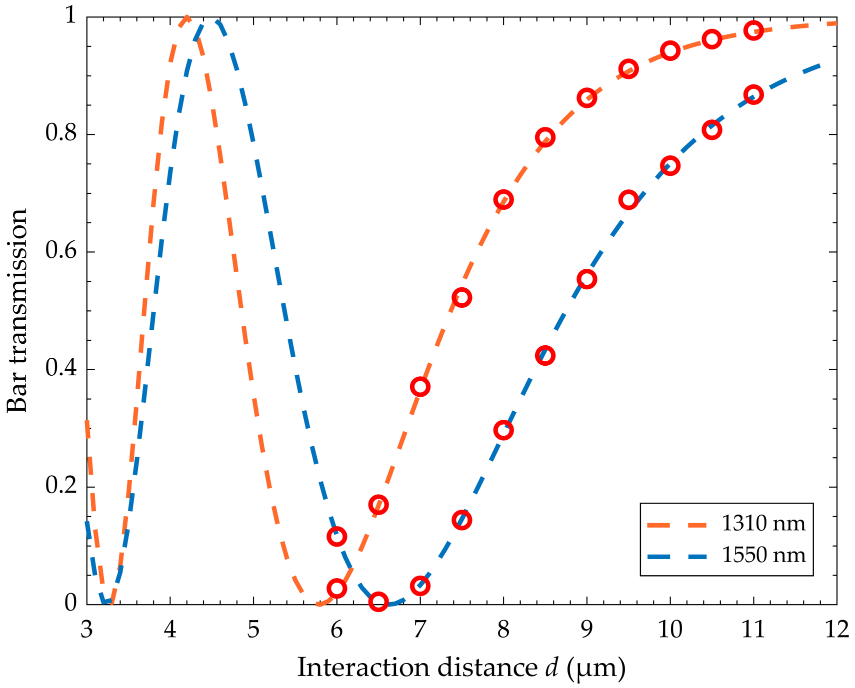

Figure 5.1: Experimental data of the Bar transmission in function of the interaction distance d, maintaining L fixed to $0\,\text{mm}$.

The characterization of the bar transmission as a function of the interaction distance d is reported in Figure 5.1. As expected, different values can be observed as a function of the working wavelength.

In addition, it is worth noting that a power transfer can occur even for an interaction length equal to 0 mm. This power transfer is related to the partial coupling of the evanescent field in the curved sections and it is represented by the initial phase ϕ_0 in the Equation 5.2. Therefore we have seen that analysing the group of couplers with d variable, by collecting the reflection data for each coupler, it is possible to derive the parameters a and b via Matlab, and thus to obtain κ for each interaction distance. Notice that κ could also be calculated by analysing the couplers with fixed d and variable L, as explained later, but this would mean that in order to obtain a reliable κ value it would be necessary to measure several points for a single d, and repeat it for different d values, whereas with the method adopted it is possible to obtain κ for any d with only 11 points.

Once the a and b parameters have been retrieved from the previous measurements, it is appropriate to verify the robustness of the simulation. For doing this, we fabricated a set of DCs with a fixed interaction distance d but different interaction length L, in particular varying L from 0 to 2 mm, every 0.2 mm. According to Equation 4.10, in this case the powers at the bar port will follow a cosine square trend. Experimental measurements (red dots) are reported in Figure 5.2. By fitting the experimental points (red dots) with a cosine squared fit (orange line), it is possible to derive κ and ϕ_0 from the following formula:

$$R = \cos^2 (\kappa L + \phi_0) \tag{5.4}$$

and compare it with the cosine squared trend simulated by Matlab (blue line), obtained by the a and b values previously calculated, thus verifying the robustness of the simulation. In Figure 5.2 it is visible the characterization of the couplers with d fixed at 8.5 μm, both for the wavelengths of 1550 nm (panel a) and 1310 nm (panel b), with also the simulated trend (blue line). The simulated trend deviates from the fitted trend with an error between the κ of 3.16% and 1.55% for 1550 and 1310 nm respectively.

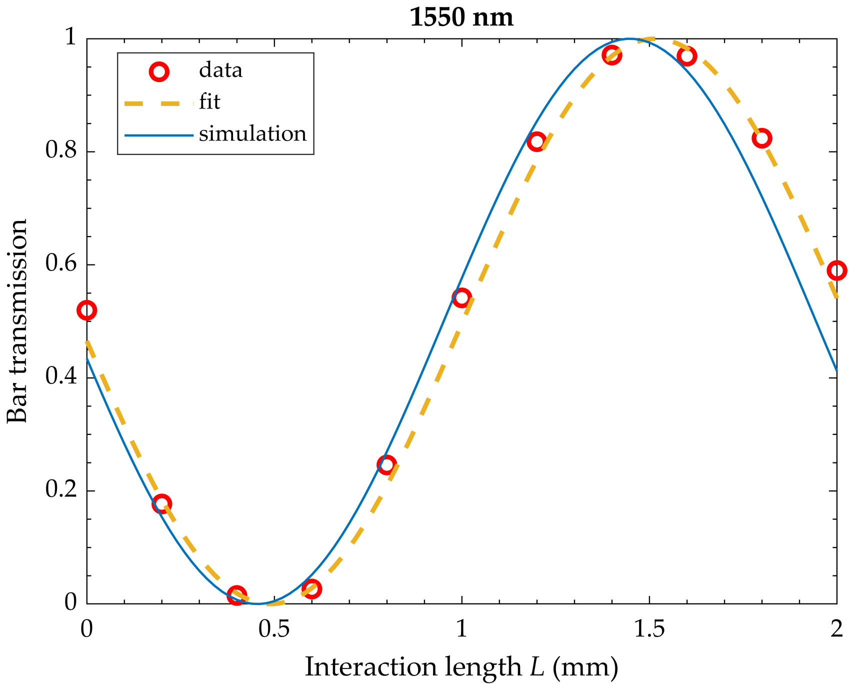

(a)

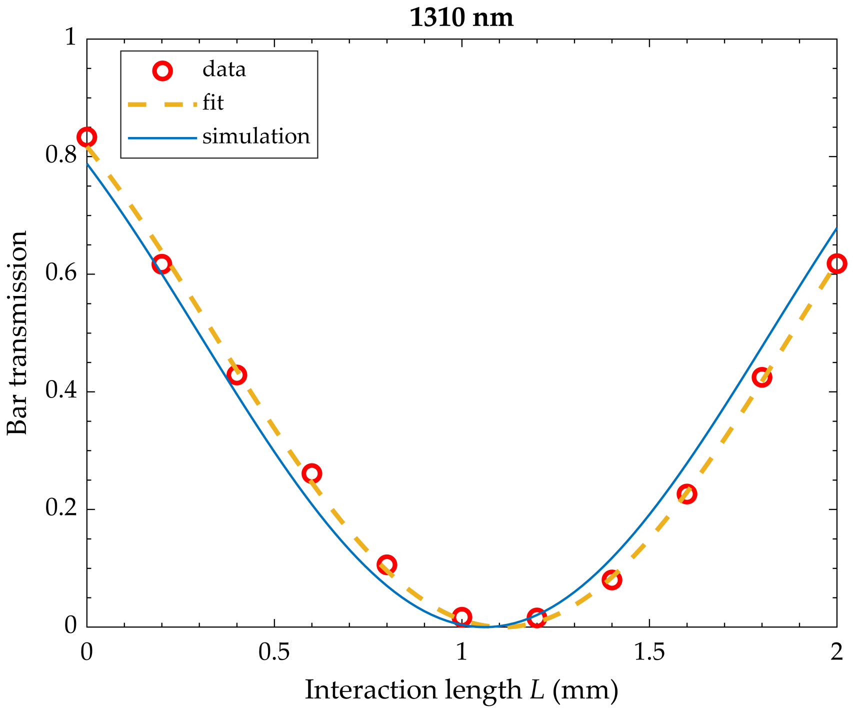

(b)

Figure 5.2: The figure shows the experimental reflection data (red dots) measured at 1550 nm on a sample in EAGLE XG for a coupler with 30 mm of radius and interaction distance of 8.5 μm. The orange line shows the $\cos^2$ fit while the blue line shows the sinusoidal trend simulated with the coupling coefficient calculated with Matlab. The deviation between simulated and fitted κ is of 3.16% at 1550 nm and of 1.55% at 1310 nm.

As previously stated, once a and b have been found, it is possible to simulate the sinusoidal trend of the power transfer in function of L for a coupler at any d and thus find the point of maximum division between λ_1 and λ_2, i.e. a WDM, as illustrated in Figure 5.3. For sake of completeness, the parameters a and b for 1310 and 1550 nm are reported in Table 5.2.

	a (mm^{-1})	b (mm^{-1})
1310 nm	42.50	437.59
1550 nm	25.16	325.47

Table 5.2: a and b parameters for 1310 and 1550 nm respectively.

Performing the simulations, i.e. entering the a and b parameters and observing the behaviour of WDMs for different d, it was seen that the most promising WDMs would come out adopting an interaction distance $\bar{d}$ equal to 11, 10.5 and 8 μm and an interaction length $\bar{L}$ of 4, 3.25 and 2 mm respectively. As a reference, it is possible to see Figure 5.3 which shows a simulation for $d = 8\,\mu$m. Couplers using others d showed the critical point at lengths L excessively long, for this reason they were discarded. The simulations have been performed without taking into account the error on κ since for small L, as in our case, the deviation between the maxima and minima in the bar transmission is negligible.

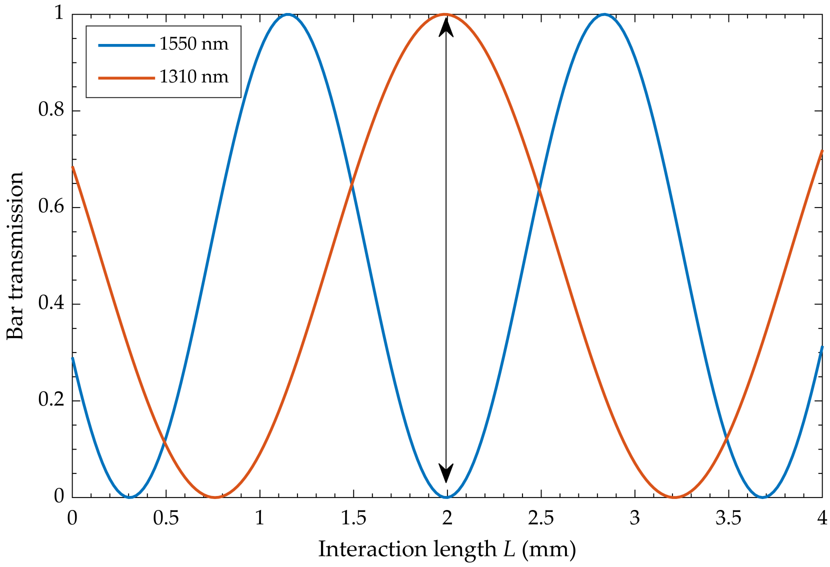

Figure 5.3: Simulation of the bar transmission for wavelengths of 1310 (orange line) and 1550 nm (blue line) as a function of interaction length L. In the figure it is possible to appreciate the point of maximum division of the two wavelengths (double arrow) at 2 mm.

At this point, a set of DCs featuring an interaction distance around $\bar{d}$ and an interaction length around $\bar{L}$ was fabricated. In particular, in order to take into account both run to run deviation in the fabrication process and the deviation in the simulated a and b values, we fabricated devices with several d ($\bar{d}\pm 0.1\,\mu m$) and L ($\bar{L} \pm x$ with steps of $0.05\,$mm). The characterization of the fabricated couplers is shown in Figure 5.4.

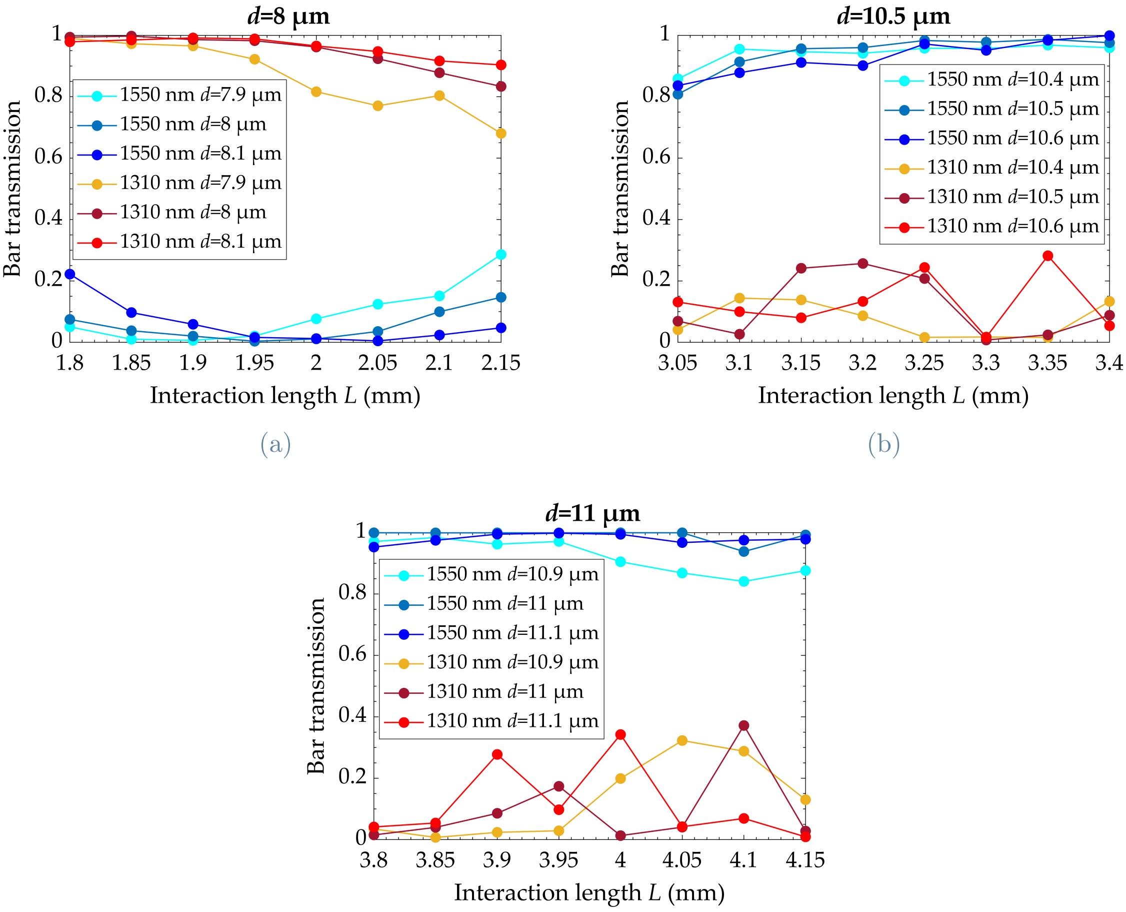

(a)

(b)

(c)

Figure 5.4: Sperimental data of the WDMs indicated by the simulations. The WDMs were fabricated at an interaction distance $d = 8\,\mu$m panel (a), $d = 10.5\,\mu$m panel (b) and $d = 11\,\mu$m panel (c).

Subsequently, according to the characterization showed in Figure 5.4, the DC that proved to be more robust during fabrication and with a sharper wavelength separation was selected, namely the coupler with $d = 8\,\mu$m. Indeed, for bigger interaction distances (see panel b and c), the splitting behaviour at 1310 nm was extremely noise. This phenomenon was not investigated, but it may be related to the longer interaction length of these devices, which makes them more sensitive to the fluctuations of the fabrication process. In order to precisely find the point of maximum division of the two wavelengths, the final device was fabricated by performing a scan around the optimal L parameter using a finer step of 0.025 mm. The behaviour of the bar transmission as a function of the interaction length L for the final device is reported in Figure 5.5. Experimental points are represented by orange and blue dots for 1310 and 1550 nm wavelength, respectively.

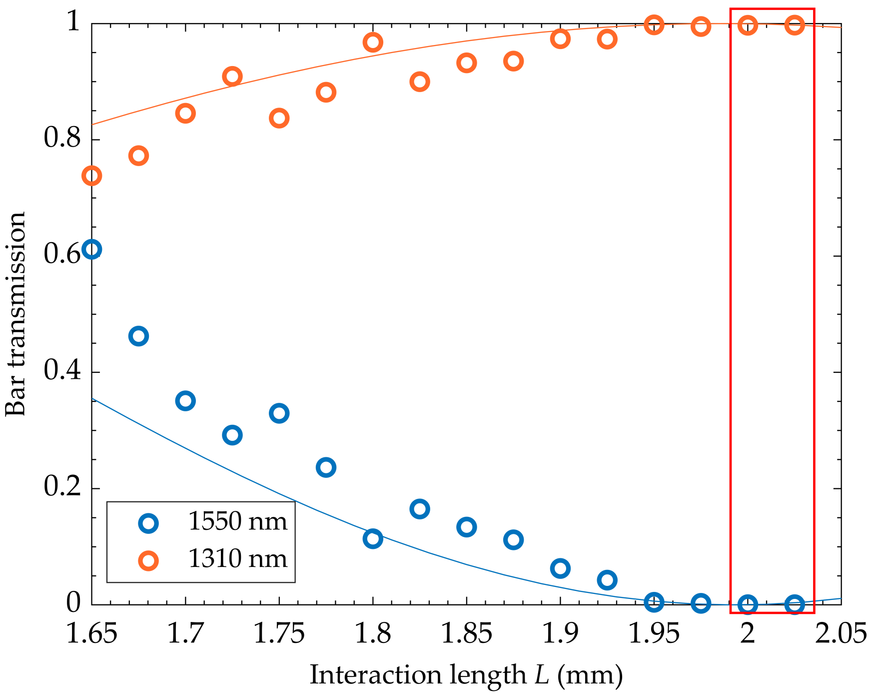

Figure 5.5: Bar transmission measurements for wavelengths of 1310 and 1550 nm for coupler with $d = 8\,\mu$m and L variable from 1.65 to 2.025 mm with a step of 0.025 mm. The solid lines represent the simulations. The red rectangle identifies the region where the ER will be measured.

The solid lines in Figure 5.5 represent the magnification of Figure 5.3, showing L from 1.65 to 2.05 mm. From Figure 5.5 it is possible to appreciate how the experimental points reach the critical point as predicted by the simulation, proving its reliability.

Only if a coupler showed a pronounced wavelength division behaviour, i.e. bar transmission values above 99.9% (below 0.1%) for λ_1 (λ_2), we proceeded with the measurement of its extinction ratio (ER) as explained in section 3.2.5. In particular, we measured the extinction ratio for the last two couplers in Figure 5.5, featuring $d = 8\,\mu$m and $L = 2$ mm and $L = 2.025$ mm, respectively. The measured ER are reported in Table 5.3.

Extinction Ratio		
	$L = 2\,\mathrm{mm}$	$L = 2.025\,\mathrm{mm}$
1310 nm	22.36 dB	25.15 dB
1550 nm	24.07 dB	19.85 dB

Table 5.3: ER of WDM for 1310 and 1550 nm.

The measurement resulted in ER values of 22.36 dB and 24.07 dB for $L = 2\,\mathrm{mm}$ and 25.15 dB and 19.85 dB for $L = 2.025\,\mathrm{mm}$, for the wavelength of 1310 and 1550 nm respectively. The splitting of the 1310/1550 nm photon pair with ER values above 20 dB represent one of the best results that it is possible to find in literature for WDM fabricated by FLM technique.

5.2. WDM for photon pair in the S- and L-band

Simulations on the single-photon source, performed by a colleague and thus not reported in this thesis, revealed that photon pairs emitted in the S- and L-bands (1460-1530 nm and 1565 to 1625 nm) are found to have higher purity than photon pairs in the O- and C-bands (1260-1360 nm and 1530-1565 nm, i.e. the wavelengths of the WDM fabricated before). For this reason, we examined the feasibility of fabricating a WDM for pair belonging to the S- and L-band. However, dividing photon pairs belonging to wavelengths that are close together results in a more difficult task.

The principle behind the operation of a WDM is that the coupling coefficient is wavelength-dependent and thus the argument of the cosine squared being different, leads to different periods of power transfer, reaching sooner or later a point of maximum division for the two wavelengths, even if the critical point with a successful division is not always guaranteed. This wavelength-dependent means that, in the range of wavelengths involved, the more different the wavelengths are, the more different the κ's are. The greater the difference in the coupling coefficient ($\Delta\kappa$), the more compact a WDM can be obtained, since the two bar transmission of the two wavelengths have to make fewer cycles to be completely separated.

Therefore, for the realization of WDMs in this range, it is first necessary to conduct a more detailed study of the wavelength dependence of κ, in order to see the sensitivity of variation of κ with the wavelength and thus be able to predict the behaviour in that range.

So for a more detailed study of κ's dependence on λ it is necessary to refer to the coupled mode theory. From the coupled mode theory it is known that the coupling coefficient has a wavelength dependence through the formula [133]:

$$\kappa = \frac{{k_0}^2}{2\beta_{\mathrm{n}}} \frac{\iint \psi_{\mathrm{m}} \Delta n^2 {\psi^*}_{\mathrm{n}} dxdy}{\iint \psi_{\mathrm{m}} {\psi^*}_{\mathrm{n}} dxdy} \tag{5.5}$$

where the integration is carried out over the cross section of one of the waveguides. β_0 is the propagation constant of individual waveguides, Δn is the difference in refractive indices between substrate and waveguides and $\psi_{\mathrm{m,n}}$ are the electric field distributions.

Since it is not trivial to study the formula 5.5 analytically, we will proceed by analysing the coupling coefficient using an experimental approach. First of all, following the procedure reported in section 5.1, several directional couplers were fabricated with interaction length L equal to 0 and scanning the interaction distance d. In particular, data were acquired for interaction distances from 6 to 11 μm. The reflections were then measured using a Santec MLS-2000 tunable laser in the range from 1510 to 1588 nm. After this, in order to retrieve the parameters a and b, the reflection data were analysed with the Matlab program, as explained in section 5.1. For sake of completeness, the parameters are listed in Table 5.4.

	a (mm^{-1})	b (mm^{-1})
1510 nm	27.07	337.74
1530 nm	24.53	322.09
1550 nm	23.44	313.98
1570 nm	23.10	309.70
1588 nm	25.08	317.39

Table 5.4: a and b parameters for 1510, 1530, 1550, 1570 and 1588 nm respectively.

After this thorough characterization, it was possible to calculate the coupling coefficient for all d at the various wavelengths. Once κ's were calculated, a linear relation between κ and λ has been observed in Figure 5.6. In figure 5.6 are reported the κ's trends for coupler at $d = 6\,\mu$m, $d = 8.5\,\mu$m, and $d = 11\,\mu$m for clarity. A linear regression was performed for each of those interaction distances, resulting in the equations presented in the following:

$$\kappa(\lambda) = (1.92 \cdot 10^{-3} mm^{-1} nm^{-1})\lambda + 0.64 mm^{-1} \tag{5.6a}$$

$$\kappa(\lambda) = (1.92 \cdot 10^{-3} mm^{-1} nm^{-1})\lambda - 1.37 mm^{-1} \tag{5.6b}$$

$$\kappa(\lambda) = (1.58 \cdot 10^{-3} mm^{-1} nm^{-1})\lambda - 1.34 mm^{-1}. \tag{5.6c}$$

Even thought these equations are valid only within the measured wavelength range and possible deviations may occur at wavelengths outside, thanks to this analysis we can retrieve the coupling coefficient κ for a wavelength range of almost 80 nm (from 1510 nm to 1588 nm) by acquiring only 5 set of experimental points.

It is possible to notice that $\Delta\kappa$ between 1510 to 1588 nm are 0.16, 0.1 and 0.096 mm^{-1} for the interaction distance of 6, 8.5 and 11 μm respectively, allowing the fabrication of WDMs of lengths of around 1 cm, as visible in Figure 5.7. From the data it can be stated that by increasing the interaction distance d, the wavelength sensitivity decreases.

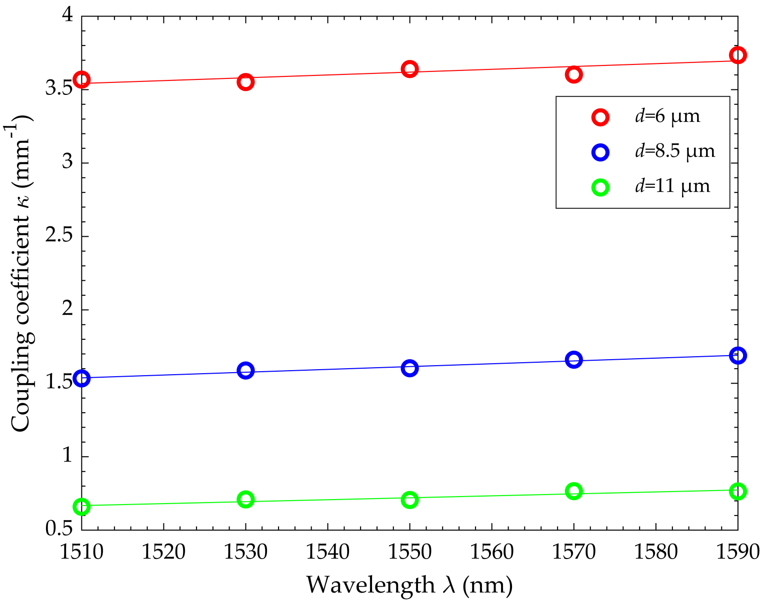

Figure 5.6: Coupling coefficient in function of wavelength. In figure are reported the linear regression for the coupling coefficient for couplers with interaction distance of 6, 8.5 and 11 μm.

Once the wavelength dependence of κ has been measured and the parameters a and b have been derived, it is possible to start fabricating the WDMs. The WDMs in question will be fabricated for wavelengths of 1510 nm and 1588 nm, i.e. the extremities of the wavelength range we have characterised, in order to have $\Delta\kappa$ as large as possible. So we proceeded running simulations using parameters a and b for the wavelengths of 1510 and 1588 nm, obtaining optimal WDM using interaction distance around $d = 8\,\mu$m. The simulation can be seen in Figure 5.7. Using the procedure used for the previous device, we found a directional coupler behaving as a WDM for $d = 8.25\,\mu$m and $L = 9.82$ mm. The ER was then measured, disclosing a value above 15 dB for both wavelength, as reported in Table 5.5.

Extinction Ratio	
1510 nm	17.2 dB
1588 nm	15.9 dB

Table 5.5: ER of WDM for 1510 and 1588 nm.

As expected, this value is significantly lower than the ER calculated for wavelengths in the O- and C-band. This is because, as mentioned before, for wavelengths close to each other, longer interaction lengths are required to obtain a WDM behaviour. It follows that the device will be more affected by fabrication and simulation errors. Indeed, this device is almost 5 times longer than the one fabricated for splitting 1310 nm wavelength from 1550 nm wavelength. For this reason, errors in the prediction of κ and fluctuations in fabrications are carried along for a longer length, deviating the maxima and minima points of the bar transmission more significantly from the actual values. It can be noted that the critical point expected from the simulations was at $d = 8\,\mu$m and $L = 9.44$ mm, as shown in Figure 5.7, while the actual critical point was found at $d = 8.25\,\mu$m and $L = 9.82$ mm. In any case, by taking into account and compensating for the different source of errors, we were able to fabricate a WDM in line or even better than others fabricated with the same platform [67, 132].

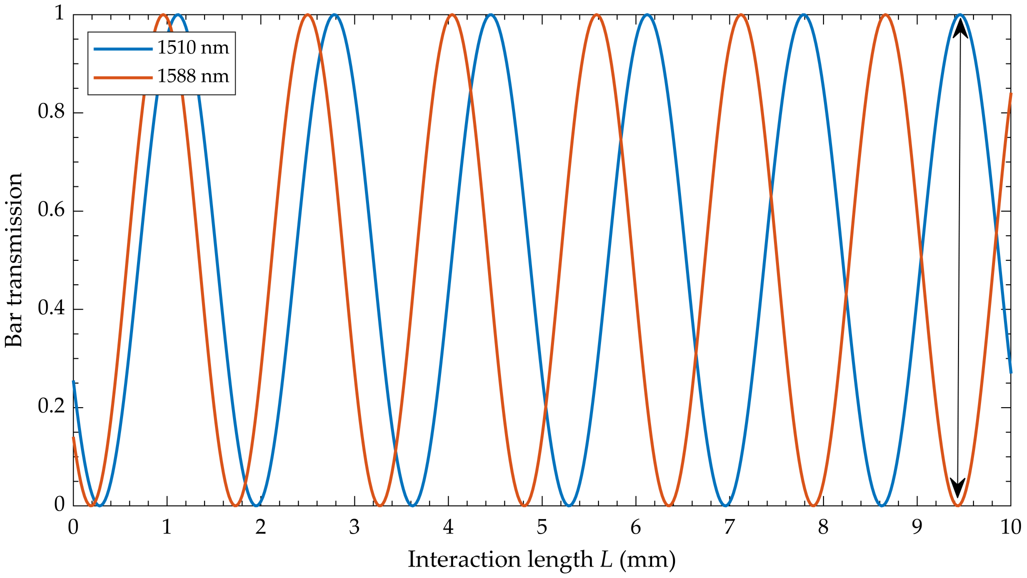

Figure 5.7: Simulation of the bar transmission for wavelengths of 1510 and 1588 nm as a function of interaction length. The critical length for the WDM is of 9.44 mm.

6 | Development of Waveguides Writing in Borofloat Glass

This chapter deals with the development of a fabrication process for a photonic platform based on Borofloat 33 glass and its employment in the realization of a WDM. Initially, in section 6.1 a motivation for justifying the change of material is provided. Subsequently, in section 6.2 an optimization for straight waveguides, curved waveguides and directional couplers for wavelengths around 1550 nm is performed. Finally, in section 6.3 a WDM is realized for the wavelengths of 1510 and 1588 nm.

6.1. Motivation

Low losses are a fundamental requirement for a successful Scattershot Boson Sampling (SBS) experiment, and not only in that experiment, but in all integrated photonics. To give an idea of the importance of losses in this experiment we can roughly estimate the timescale for a successful BS experiment in the case of high losses and low losses. Imagine to realize a device in a platform (A) with losses that are about one order of magnitude higher than the one of the same device but in another platform (B) and to put it in the optical path of a BS experiment. Let also assume that the probability of generating one photon-pair is $p = 0.01$. Assuming constant all the other parameters of the experiment (e.g. generation rate, detection rate), the probability to detect a single photon at the output will be ten times higher for the configuration with device B. So, assuming that for the configuration with material A we have on average a detected photon at the output every $30\,\mu$s, for configuration B we will have about one photon every $3\,\mu$s. For example, to obtain 4 simultaneous photons, the probability becomes p^4, i.e. to get four simultaneous photons it is necessary to generate about 10^8 photons. In case A it takes 50 minutes, while in case B it takes 5 minutes. If the desired simultaneous photons are 5 or 6 then the times would increase to 3.47 days and almost 1 year for A and 8.3 hours and 1 month for B, respectively. So having low losses would save a huge amount of time in the success of the experiment.

For this reason, instead of using the well-known EAGLE XG glass as platform, we are studying a new material (Borofloat 33 glass) that is expected to show lower propagation losses. Indeed, according to the optical datasheet of the two materials, Borofloat shows slightly higher optical transmission with respect to EAGLE XG. Borofloat 33 (EAGLE XG) has a chemical composition of 81% (59.7%) SiO_2, 13% (12.27%) B_2O_3, 4% Na_2O/K_2O ($< 0.01\%$) and 2% (17.1%) Al_2O_3 (and 7.3% CaO) [134–136]. Borofloat 33 has a refractive index at 1030 nm of 1.463, which is lower than EAGLE XG's refractive index, which is 1.5 at the same wavelength.

6.2. Optimization Process

Since we need to investigate whether Borofloat would be a good alternative to EAGLE XG it is necessary to find optimal waveguides for the desired wavelength. Since the generated photons are in the range of 1550 nm, the optimization will be performed for that wavelength. A good waveguide, in addition to having low propagation losses, must also have low bending losses and must be able to couple to other waveguides. In this section these three requirements will be analysed.

6.2.1. Straight Waveguides

As in all optimisation processes, in order to find the tailored parameters to obtain the waveguide with the desired properties, it is necessary to proceed by fabricating several straight waveguides by doing an extensive scan on several parameters.

During the whole optimization procedure, some parameters remained unchanged, such as repetition rate at 1 MHz, the use of a compensated 50x objective with numerical aperture NA of 0.6 and the polarization of the laser beam. Indeed, these parameters had represented a good starting point also for the optimisation of the fabrication process of other materials. In addition, exploring the whole space of possible parameters at the same time will turn out to be excessively time consuming. In general, it is better to focus on a subset of possible parameters. The unchanged parameters will represent additional knobs in case the optimisation process will not lead to satisfactory results. The first two fabrications were performed by sweeping a wide range of powers, from 650 to 1590 mW in total, examining four different scan parameters (1, 3, 5, 7 scans) and using a total of four write speeds, from 25 up to 80 mm/s. From these fabrications, it was possible to define a window of optimum values, i.e. powers from 650 to 750 mW, with three scans values (3, 5, 7 scans) at two different speeds, 40 mm/s and 60 mm/s. In fact, it was seen that increasing the power above 750 mW, while maintaining the above parameters, resulted in multimode waveguides. Same behaviour by lowering the writing speed. However, by lowering the power, the modification of the material was not sufficiently strong to allow the propagation of light, in fact below 650 mW very high losses were experienced.

Once the optimal window was found, a measurement on a 10 cm sample was performed in order to have a rough, but significant estimation of IL. The insertion losses of a 10 cm sample are shown in Figure 6.1. Once IL has been measured on the 10 cm sample, we decided to precisely retrieve coupling losses and propagation losses through the so-called cut-back method. Since this method is quite time consuming, we decided to discard the waveguides with IL above a threshold. The threshold was arbitrarily set at 0.75 dB, so 11 waveguides were selected for further investigation.

CL and PL calculated for these waveguides are reported in Figure 6.2. From the graph, it can be seen that all the waveguides present very low propagation losses, with values of approximately 0.023 dB/cm up to 0.037 dB/cm. These values are almost an order of magnitude lower than the PLs values found in the literature for EAGLE XG.

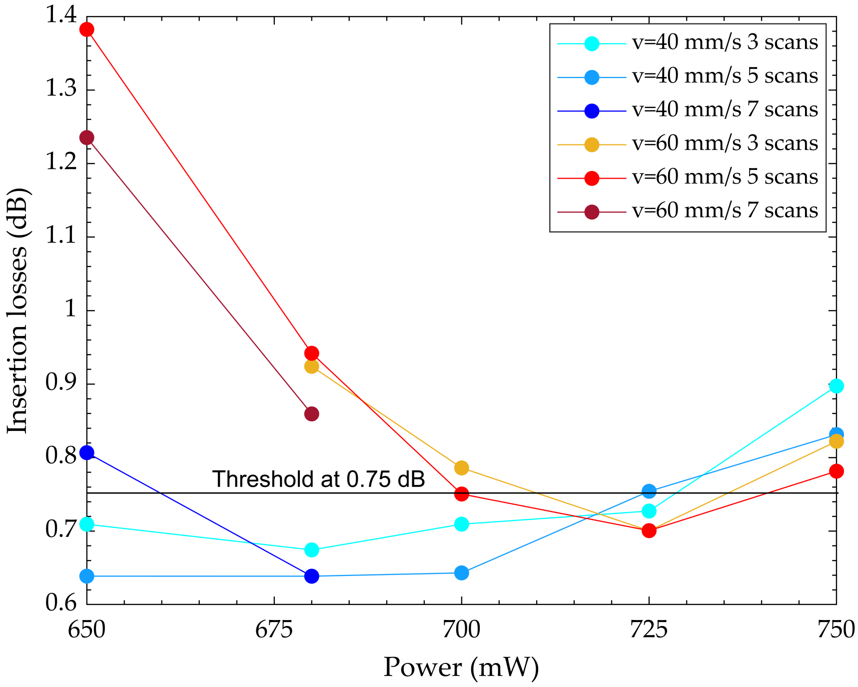

Figure 6.1: Insertion losses for a 10 cm sample for different fabrication parameters. To shorten the cut-back procedure, only the waveguides with IL losses lower than a threshold of 0.75 dB were selected for further investigations and measurements.

The mode profiles were then measured using the method explained in section 3.2.3. The modes turn out to have a Gaussian-like profile with mode diameters of around 12.5 μm (see Table 6.1 for reference), and tend to be slightly elongated along the laser incidence axis, as shown in Figure 6.3. The overlap integrals between the mode profile of the fiber and the waveguides are estimated at values around 85%, which justifies the particularly high value of the CLs.

Since all waveguides show very promising values of PLs, before proceeding with the optimization of bending losses, it is convenient to further select a subset of waveguides. In general, we did not select the processing parameters that allow the fabrication of the waveguides with the lowest PLs, since not always the best guides in terms of propagation losses correspond to the best waveguides in terms of bending losses. In particular, in the selection we took into account also the guided mode profile. Indeed, waveguides with smaller modes tend to have a higher index contrast, which turns out into lower bending losses at fixed radius. In conclusion, we selected the waveguides that show the best trade off between CLs, guided mode size and PLs. The three selected waveguides are highlighted with a red cicle in Figure 6.2. Corresponding values of mode sizes, CLs and

PLs are reported in Table 6.1. Guided mode profiles and micrograph of waveguides' cross sections are reported in Figure 6.3.

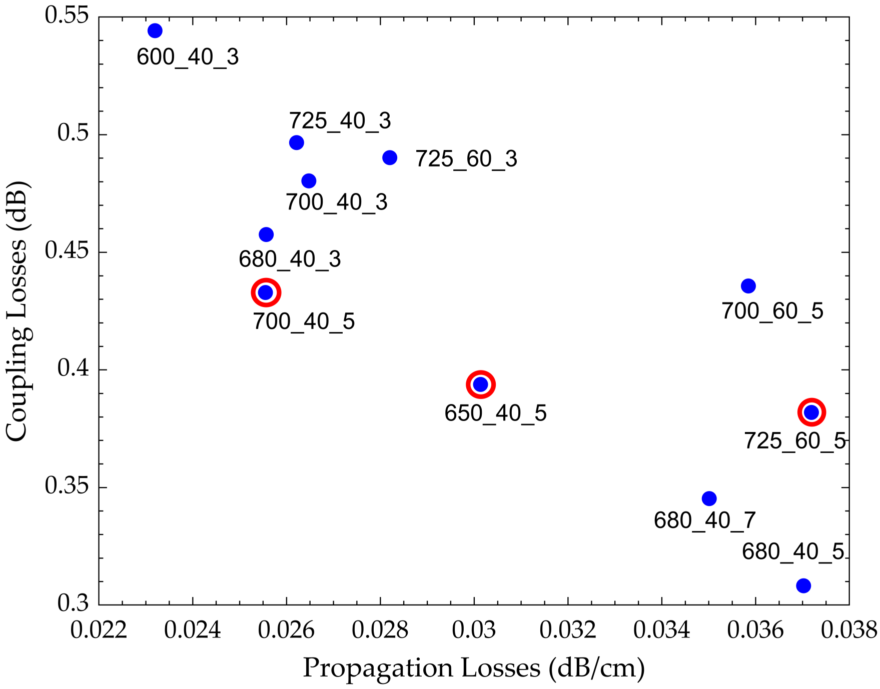

Figure 6.2: Coupling losses and propagation losses derived after a cutback. The nomenclature stands for power(mW)_velocity(mm/s)_scans. The three red circles indicate the waveguides selected for subsequent bend optimization.

Power (mW)	**Speed** (mm/s)	**Dimension** ($\mu m \times \mu m$)	**CL** (dB)	**PL** (dB/cm)
650	40	12.4 ×12.3	0.39	0.030
700	40	12.4 ×13.7	0.43	0.025
725	60	12.6×12.9	0.38	0.037

Table 6.1: Straight waveguides data obtained after the cutback. Mode dimension, coupling losses and propagation losses for the three best waveguides are shown. All the three waveguides have been fabricated with a number of scans equal to 5.

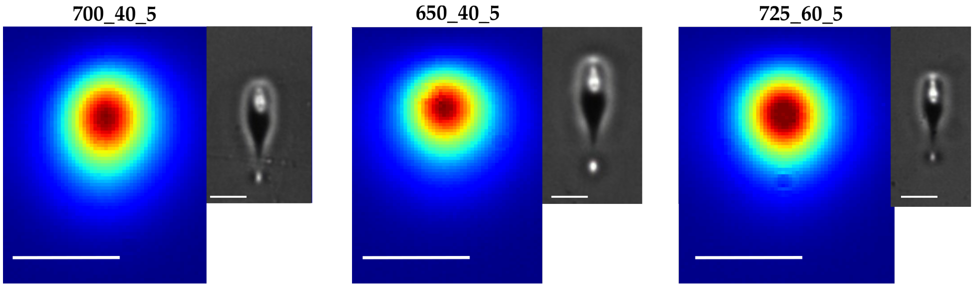

Figure 6.3: Mode profile and cross section of selected guides. Each image contains mode size and overlap integral to the fiber mode. Scale bar is 10 μm.

Before proceeding with the analysis of bending losses, it is better to highlight a feature in this fabrication process of Borofloat 33 that emerged during different fabrications. In particular, it turned out that the fabrication process is extremely sensitive to the writing depth. Typically, we write waveguide at 50 μm from the bottom surface of a 900 μm thick samples with a 50x objective encompassing a compensation collar to reduce effect of abberations. The sample, as provided by the supplier, have a tolerance in the thickness value of ±20 μm. It means that it is possible to fabricate in thicker or even thinner glass substrates. In the latter case, it follows that the portion of glass traversed by the laser is reduced. It has been observed that, keeping fixed all the parameters, when the writing depth is smaller than about 840 μm, the waveguide cross-section starts presenting unusual dots (probably micro-voids), as shown in the microscope picture reported in Figure 6.4. These dots are centres of scattering, thus causing an increase in the propagation losses. The cause of the formation of the dots is not yet known, but in a first hypothesis it could be due to an excess of deposited energy. In fact, the shorter the distance crossed by the laser inside the sample, the less energy is absorbed and lost during propagation and thus higher is the energy deposited in the focal point.

On the other hand, if the distance is greater, the deposited energy could be not sufficient to create the refractive index modification and therefore the waveguide losses increase. Furthermore, it is always safe to maintain a margin of about 20-30 μm from the surface, to avoid effects of water-substrate discontinuity. For this reason, the successive fabrications in Borofloat 33 were performed by writing at a fixed distance from the top surface, i.e. 850 μm from the top surface. However, before each fabrication it is necessary to check the thickness of the sample, to make sure that we do not write too close to the bottom surface and check whether there are any creases in the sample, which are usually more present and pronounced in 10 cm long samples, in order to properly take a reference point so as not to end up close to the bottom surface or even exit during the writing. In order to compensate the effect of the bow, a program that map the surface of the substrate can be adopted.

An optimisation in its functioning would represent a possible solution to circumvent this problem, but further investigations are required. Indeed, a first fabrication round has led to higher *ILs*. Therefore in Borofloat 33 there is an optimal window of writing depth. Such a high depth sensitivity could be a huge drawback, as it could compromise the three dimensional capability of femtosecond laser writing. As 3D capability is not strictly required for our WDM filter, we will leave the analysis on depth insensitivity to future optimisations.

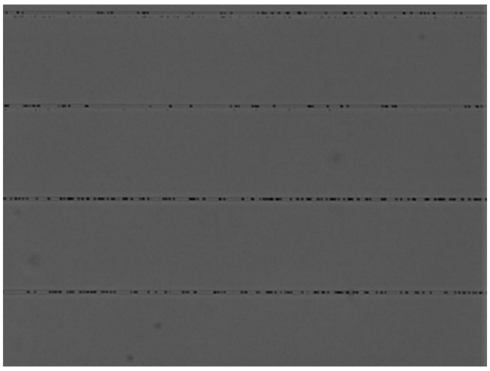

Figure 6.4: Demonstration of high sensitivity to writing depth. Waveguides containing dots probably due to excessive deposited energy.

6.2.2. Bending Losses

As miniaturization is an important feature of photonic platforms and standard devices for quantum information processing encompass a high number of interacting modes and bends [35], an optimisation on bending losses is necessary.

To measure the bending losses, a method similar to the one explained in section 3.2.4 was used. In particular, instead of inscribing S-bends of length l_c, it was decided to fabricate serpentines, i.e. numerous S-bends in series. This gives a better idea of the possible losses for a future hypothetical device composed of numerous curved sections and moreover, in this way, greater lengths of the curved section are achieved, resulting in a better estimation of *BL*. Exploiting the processing parameters of the three previously selected waveguides, we fabricated a sample with several radii of curvature: 60, 40, 30, 20, 15 mm.

The characterization of serpentine waveguides is reported in Figure 6.5. In panel (a) we report on the *ILs* of a 10 cm device, while in panel (b) we report on the corresponding *BLs*.

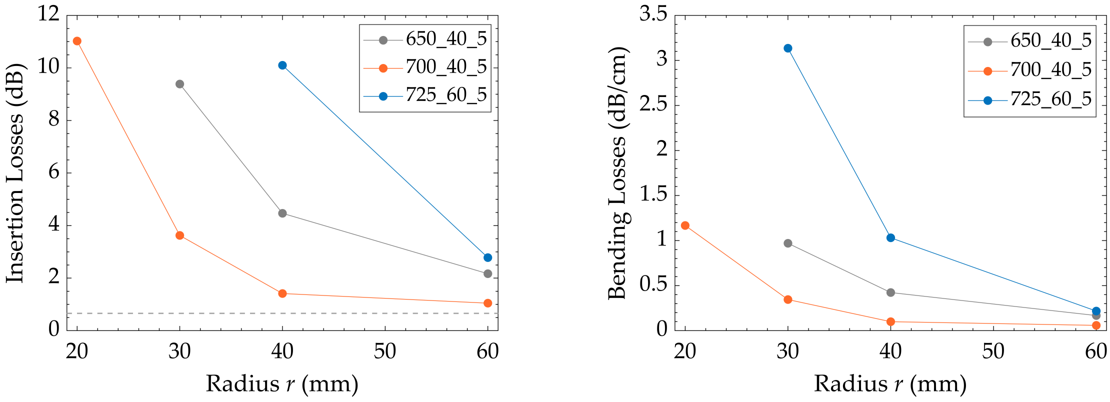

(a)

(b)

Figure 6.5: Insertion losses (a) and bending losses (b) for the sample containing serpentines with different radii of curvature for the three selected waveguides. The nomenclature stands for power(mW)_velocity(mm/s)_scans. The dotted line in (a) indicates the IL of the straight waveguide inscribed at 650 mW and is used as a reference to indicate the ILs of the straight waveguides, which are around that value.

From the two graphs it can be seen that the ILs and BLs are lower for the waveguide fabricated with 700 mW at 40 mm/s with 5 scans (orange line), in fact the IL for a 10 cm sample of the straight waveguide is 0.52 dB, increasing to 1.05 dB, 1.41 dB and 3.62 dB for radii of 60 mm, 40 mm and 30 mm respectively. For the other two processing parameters, waveguides show a bigger exponential factor, featuring ILs above 4 dB already for radii of 60 mm, and thus much higher bending losses. Indeed, data of serpentine waveguides at radius 20 mm are out of scale and thus are missing in the graph. For the same reason, the data for the 15 mm radius of curvature are missing for all waveguides. It was found that in order to have a negligible amount of bending losses, radii of 60 mm must be used for the waveguide fabricated with 700 mW at 40 mm/s with 5 scans, obtaining BL of 0.06 dB/cm. However, it is possible to reduce the radius to 40 mm, obtaining BL of 0.1 dB/cm, allowing more compact devices to be realised. The BLs of the other two waveguides were found to be around 0.2 dB/cm for radii of 60 mm, therefore proving to be not suitable for devices containing many curves.

6.2.3. Directional Couplers

Once the waveguide with the optimum parameters has been found, it only remains to examine the waveguide coupling behaviour, as WDM is based on that.

The geometry of the couplers is the same adopted in section 5.1, i.e. planar couplers, with a distance between the non-interacting waveguides of $127\,\mu m$. We then proceeded to manufacture directional couplers with the parameters shown in the Table 6.2.

Fabrication Parameters	
Substrate	Borofloat 33
Laser System	Yb:KYW cavity dumped
Wavelength	1030 nm
Repetition Rate	1 MHz
Writing Power	700 mW
Translational Speed	40 mm/s
Number of Scans	5
Writing Depth	850 μm from top
Objective	50x CC

Table 6.2: Table containing the fabrication parameters.

The first set of couplers consists of 11 couplers with $L = 0$, but scanning the interaction distance from 6 to $11\,\mu m$ with a step of $0.5\,\mu m$. As shown in Figure 6.6, from these measurements it is possible to appreciate the trend at the bar port as a function of the interaction distance d and then derive the parameters κ and ϕ_0, through the method explained in the section 5.1. Through the graph it is possible to confirm that these are synchronous DCs, since all the power is transferred at the cross port for interaction distance between 8 and $9\,\mu m$.

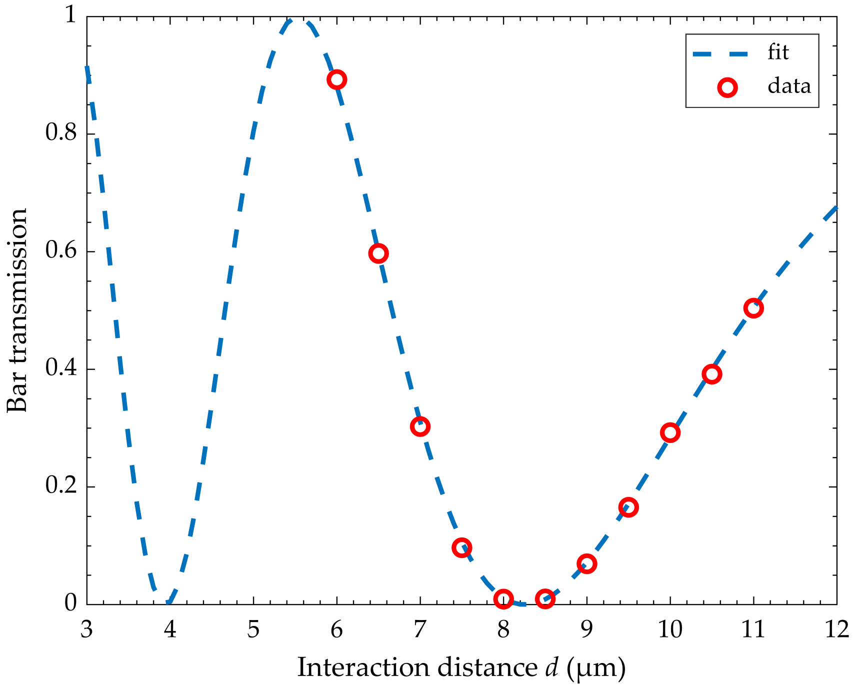

Figure 6.6: Normalized power at the Bar output port as a function of interaction distance. The experimental data are dotted with red circles while the dashed line represents the fit processed by Matlab.

Two other coupler groups were then fabricated on the same sample, keeping d constant and varying L from 0 to 2 mm, with a step of 0.2 mm. It is possible to appreciate the $\cos^2$ trend in Figure 6.7 where the data of the couplers at $d = 6.5\,\mu$m (panel a) and $d = 9\,\mu$m (panel b) are shown. As a reference, a $\cos^2$ fit is also reported. This fit can then be compared with the values obtained from the simulation based on the κ and ϕ_0 parameters retrieved by processing the data of the first set of couplers in Figure 6.6. In Figure 6.7 it is possible to observe the comparison between the two curves (dashed line vs. solid line). The simulation tends to overestimate κ, resulting in a percentage variation of 2.81% for $d = 6.5\,\mu$m and 5.96% for $d = 9\,\mu$m.

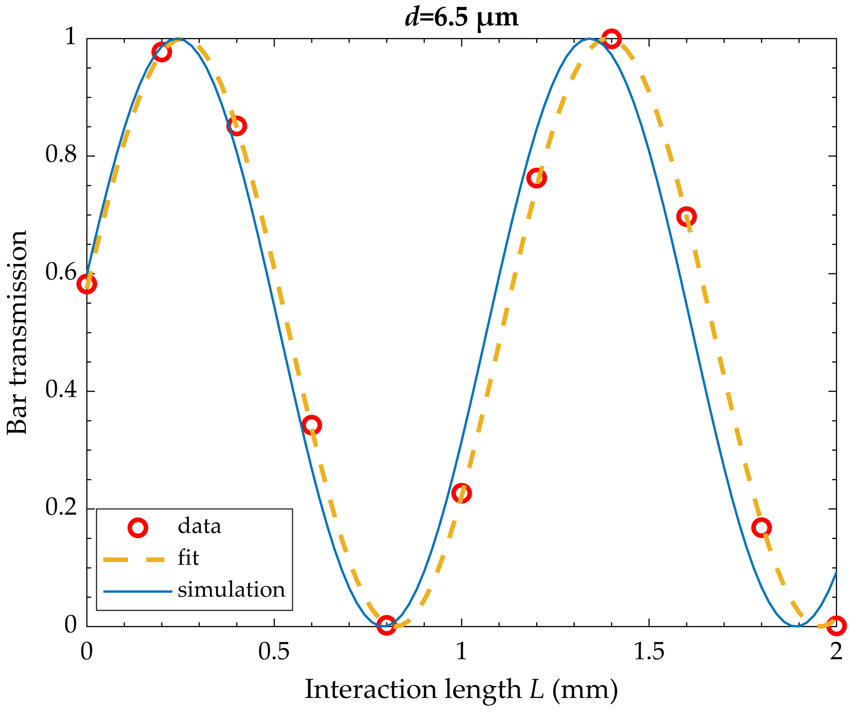

(a)

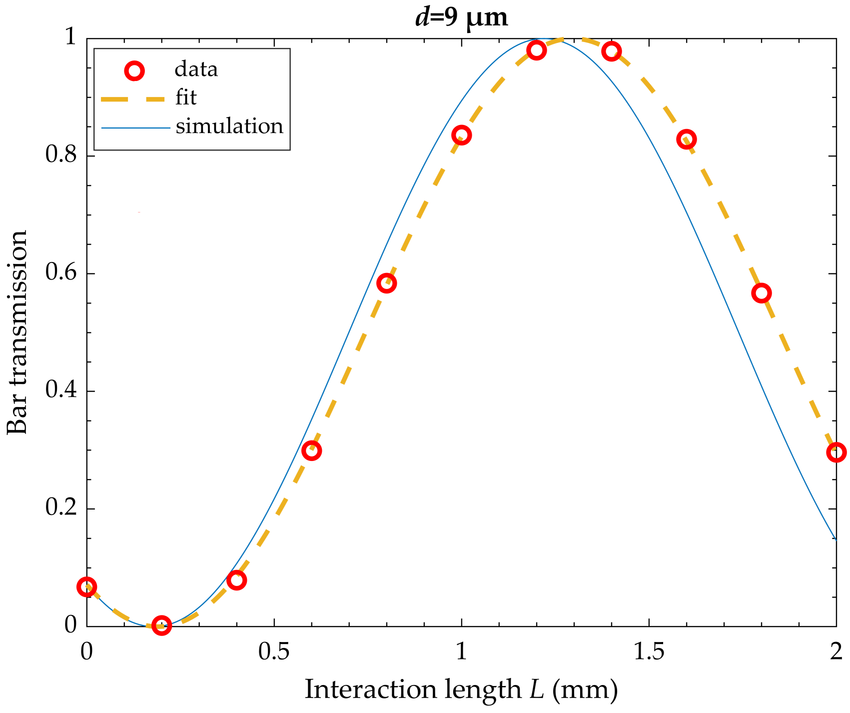

(b)

Figure 6.7: Normalized power at the Bar output port as a function of interaction length L. The two graphs show the data collected from the two sets of couplers at $d = 6.5\,\mu$m (a) and $d = 9\,\mu$m (b), depicted by the red circles. The dotted line represents the $\cos^2$ fit while the solid line represents the simulation, obtained from the parameters retrieved from Matlab.

As with EAGLE XG, the trend of κ as a function of wavelength was derived. So as explained in section 5.2 the parameters a and b were obtained for five different wavelengths from 1510 to 1588 nm. Then κ was calculated by means of the Equation 5.1 and thanks to the five points it was possible, through a linear regression, to determine the linear trend of the coupling coefficient as a function of wavelength, as reported in Figure 6.8. Furthermore, thanks to the a and b parameters, it is possible to simulate the trend of the power transfer for the different wavelengths and thus obtain the values for the fabrication of a WDM, as will be detailed later. The parameters a and b for the different wavelengths are listed in Table 6.3

	a (mm^{-1})	b (mm^{-1})
1510 nm	16.25	269.19
1530 nm	15.24	258.66
1550 nm	14.95	254.76
1570 nm	14.18	246.58
1588 nm	13.37	238.33

Table 6.3: a and b parameters for 1510, 1530, 1550, 1570 and 1588 nm respectively.

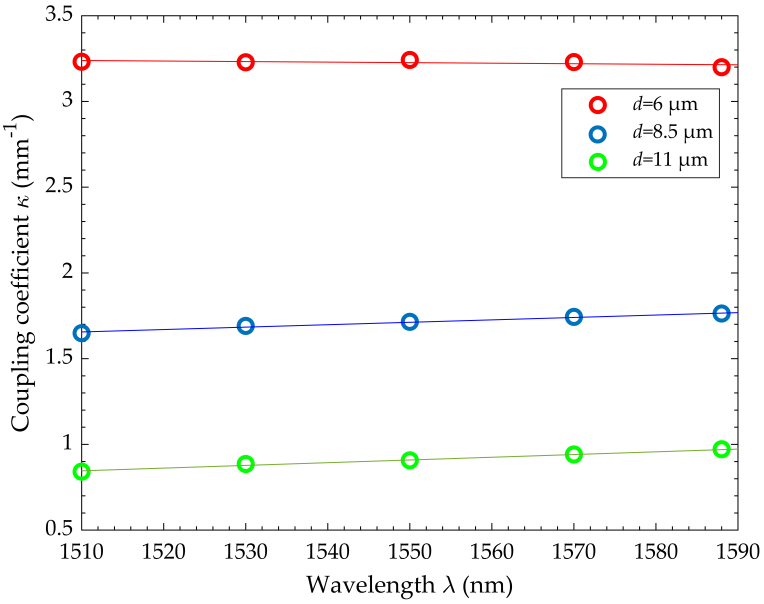

Figure 6.8: Coupling coefficient as a function of wavelength in Borofloat 33. Three different linear regressions are presented for coupler at $d = 6\,\mu$m (red), $d = 8.5\,\mu$m (blue), $d = 11\,\mu$m (green).

6.3. WDM Fabrication and characterization

The WDM to be fabricated is for the wavelengths of 1510 nm and 1588 nm. Therefore, following the same procedure of section 5.1, taking the a and b values previously calculated for 1510 and 1588 nm, several simulations were performed to find the point of maximum extinction ratio at minimum length between the two wavelength. In particular, WDMs were simulated using interaction distances from 6 to 11 μm with a step of 0.5 μm, and a maximum split point was found for a simulated coupler with $d = 10.25\,\mu\text{m}$ at $L = 9.9$ mm, as shown in Figure 6.10. Subsequent fabrications, using the same parameters previously reported, were then carried out around those values, also taking into account the overestimation in the simulations of the κ value of the Matlab program. The fabrications produced a WDM with $d = 10.25\,\mu\text{m}$ and $L = 9.44$ mm. Later, using the method explained in section 3.2.5 an ER of 19 dB was measured for both wavelengths. This ER is better than the one obtained for EAGLE XG and in line with the best values for WDM fabricated by FLM. In addition, since the length of the filter is almost equal to the one in EAGLE XG and propagation losses are almost 10 times lower, this filter is expected to show better performance when integrated in the full experimental setup.

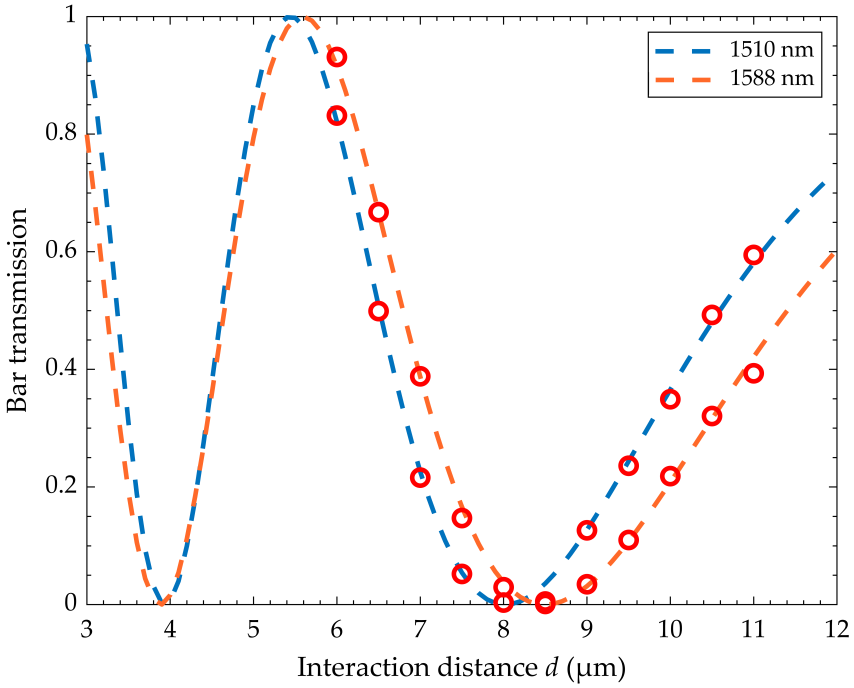

Figure 6.9: Normalized bar powers for wavelengths of 1510 and 1588 nm, for which the parameters a and b can then be calculated. Red circle represents the experimental point, dashed line the exponential fit.

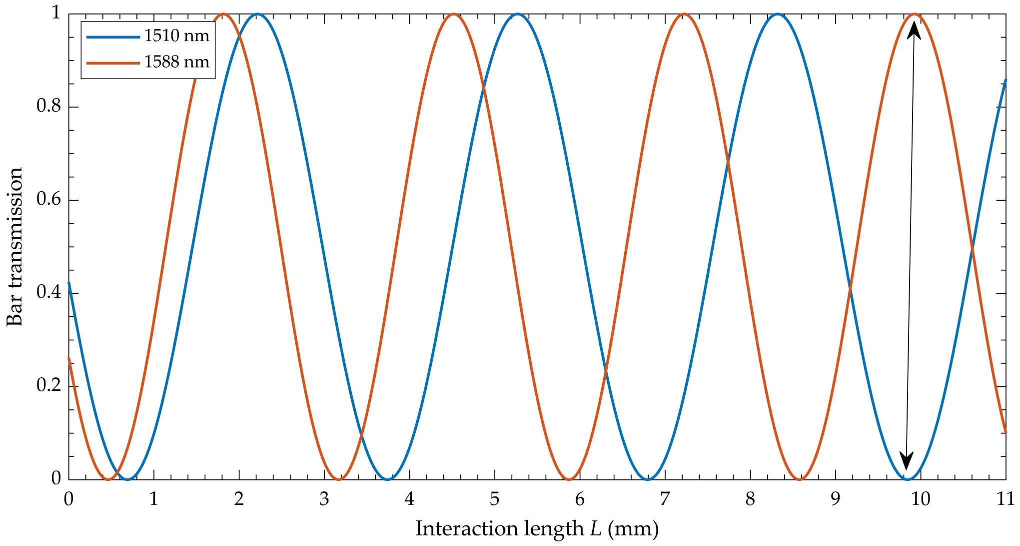

Figure 6.10: WDM simulation. The figure displays the trend of the normalized powers in Bar output port for the wavelengths of 1510 nm (blue line) and 1588 nm (orange line). The simulation indicates that the point of maximum division of the two wavelengths occurs at an interaction length L of 9.9 mm.

Conclusions and future developments

In this work, the fabrication and characterization of a Wavelength Division Multiplexer fabricated via femtosecond laser micromachining has been presented. This component is fundamental for the implementation of a heralded integrated single-photon source, as it allows the division of heralding from heralded photons. The component should feature low losses and high extinction ratio (ER), which is defined as the ratio between the power transmitted in the target output port with respect to the one in the other port.

For the realization of this component, we decided to exploit the dependence on wavelength of the coupling coefficient in standard directional couplers. In particular, we started the experimental activity by analysing the behaviour of directional couplers as a function both of the interaction distance and the wavelength. Once we have retrieved the coupling coefficient in our femtosecond laser written devices, we run a multiparameter (interaction distance d, interaction length L) simulations to find the optimal d and L values for the fabrication of an efficient WDM.

The first part of the thesis involved the fabrication of the WDMs on the well-known EAGLE XG borosilicate glass substrate. The WDMs were designed to operate at the typical telecom wavelengths of 1550 nm and 1310 nm and in a narrower wavelength range of 1510 nm and 1588 nm. The best WDM showed ER values of 24 dB and 22 dB at 1550 nm and 1310 nm wavelengths, respectively. The device working at 1510 and 1588 nm showed ER values of 17 and 16 dB, respectivily. As expected, the latter device showed lower values of the extinction ratio. Indeed, being the wavelengths to be divided closer and the difference in the coupling coefficients smaller, a directional coupler with a longer interaction length was required. In general, the longer the propagation distance, the higher is the sensitivity to fluctuations during the fabrication process.
In the second part, driven by the need to achieve lower losses, a new material was studied, namely Borofloat 33. In this case, before the realization of the WDM, it was necessary to carry out an optimization almost from scratch, i.e. starting from the optimization of the straight waveguides up to the directional couplers. The optimization was conducted for a wavelength range of 100 nm around 1550 nm. Effectively, the use of Borofloat has led to a clear reduction in propagation losses, measuring around 0.03 dB/cm, around a factor of 6

less than the competitor EAGLE XG, which had propagation losses of around 0.16 dB/cm. Although our fabrication process in Borofloat led to one of the lowest PL values found in the literature for femtosecond laser written waveguides, the achieved mode confinement led to much worse values of bending losses, with values comparable to EAGLE XG only for bending radii of 60 mm. In addition, our fabrication process in Borofloat showed lower reproducibility. In fact, even keeping the same parameters, the fabricated waveguides showed not negligible differences both in guiding performance (PL, BL and coupling losses) as well as in their morphology. Reviewing the various fabrications, these run-to-run variations were attributed to a high sensitivity of the process on the writing depth, which may limit the advantage of 3D capability of femtosecond laser micromachining. Since the component we devised in this thesis was essentially planar, we decided to proceed with its fabrication. In particular, we realized a WDM for dividing photons at 1510 nm from the ones at 1588 nm with an extinction ratio of 19 dB for both wavelengths. In conclusion, this WDM showed in line or even better performance than the other femtosecond laser written devices reported in literature.

Being propagation losses of laser-written waveguides in Borofloat so promising, future developments would aim at the optimization of the fabrication process to enhance the 3D capability for this substrate. Reduction in bending losses would potentially make this platform as a competitive technology for the realization of complex universal linear optical networks [35]. In the general framework of the integrated heralded single-photon source, the next steps require the optimization of the nonlinear crystal for the generation of high purity and indistinguishable photons and the development of the filter for pump suppression.

Bibliography

[1] Han-Sen Zhong, Yu-Hao Deng, Jian Qin, Hui Wang, Ming-Cheng Chen, Li-Chao Peng, Yi-Han Luo, Dian Wu, Si-Qiu Gong, Hao Su, Yi Hu, Peng Hu, Xiao-Yan Yang, Wei-Jun Zhang, Hao Li, Yuxuan Li, Xiao Jiang, Lin Gan, Guangwen Yang, Lixing You, Zhen Wang, Li Li, Nai-Le Liu, Jelmer J. Renema, Chao-Yang Lu, and Jian-Wei Pan. Phase-programmable gaussian boson sampling using stimulated squeezed light. *Phys. Rev. Lett.*, 127:180502, Oct 2021. doi: 10.1103/PhysRevLett.127.180502. URL `https://link.aps.org/doi/10.1103/PhysRevLett.127.180502`.

[2] Shankhadip Kundu, Rajdeep Kundu, Shubhabrata Kundu, Anubhab Bhattachaijee, Sayantan Gupta, Souvik Ghosh, and Indranil Basu. Quantum computation: From church-turing thesis to qubits. pages 1–5, 2016. doi: 10.1109/UEMCON.2016.7777805.

[3] Michael A. Nielsen and Isaac L. Chuang. *Quantum Computation and Quantum Information*. Cambridge University Press, 2000.

[4] Andrew Steane. Quantum computing. *Reports on Progress in Physics*, 61(2):117–173, Feb 1998. ISSN 1361-6633. doi: 10.1088/0034-4885/61/2/002. URL `http://dx.doi.org/10.1088/0034-4885/61/2/002`.

[5] R. P. Feynman. Simulating physics with computers. *International Journal of Theoretical Physics*, 21(6):467–488, 1982.

[6] David Collins, K. W. Kim, and W. C. Holton. Deutsch-jozsa algorithm as a test of quantum computation. *Phys. Rev. A*, 58:R1633–R1636, Sep 1998. doi: 10.1103/PhysRevA.58.R1633. URL `https://link.aps.org/doi/10.1103/PhysRevA.58.R1633`.

[7] Artur Ekert and Richard Jozsa. Quantum computation and shor's factoring algorithm. *Rev. Mod. Phys.*, 68:733–753, Jul 1996. doi: 10.1103/RevModPhys.68.733. URL `https://link.aps.org/doi/10.1103/RevModPhys.68.733`.

[8] John Proos and Christof Zalka. Shor's discrete logarithm quantum algorithm for elliptic curves. *arXiv preprint quant-ph/0301141*, 2003.

[9] Michele Mosca and Christof Zalka. Exact quantum fourier transforms and discrete logarithm algorithms. *International Journal of Quantum Information*, 2(01):91–100, 2004.

[10] P. G. Kwiat, J. R. Mitchell, P. D. D. Schwindt, and A. G. White. Grover's search algorithm: An optical approach. *Journal of Modern Optics*, 47(2-3):257–266, 2000. doi: 10.1080/09500340008244040.

[11] Frank Arute, Kunal Arya, Ryan Babbush, Dave Bacon, Joseph C Bardin, Rami Barends, Rupak Biswas, Sergio Boixo, Fernando GSL Brandao, David A Buell, et al. Quantum supremacy using a programmable superconducting processor. *Nature*, 574 (7779):505–510, 2019.

[12] Frank Arute, Kunal Arya, Ryan Babbush, Dave Bacon, Joseph C Bardin, Rami Barends, Sergio Boixo, Michael Broughton, Bob B Buckley, David A Buell, et al. Hartree-fock on a superconducting qubit quantum computer. *Science*, 369(6507): 1084–1089, 2020.

[13] Yulin Wu, Wan-Su Bao, Sirui Cao, Fusheng Chen, Ming-Cheng Chen, Xiawei Chen, Tung-Hsun Chung, Hui Deng, Yajie Du, Daojin Fan, Ming Gong, Cheng Guo, Chu Guo, Shaojun Guo, Lianchen Han, Linyin Hong, He-Liang Huang, Yong-Heng Huo, Liping Li, Na Li, Shaowei Li, Yuan Li, Futian Liang, Chun Lin, Jin Lin, Haoran Qian, Dan Qiao, Hao Rong, Hong Su, Lihua Sun, Liangyuan Wang, Shiyu Wang, Dachao Wu, Yu Xu, Kai Yan, Weifeng Yang, Yang Yang, Yangsen Ye, Jianghan Yin, Chong Ying, Jiale Yu, Chen Zha, Cha Zhang, Haibin Zhang, Kaili Zhang, Yiming Zhang, Han Zhao, Youwei Zhao, Liang Zhou, Qingling Zhu, Chao-Yang Lu, Cheng-Zhi Peng, Xiaobo Zhu, and Jian-Wei Pan. Strong quantum computational advantage using a superconducting quantum processor. *Phys. Rev. Lett.*, 127:180501, Oct 2021. doi: 10.1103/PhysRevLett.127.180501. URL `https://link.aps.org/doi/10.1103/PhysRevLett.127.180501`.

[14] Han-Sen Zhong, Hui Wang, Yu-Hao Deng, Ming-Cheng Chen, Li-Chao Peng, Yi-Han Luo, Jian Qin, Dian Wu, Xing Ding, Yi Hu, et al. Quantum computational advantage using photons. *Science*, 370(6523):1460–1463, 2020.

[15] Giuliano Benenti, Giulio Casati, Davide Rossini, and Giuliano Strini. *Principles of Quantum Computation and Information: A Comprehensive Textbook*. World Scientific, 2019.

[16] Yuchen Wang, Zixuan Hu, Barry C. Sanders, and Sabre Kais. Qudits and high-dimensional quantum computing. *Frontiers in Physics*, 8, 2020. ISSN 2296-424X.

doi: 10.3389/fphy.2020.589504. URL `https://www.frontiersin.org/article/10.3389/fphy.2020.589504`.

[17] Fulvio Flamini, Nicolò Spagnolo, and Fabio Sciarrino. Photonic quantum information processing: a review. *Reports on Progress in Physics*, 82(1):016001, nov 2018. doi: 10.1088/1361-6633/aad5b2. URL `https://doi.org/10.1088/1361-6633/aad5b2`.

[18] Boris B Blinov, Dietrich Leibfried, C Monroe, and David J Wineland. Quantum computing with trapped ion hyperfine qubits. *Quantum Information Processing*, 3 (1):45–59, 2004.

[19] Seth Lloyd. Almost any quantum logic gate is universal. *Phys. Rev. Lett.*, 75:346–349, Jul 1995. doi: 10.1103/PhysRevLett.75.346. URL `https://link.aps.org/doi/10.1103/PhysRevLett.75.346`.

[20] Yuriy Makhlin. Nonlocal properties of two-qubit gates and mixed states, and the optimization of quantum computations. *Quantum Information Processing*, 1(4): 243–252, 2002.

[21] Jeremy L. O'Brien. Optical quantum computing. *Science*, 318(5856):1567–1570, Dec 2007. ISSN 1095-9203. doi: 10.1126/science.1142892. URL `http://dx.doi.org/10.1126/science.1142892`.

[22] Francesco Ceccarelli, Simone Atzeni, Alessandro Prencipe, Raffaele Farinaro, and Roberto Osellame. Thermal phase shifters for femtosecond laser written photonic integrated circuits. *Journal of Lightwave Technology*, 37(17):4275–4281, 2019. doi: 10.1109/JLT.2019.2923126.

[23] Emanuel Knill, Raymond Laflamme, and Gerald J Milburn. A scheme for efficient quantum computation with linear optics. *nature*, 409(6816):46–52, 2001.

[24] T. C. Ralph, N. K. Langford, T. B. Bell, and A. G. White. Linear optical controlled-not gate in the coincidence basis. *Phys. Rev. A*, 65:062324, Jun 2002. doi: 10.1103/PhysRevA.65.062324. URL `https://link.aps.org/doi/10.1103/PhysRevA.65.062324`.

[25] Ilya Fushman, Dirk Englund, Andrei Faraon, Nick Stoltz, Pierre Petroff, and Jelena Vučković. Controlled phase shifts with a single quantum dot. *science*, 320(5877): 769–772, 2008.

[26] J. D. Franson, B. C. Jacobs, and T. B. Pittman. Quantum computing using single photons and the zeno effect. *Phys. Rev. A*, 70:062302, Dec 2004. doi: 10.1103/

PhysRevA.70.062302. URL `https://link.aps.org/doi/10.1103/PhysRevA.70.062302`.

[27] Peter Lodahl. Quantum-dot based photonic quantum networks. *Quantum Science and Technology*, 3(1):013001, 2017.

[28] Daniel B Higginbottom, Lukáš Slodička, Gabriel Araneda, Lukáš Lachman, Radim Filip, Markus Hennrich, and Rainer Blatt. Pure single photons from a trapped atom source. *New Journal of Physics*, 18(9):093038, 2016.

[29] Julia Benedikter, Hanno Kaupp, Thomas Hümmer, Yuejiang Liang, Alexander Bommer, Christoph Becher, Anke Krueger, Jason M Smith, Theodor W Hänsch, and David Hunger. Cavity-enhanced single-photon source based on the silicon-vacancy center in diamond. *Physical Review Applied*, 7(2):024031, 2017.

[30] Hiroshi Fukuda, Koji Yamada, Tetsufumi Shoji, Mitsutoshi Takahashi, Tai Tsuchizawa, Toshifumi Watanabe, Jun-ichi Takahashi, and Sei-ichi Itabashi. Four-wave mixing in silicon wire waveguides. *Optics express*, 13(12):4629–4637, 2005.

[31] Steven Rogers, Daniel Mulkey, Xiyuan Lu, Wei C Jiang, and Qiang Lin. High visibility time-energy entangled photons from a silicon nanophotonic chip. *ACS photonics*, 3(10):1754–1761, 2016.

[32] Christophe Couteau. Spontaneous parametric down-conversion. *Contemporary Physics*, 59(3):291–304, 2018.

[33] T Tsuchizawa, L Vivien, and L Pavesi. Guided light in silicon-based materials. In *handbook of Silicon photonics*. CRC Press, 2013.

[34] Alberto Politi, Martin J Cryan, John G Rarity, Siyuan Yu, and Jeremy L O'brien. Silica-on-silicon waveguide quantum circuits. *Science*, 320(5876):646–649, 2008.

[35] Caterina Taballione, Malaquias Correa Anguita, Michiel de Goede, Pim Venderbosch, Ben Kassenberg, Henk Snijders, Devin Smith, Jörn P Epping, Reinier van der Meer, Pepijn WH Pinkse, et al. 20-mode universal quantum photonic processor. *arXiv preprint arXiv:2203.01801*, 2022.

[36] M Svalgaard, CV Poulsen, A Bjarklev, and Ole Poulsen. Direct uv writing of buried singlemode channel waveguides in ge-doped silica films. *Electronics Letters*, 30(17):1401–1403, 1994.

[37] R. Osellame, G. Cerullo, and R. Ramponi. *Femtosecond Laser Micromachining: Photonic and Microfluidic Devices in Transparent Materials*. Topics in Applied

Physics. Springer Berlin Heidelberg, 2012. ISBN 9783642233678. URL `https://books.google.it/books?id=aIgIswEACAAJ`.

[38] Lucian C Comandar, Bernd Fröhlich, James F Dynes, Andrew W Sharpe, Marco Lucamarini, ZL Yuan, Richard V Penty, and Andrew J Shields. Gigahertz-gated ingaas/inp single-photon detector with detection efficiency exceeding 55% at 1550 nm. *Journal of Applied Physics*, 117(8):083109, 2015.

[39] Qianchun Weng, Zhenghua An, Bo Zhang, Pingping Chen, Xiaoshuang Chen, Ziqiang Zhu, and Wei Lu. Quantum dot single-photon switches of resonant tunneling current for discriminating-photon-number detection. *Scientific reports*, 5(1): 1–5, 2015.

[40] Zhizhong Yan, Deny R Hamel, Aimee K Heinrichs, Xudong Jiang, Mark A Itzler, and Thomas Jennewein. An ultra low noise telecom wavelength free running single photon detector using negative feedback avalanche diode. *Review of Scientific Instruments*, 83(7):073105, 2012.

[41] Hao Li, Lu Zhang, Lixing You, Xiaoyan Yang, Weijun Zhang, Xiaoyu Liu, Sijing Chen, Zhen Wang, and Xiaoming Xie. Large-sensitive-area superconducting nanowire single-photon detector at 850 nm with high detection efficiency. *Optics express*, 23(13):17301–17308, 2015.

[42] Robert M Heath, Michael G Tanner, Alessandro Casaburi, Mark G Webster, Lara San Emeterio Alvarez, Weitao Jiang, Zoe H Barber, Richard J Warburton, and Robert H Hadfield. Nano-optical observation of cascade switching in a parallel superconducting nanowire single photon detector. *Applied physics letters*, 104(6): 063503, 2014.

[43] M Avenhaus, K Laiho, MV Chekhova, and Ch Silberhorn. Accessing higher order correlations in quantum optical states by time multiplexing. *Physical review letters*, 104(6):063602, 2010.

[44] Yongbo Yuan, Qingfeng Dong, Bin Yang, Fawen Guo, Qi Zhang, Ming Han, and Jinsong Huang. Solution-processed nanoparticle super-float-gated organic field-effect transistor as un-cooled ultraviolet and infrared photon counter. *Scientific reports*, 3(1):1–7, 2013.

[45] Aaron J Miller, Adriana E Lita, Brice Calkins, Igor Vayshenker, Steven M Gruber, and Sae Woo Nam. Compact cryogenic self-aligning fiber-to-detector coupling with losses below one percent. *Optics express*, 19(10):9102–9110, 2011.

[46] Scott Aaronson and Alex Arkhipov. The computational complexity of linear optics. In *Proceedings of the forty-third annual ACM symposium on Theory of computing*, pages 333–342, 2011.

[47] Joonsuk Huh, Gian Giacomo Guerreschi, Borja Peropadre, Jarrod R McClean, and Alán Aspuru-Guzik. Boson sampling for molecular vibronic spectra. *Nature Photonics*, 9(9):615–620, 2015.

[48] Diego González Olivares, Borja Peropadre, Alán Aspuru-Guzik, and Juan José García-Ripoll. Quantum simulation with a boson sampling circuit. *Physical Review A*, 94(2):022319, 2016.

[49] Chris Sparrow, Enrique Martín-López, Nicola Maraviglia, Alex Neville, Christopher Harrold, Jacques Carolan, Yogesh N Joglekar, Toshikazu Hashimoto, Nobuyuki Matsuda, Jeremy L O'Brien, et al. Simulating the vibrational quantum dynamics of molecules using photonics. *Nature*, 557(7707):660–667, 2018.

[50] Lidror Troyansky and Naftali Tishby. On the quantum evaluation of the determinant and the permanent of a matrix. *Proc. Phys. Comput*, page 96, 1996.

[51] L.G. Valiant. The complexity of computing the permanent. *Theoretical Computer Science*, 8(2):189–201, 1979. ISSN 0304-3975. doi: https://doi.org/10.1016/0304-3975(79)90044-6. URL `https://www.sciencedirect.com/science/article/pii/0304397579900446`.

[52] Peter Clifford and Raphaël Clifford. The classical complexity of boson sampling. In *Proceedings of the Twenty-Ninth Annual ACM-SIAM Symposium on Discrete Algorithms*, pages 146–155. SIAM, 2018.

[53] Agata M Brańczyk. Hong-ou-mandel interference. *arXiv preprint arXiv:1711.00080*, 2017.

[54] A. P. Lund, A. Laing, S. Rahimi-Keshari, T. Rudolph, J. L. O'Brien, and T. C. Ralph. Boson sampling from a gaussian state. *Phys. Rev. Lett.*, 113:100502, Sep 2014. doi: 10.1103/PhysRevLett.113.100502. URL `https://link.aps.org/doi/10.1103/PhysRevLett.113.100502`.

[55] Chris Palmer. Quantum computing quickly scores second claim of supremacy, 2021.

[56] Nicolás Quesada, Juan Miguel Arrazola, and Nathan Killoran. Gaussian boson sampling using threshold detectors. *Phys. Rev. A*, 98:062322, Dec 2018. doi: 10.1103/PhysRevA.98.062322. URL `https://link.aps.org/doi/10.1103/PhysRevA.98.062322`.

[57] Andrea Crespi, Roberto Osellame, Roberta Ramponi, Daniel J Brod, Ernesto F Galvao, Nicolo Spagnolo, Chiara Vitelli, Enrico Maiorino, Paolo Mataloni, and Fabio Sciarrino. Integrated multimode interferometers with arbitrary designs for photonic boson sampling. *Nature photonics*, 7(7):545–549, 2013.

[58] Justin B Spring, Benjamin J Metcalf, Peter C Humphreys, W Steven Kolthammer, Xian-Min Jin, Marco Barbieri, Animesh Datta, Nicholas Thomas-Peter, Nathan K Langford, Dmytro Kundys, et al. Boson sampling on a photonic chip. *Science*, 339 (6121):798–801, 2013.

[59] Han-Sen Zhong, Yuan Li, Wei Li, Li-Chao Peng, Zu-En Su, Yi Hu, Yu-Ming He, Xing Ding, Weijun Zhang, Hao Li, et al. 12-photon entanglement and scalable scattershot boson sampling with optimal entangled-photon pairs from parametric down-conversion. *Physical review letters*, 121(25):250505, 2018.

[60] Stefano Paesani, Yunhong Ding, Raffaele Santagati, Levon Chakhmakhchyan, Caterina Vigliar, Karsten Rottwitt, Leif Oxenløwe, Jianwei Wang, Mark Thompson, and Anthony Laing. Generation and sampling of quantum states of light in a silicon chip. *Nature Physics*, 15:1, 09 2019. doi: 10.1038/s41567-019-0567-8.

[61] P Grünwald. Effective second-order correlation function and single-photon detection. *New Journal of Physics*, 21(9):093003, sep 2019. doi: 10.1088/1367-2630/ab3ae0. URL `https://doi.org/10.1088/1367-2630/ab3ae0`.

[62] Jonathan C. F. Matthews. *The Hong–Ou–Mandel Effect in a Waveguide Directional Coupler*, pages 29–40. Springer Berlin Heidelberg, Berlin, Heidelberg, 2013. ISBN 978-3-642-32870-1. doi: 10.1007/978-3-642-32870-1_3. URL `https://doi.org/10.1007/978-3-642-32870-1_3`.

[63] Jun Chen, Aaron J. Pearlman, Alexander Ling, Jingyun Fan, and Alan Migdall. A versatile waveguide source of photon pairs for chip-scale quantum information processing. *Opt. Express*, 17(8):6727–6740, Apr 2009. doi: 10.1364/OE.17.006727. URL `http://opg.optica.org/oe/abstract.cfm?URI=oe-17-8-6727`.

[64] Simone Atzeni, Adil S. Rab, Giacomo Corrielli, Emanuele Polino, Mauro Valeri, Paolo Mataloni, Nicolò Spagnolo, Andrea Crespi, Fabio Sciarrino, and Roberto Osellame. Integrated sources of entangled photons at the telecom wavelength in femtosecond-laser-written circuits. *Optica*, 5(3):311–314, Mar 2018. doi: 10.1364/OPTICA.5.000311. URL `http://opg.optica.org/optica/abstract.cfm?URI=optica-5-3-311`.

[65] Justin B. Spring, Paolo L. Mennea, Benjamin J. Metcalf, Peter C. Humphreys,

James C. Gates, Helen L. Rogers, Christoph Söller, Brian J. Smith, W. Steven Kolthammer, Peter G. R. Smith, and Ian A. Walmsley. Chip-based array of near-identical, pure, heralded single-photon sources. *Optica*, 4(1):90–96, Jan 2017. doi: 10.1364/OPTICA.4.000090. URL `http://opg.optica.org/optica/abstract.cfm?URI=optica-4-1-90`.

[66] Stefano Paesani, Massimo Borghi, Stefano Signorini, Alexandre Maïnos, Lorenzo Pavesi, and Anthony Laing. Near-ideal spontaneous photon sources in silicon quantum photonics. *Nature communications*, 11(1):1–6, 2020.

[67] Panagiotis Vergyris, Thomas Meany, Tommaso Lunghi, Gregory Sauder, James Downes, MJ Steel, Michael J Withford, Olivier Alibart, and Sébastien Tanzilli. On-chip generation of heralded photon-number states. *Scientific reports*, 6(1):1–6, 2016.

[68] Matthew D Eisaman, Jingyun Fan, Alan Migdall, and Sergey V Polyakov. Invited review article: Single-photon sources and detectors. *Review of scientific instruments*, 82(7):071101, 2011.

[69] Junyi Lee, Victor Leong, Dmitry Kalashnikov, Jibo Dai, Alagappan Gandhi, and Leonid A Krivitsky. Integrated single photon emitters. *AVS Quantum Science*, 2 (3):031701, 2020.

[70] Sergei Slussarenko and Geoff J Pryde. Photonic quantum information processing: A concise review. *Applied Physics Reviews*, 6(4):041303, 2019.

[71] Yan Chen, Michael Zopf, Robert Keil, Fei Ding, and Oliver G Schmidt. Highly-efficient extraction of entangled photons from quantum dots using a broadband optical antenna. *Nature communications*, 9(1):1–7, 2018.

[72] Sara L. Mouradian, Tim Schröder, Carl B. Poitras, Luozhou Li, Jordan Goldstein, Edward H. Chen, Michael Walsh, Jaime Cardenas, Matthew L. Markham, Daniel J. Twitchen, Michal Lipson, and Dirk Englund. Scalable integration of long-lived quantum memories into a photonic circuit. *Phys. Rev. X*, 5:031009, Jul 2015. doi: 10.1103/PhysRevX.5.031009. URL `https://link.aps.org/doi/10.1103/PhysRevX.5.031009`.

[73] Christian Hepp, Tina Müller, Victor Waselowski, Jonas N Becker, Benjamin Pingault, Hadwig Sternschulte, Doris Steinmüller-Nethl, Adam Gali, Jeronimo R Maze, Mete Atatüre, et al. Electronic structure of the silicon vacancy color center in diamond. *Physical Review Letters*, 112(3):036405, 2014.

[74] Takayuki Iwasaki, Fumitaka Ishibashi, Yoshiyuki Miyamoto, Satoshi Kobayashi, Takehide Miyazaki, Kosuke Tahara, Kay D Jahnke, Lachlan J Rogers, Boris Naydenov, Fedor Jelezko, et al. Germanium-vacancy single color centers in diamond. *Scientific reports*, 5(1):1–7, 2015.

[75] Takayuki Iwasaki, Yoshiyuki Miyamoto, Takashi Taniguchi, Petr Siyushev, Mathias H Metsch, Fedor Jelezko, and Mutsuko Hatano. Tin-vacancy quantum emitters in diamond. *Physical review letters*, 119(25):253601, 2017.

[76] Birgit JM Hausmann, Brendan Shields, Qimin Quan, Patrick Maletinsky, Murray McCutcheon, Jennifer T Choy, Tom M Babinec, Alexander Kubanek, Amir Yacoby, Mikhail D Lukin, et al. Integrated diamond networks for quantum nanophotonics. *Nano letters*, 12(3):1578–1582, 2012.

[77] Sara Mouradian, Noel H Wan, Tim Schröder, and Dirk Englund. Rectangular photonic crystal nanobeam cavities in bulk diamond. *Applied Physics Letters*, 111 (2):021103, 2017.

[78] JS Hodges, L Li, M Lu, EH Chen, ME Trusheim, S Allegri, X Yao, O Gaathon, H Bakhru, and D Englund. Long-lived nv- spin coherence in high-purity diamond membranes. *New Journal of Physics*, 14(9):093004, 2012.

[79] Christof P Dietrich, Andrea Fiore, Mark G Thompson, Martin Kamp, and Sven Höfling. Gaas integrated quantum photonics: Towards compact and multifunctional quantum photonic integrated circuits. *Laser & Photonics Reviews*, 10 (6):870–894, 2016.

[80] Je-Hyung Kim, Shahriar Aghaeimeibodi, Christopher JK Richardson, Richard P Leavitt, Dirk Englund, and Edo Waks. Hybrid integration of solid-state quantum emitters on a silicon photonic chip. *Nano letters*, 17(12):7394–7400, 2017.

[81] Peter Schnauber, Anshuman Singh, Johannes Schall, Suk In Park, Jin Dong Song, Sven Rodt, Kartik Srinivasan, Stephan Reitzenstein, and Marcelo Davanco. Indistinguishable photons from deterministically integrated single quantum dots in heterogeneous gaas/si3n4 quantum photonic circuits. *Nano letters*, 19(10):7164–7172, 2019.

[82] Thomas Hummel, Claudéric Ouellet-Plamondon, Ela Ugur, Irina Kulkova, Toke Lund-Hansen, Matthew A Broome, Ravitej Uppu, and Peter Lodahl. Efficient demultiplexed single-photon source with a quantum dot coupled to a nanophotonic waveguide. *Applied Physics Letters*, 115(2):021102, 2019.

[83] Gabija Kiršanskė, Henri Thyrrestrup, Raphaël S. Daveau, Chris L. Dreeßen, Tommaso Pregnolato, Leonardo Midolo, Petru Tighineanu, Alisa Javadi, Søren Stobbe, Rüdiger Schott, Arne Ludwig, Andreas D. Wieck, Suk In Park, Jin D. Song, Andreas V. Kuhlmann, Immo Söllner, Matthias C. Löbl, Richard J. Warburton, and Peter Lodahl. Indistinguishable and efficient single photons from a quantum dot in a planar nanobeam waveguide. *Phys. Rev. B*, 96:165306, Oct 2017. doi: 10.1103/PhysRevB.96.165306. URL `https://link.aps.org/doi/10.1103/PhysRevB.96.165306`.

[84] Matthias Bock, Andreas Lenhard, Christopher Chunnilall, and Christoph Becher. Highly efficient heralded single-photon source for telecom wavelengths based on a ppln waveguide. *Opt. Express*, 24(21):23992–24001, Oct 2016. doi: 10.1364/OE.24.023992. URL `http://opg.optica.org/oe/abstract.cfm?URI=oe-24-21-23992`.

[85] Daniel J Brod, Ernesto F Galvão, Andrea Crespi, Roberto Osellame, Nicolò Spagnolo, and Fabio Sciarrino. Photonic implementation of boson sampling: a review. *Advanced Photonics*, 1(3):034001, 2019.

[86] Nicholas C. Harris, Davide Grassani, Angelica Simbula, Mihir Pant, Matteo Galli, Tom Baehr-Jones, Michael Hochberg, Dirk Englund, Daniele Bajoni, and Christophe Galland. Integrated source of spectrally filtered correlated photons for large-scale quantum photonic systems. *Phys. Rev. X*, 4:041047, Dec 2014. doi: 10.1103/PhysRevX.4.041047. URL `https://link.aps.org/doi/10.1103/PhysRevX.4.041047`.

[87] Jiayang Wu, Tania Moein, Xingyuan Xu, Guanghui Ren, Arnan Mitchell, and David J. Moss. Micro-ring resonator quality factor enhancement via an integrated fabry-perot cavity. *APL Photonics*, 2(5), May 2017. ISSN 2378-0967. doi: 10.1063/1.4981392.

[88] Stephan Krapick, Harald Herrmann, Viktor Quiring, Benjamin Brecht, Hubertus Suche, and Ch Silberhorn. An efficient integrated two-color source for heralded single photons. *New Journal of Physics*, 15(3):033010, 2013.

[89] Andreas Boes, Thach G Nguyen, Lin Chang, John E Bowers, Guanghui Ren, and Arnan Mitchell. Integrated photonic high extinction short and long pass filters based on lateral leakage. *Optics Express*, 29(12):18905–18914, 2021.

[90] K. M. Davis, K. Miura, N. Sugimoto, and K. Hirao. Writing waveguides in glass with a femtosecond laser. *Opt. Lett.*, 21(21):1729–1731, Nov 1996. doi: 10.

1364/OL.21.001729. URL `http://www.osapublishing.org/ol/abstract.cfm?URI=ol-21-21-1729`.

[91] JH Schmid, P Cheben, PJ Bock, R Halir, J Lapointe, S Janz, A Delage, A Densmore, J-M Fedeli, TJ Hall, et al. Refractive index engineering with subwavelength gratings in silicon microphotonic waveguides. *IEEE Photonics Journal*, 3(3):597–607, 2011.

[92] Michael J Shaw, Junpeng Guo, Gregory Allen Vawter, Scott Habermehl, and Charles T Sullivan. Fabrication techniques for low-loss silicon nitride waveguides. In *Micromachining Technology for Micro-Optics and Nano-Optics III*, volume 5720, pages 109–118. International Society for Optics and Photonics, 2005.

[93] Andrius Marcinkevičius, Saulius Juodkazis, Mitsuru Watanabe, Masafumi Miwa, Shigeki Matsuo, Hiroaki Misawa, and Junji Nishii. Femtosecond laser-assisted three-dimensional microfabrication in silica. *Opt. Lett.*, 26(5):277–279, Mar 2001. URL `http://www.osapublishing.org/ol/abstract.cfm?URI=ol-26-5-277`.

[94] L V Keldysh. Ionization in the field of a strong electromagnetic wave. *Zh. Eksperim. i Teor. Fiz.*, 47, 11 1964. URL `https://www.osti.gov/biblio/4662394`.

[95] Chris B Schaffer, André Brodeur, and Eric Mazur. Laser-induced breakdown and damage in bulk transparent materials induced by tightly focused femtosecond laser pulses. *Measurement Science and Technology*, 12(11), oct 2001. doi: 10.1088/0957-0233/12/11/305. URL `https://doi.org/10.1088/0957-0233/12/11/305`.

[96] Detao Du, Xila Liu, Georg Korn, Jeff Squier, and G. Mourou. Laser-induced breakdown by impact ionization in sio2 with pulse widths from 7 ns to 150 fs. *Applied Physics Letters*, 64:3071 – 3073, 07 1994. doi: 10.1063/1.111350.

[97] R. Osellame, Giuseppe Della Valle, N. Chiodo, Stefano Taccheo, P. Laporta, Orazio Svelto, and G. Cerullo. Lasing in femtosecond laser written optical waveguides. *Applied Physics A*, 93:17–26, 10 2008. doi: 10.1007/s00339-008-4644-6.

[98] B. C. Stuart, M. D. Feit, S. Herman, A. M. Rubenchik, B. W. Shore, and M. D. Perry. Nanosecond-to-femtosecond laser-induced breakdown in dielectrics. *Phys. Rev. B*, 53:1749–1761, Jan 1996. doi: 10.1103/PhysRevB.53.1749. URL `https://link.aps.org/doi/10.1103/PhysRevB.53.1749`.

[99] Masahiro Shimizu, Masaaki Sakakura, Masatoshi Ohnishi, Yasuhiko Shimotsuma, Takayuki Nakaya, Kiyotaka Miura, and Kazuyuki Hirao. Mechanism of heat-modification inside a glass after irradiation with high-repetition rate femtosecond laser pulses. *Journal of Applied Physics*, 108, 10 2010. doi: 10.1063/1.3483238.

[100] S. Nolte C.B. Schaffer K. Itoh, W. Watanabe. Ultrafast processes for bulk modification of transparent materials. *MRS Bulletin*, 31:620–625, 8 2006. doi: 10.1557/mrs2006.159. URL `https://doi.org/10.1557/mrs2006.159`.

[101] J. W. Chan, T. Huser, S. Risbud, and D. M. Krol. Structural changes in fused silica after exposure to focused femtosecond laser pulses. *Opt. Lett.*, 26(21):1726–1728, Nov 2001. doi: 10.1364/OL.26.001726. URL `http://www.osapublishing.org/ol/abstract.cfm?URI=ol-26-21-1726`.

[102] P. Dekker, M. Ams, G. D. Marshall, D. J. Little, and M. J. Withford. Annealing dynamics of waveguide bragg gratings: evidence of femtosecond laser induced colour centres. *Opt. Express*, 18(4):3274–3283, Feb 2010. URL `http://www.osapublishing.org/oe/abstract.cfm?URI=oe-18-4-3274`.

[103] Shingo Kanehira, Kiyotaka Miura, and Kazuyuki Hirao. Ion-exchange in glass using femtosecond laser irradiation. *Applied Physics Letters*, 93, 07 2008. doi: 10.1063/1.2959820.

[104] E.Simova P.P. Rajeev D.M.Rayner V.R.Bhardwaj P.B.Corkum C.Hnatovsky, R.S.Taylor. Fabrication of microchannels in glass using focused femtosecond laser radiation and selective chemical etching. *Applied Physics A*, 84(10):47–61, July 2006.

[105] S. Juodkazis, K. Nishimura, S. Tanaka, H. Misawa, E. G. Gamaly, B. Luther-Davies, L. Hallo, P. Nicolai, and V. T. Tikhonchuk. Laser-induced microexplosion confined in the bulk of a sapphire crystal: Evidence of multimegabar pressures. *Phys. Rev. Lett.*, 96:166101, Apr 2006. doi: 10.1103/PhysRevLett.96.166101. URL `https://link.aps.org/doi/10.1103/PhysRevLett.96.166101`.

[106] E. N. Glezer, M. Milosavljevic, L. Huang, R. J. Finlay, T.-H. Her, J. P. Callan, and E. Mazur. Three-dimensional optical storage inside transparent materials. *Opt. Lett.*, 21(24):2023–2025, Dec 1996. doi: 10.1364/OL.21.002023. URL `http://www.osapublishing.org/ol/abstract.cfm?URI=ol-21-24-2023`.

[107] S. Juodkazis, S. Matsuo, H. Misawa, V. Mizeikis, A. Marcinkevicius, H. B. Sun, Y. Tokuda, M. Takahashi, T. Yoko, and J. Nishii. Application of femtosecond laser pulses for microfabrication of transparent media. *Applied Surface Science*, 197-198: 705–709, 2002. doi: 10.1016/S0169-4332(02)00397-5.

[108] Shane M. Eaton, Haibin Zhang, Peter R. Herman, Fumiyo Yoshino, Lawrence Shah, James Bovatsek, and Alan Y. Arai. Heat accumulation effects in femtosecond laser-written waveguides with variable repetition rate. *Opt. Express*, 13(12):4708–4716,

Jun 2005. doi: 10.1364/OPEX.13.004708. URL `http://www.osapublishing.org/oe/abstract.cfm?URI=oe-13-12-4708`.

[109] Shane M. Eaton, Giulio Cerullo, and Roberto Osellame. *Fundamentals of Femtosecond Laser Modification of Bulk Dielectrics*, pages 3–18. Springer Berlin Heidelberg, Berlin, Heidelberg, 2012. ISBN 978-3-642-23366-1. doi: 10.1007/978-3-642-23366-1_1. URL `https://doi.org/10.1007/978-3-642-23366-1_1`.

[110] Shane Michael Eaton. *Contrasts in thermal diffusion and heat accumulation effects in the fabrication of waveguides in glasses using variable repetition rate femtosecond laser*. University of Toronto, 2008.

[111] G. Cerullo, R. Osellame, S. Taccheo, M. Marangoni, D. Polli, R. Ramponi, P. Laporta, and S. De Silvestri. Femtosecond micromachining of symmetric waveguides at 1.5 µm by astigmatic beam focusing. *Opt. Lett.*, 27(21):1938–1940, Nov 2002. doi: 10.1364/OL.27.001938. URL `http://www.osapublishing.org/ol/abstract.cfm?URI=ol-27-21-1938`.

[112] Jun Guan, Xiang Liu, and Martin J. Booth. Ultrafast laser writing quill effect in low loss waveguide fabrication regime. *Opt. Express*, 26(23):30716–30723, Nov 2018. doi: 10.1364/OE.26.030716. URL `http://www.osapublishing.org/oe/abstract.cfm?URI=oe-26-23-30716`.

[113] Douglas J. Little, Martin Ams, Peter Dekker, Graham D. Marshall, Judith M. Dawes, and Michael J. Withford. Femtosecond laser modification of fused silica: the effect of writing polarization on si-o ring structure. *Opt. Express*, 16(24):20029–20037, Nov 2008. doi: 10.1364/OE.16.020029. URL `http://www.osapublishing.org/oe/abstract.cfm?URI=oe-16-24-20029`.

[114] Lawrence Shah, Alan Y. Arai, Shane M. Eaton, and Peter R. Herman. Waveguide writing in fused silica with a femtosecond fiber laser at 522 nm and 1 mhz repetition rate. *Opt. Express*, 13(6):1999–2006, Mar 2005. doi: 10.1364/OPEX.13.001999. URL `http://www.osapublishing.org/oe/abstract.cfm?URI=oe-13-6-1999`.

[115] Shane M. Eaton, Haibin Zhang, Mi Li Ng, Jianzhao Li, Wei-Jen Chen, Stephen Ho, and Peter R. Herman. Transition from thermal diffusion to heat accumulation in high repetition rate femtosecond laser writing of buried optical waveguides. *Opt. Express*, 16(13):9443–9458, Jun 2008. doi: 10.1364/OE.16.009443. URL `http://www.osapublishing.org/oe/abstract.cfm?URI=oe-16-13-9443`.

[116] W. Vogel. *Glass Chemistry*. Springer-Verlag, 1994.

[117] Alexander Arriola, Simon Gross, Nemanja Jovanovic, Ned Charles, Peter G. Tuthill, Santiago M. Olaizola, Alexander Fuerbach, and Michael J. Withford. Low bend loss waveguides enable compact, efficient 3d photonic chips. *Opt. Express*, 21(3):2978–2986, Feb 2013. doi: 10.1364/OE.21.002978. URL `http://www.osapublishing.org/oe/abstract.cfm?URI=oe-21-3-2978`.

[118] René Heilmann, Chiara Greganti, Markus Gräfe, Stefan Nolte, Philip Walther, and Alexander Szameit. Tapering of femtosecond laser-written waveguides. *Appl. Opt.*, 57(3):377–381, Jan 2018. doi: 10.1364/AO.57.000377. URL `http://www.osapublishing.org/ao/abstract.cfm?URI=ao-57-3-377`.

[119] Tatsuhiko Aizawa and Tadahiko Inohara. *Pico- and Femtosecond Laser Micromachining for Surface Texturing.* 02 2019. ISBN 978-1-78923-809-9. doi: 10.5772/intechopen.83741.

[120] D. Gloge. Bending loss in multimode fibers with graded and ungraded core index. *Appl. Opt.*, 11(11):2506–2513, Nov 1972. doi: 10.1364/AO.11.002506. URL `http://www.osapublishing.org/ao/abstract.cfm?URI=ao-11-11-2506`.

[121] G. Corrielli. Integrated photonic circuits by femtosecond laser writing for qubit manipulation, quantum cryptography and quantum-optical analogies. PHD Thesis Politecnico di Milano, 2015.

[122] Shicheng Zhang, Wei Ji, Rui Yin, Xiao Li, Zisu Gong, and Lingyu Lv. Full bandwidth wavelength division multiplexer/demultiplexer based on mmi. *IEEE Photonics Technology Letters*, 30(1):107–110, 2018. doi: 10.1109/LPT.2017.2777669.

[123] Ali W Elshaari, Wolfram Pernice, Kartik Srinivasan, Oliver Benson, and Val Zwiller. Hybrid integrated quantum photonic circuits. *Nature photonics*, 14(5):285–298, 2020.

[124] Xiaojun Fang and Richard O. Claus. Polarization-independent all-fiber wavelength-division multiplexer based on a sagnac interferometer. *Opt. Lett.*, 20(20):2146–2148, Oct 1995. doi: 10.1364/OL.20.002146. URL `http://opg.optica.org/ol/abstract.cfm?URI=ol-20-20-2146`.

[125] F. Bilodeau, D.C. Johnson, S. Theriault, B. Malo, J. Albert, and K.O. Hill. An all-fiber dense wavelength-division multiplexer/demultiplexer using photoimprinted bragg gratings. *IEEE Photonics Technology Letters*, 7(4):388–390, 1995. doi: 10.1109/68.376811.

[126] Enrique AJ Marcatili. Dielectric rectangular waveguide and directional coupler for integrated optics. *Bell System Technical Journal*, 48(7):2071–2102, 1969.

[127] Arun Kumar, K Thyagarajan, and Ajoy K Ghatak. Analysis of rectangular-core dielectric waveguides: an accurate perturbation approach. *Optics letters*, 8(1):63–65, 1983.

[128] WP Huang and CL Xu. Simulation of three-dimensional optical waveguides by a full-vector beam propagation method. *IEEE journal of quantum electronics*, 29(10):2639–2649, 1993.

[129] A. Yariv. Coupled-mode theory for guided-wave optics. *IEEE Journal of Quantum Electronics*, 9(9):919–933, 1973. doi: 10.1109/JQE.1973.1077767.

[130] Dvir Munk, Moshe Katzman, Yuri Kaganovskii, Naor Inbar, Arijit Misra, Mirit Hen, Maayan Priel, Moshe Feldberg, Maria Tkachev, Arik Bergman, Menachem Vofsi, Michael Rosenbluh, Thomas Schneider, and Avi Zadok. Eight-channel silicon-photonic wavelength division multiplexer with 17 ghz spacing. *IEEE Journal of Selected Topics in Quantum Electronics*, 25(5):1–10, 2019. doi: 10.1109/JSTQE.2019.2904437.

[131] Jeong Hwan Song, Jong Hoon Lim, Ryun Kyung Kim, Kyung Shik Lee, Kyoung-Youm Kim, Jaegeol Cho, Dongkyoon Han, Suntae Jung, Yunkyung Oh, and Dong-Hoon Jang. Bragg grating-assisted wdm filter for integrated optical triplexer transceivers. *IEEE Photonics Technology Letters*, 17(12):2607–2609, 2005.

[132] Thomas Meany, Lutfi A Ngah, Matthew J Collins, Alex S Clark, Robert J Williams, Benjamin J Eggleton, MJ Steel, Michael J Withford, Olivier Alibart, and Sébastien Tanzilli. Hybrid photonic circuit for multiplexed heralded single photons. *Laser & photonics reviews*, 8(3):L42–L46, 2014.

[133] Wei-Jen Chen, Shane M. Eaton, Haibin Zhang, and Peter R. Herman. Broadband directional couplers fabricated in bulk glass with high repetition rate femtosecond laser pulses. *Opt. Express*, 16(15):11470–11480, Jul 2008. doi: 10.1364/OE.16.011470. URL `http://www.osapublishing.org/oe/abstract.cfm?URI=oe-16-15-11470`.

[134] Data sheet borofloat 33, . URL `https://psec.uchicago.edu/glass/borofloat_33_e.pdf`.

[135] Data sheet eagle xg, . URL `https://www.corning.com/media/worldwide/cdt/documents/EAGLE%20XG_PI%20Sheet_2021.pdf`.

[136] Toney Teddy Fernandez, Simon Gross, Alexander Arriola, Michael Withford, and

Karen Privat. Revisiting ultrafast laser inscribed waveguide formation in commercial alkali-free borosilicate glasses. *Optics Express*, 28, 03 2020. doi: 10.1364/OE.387790.

List of Figures

List of Tables

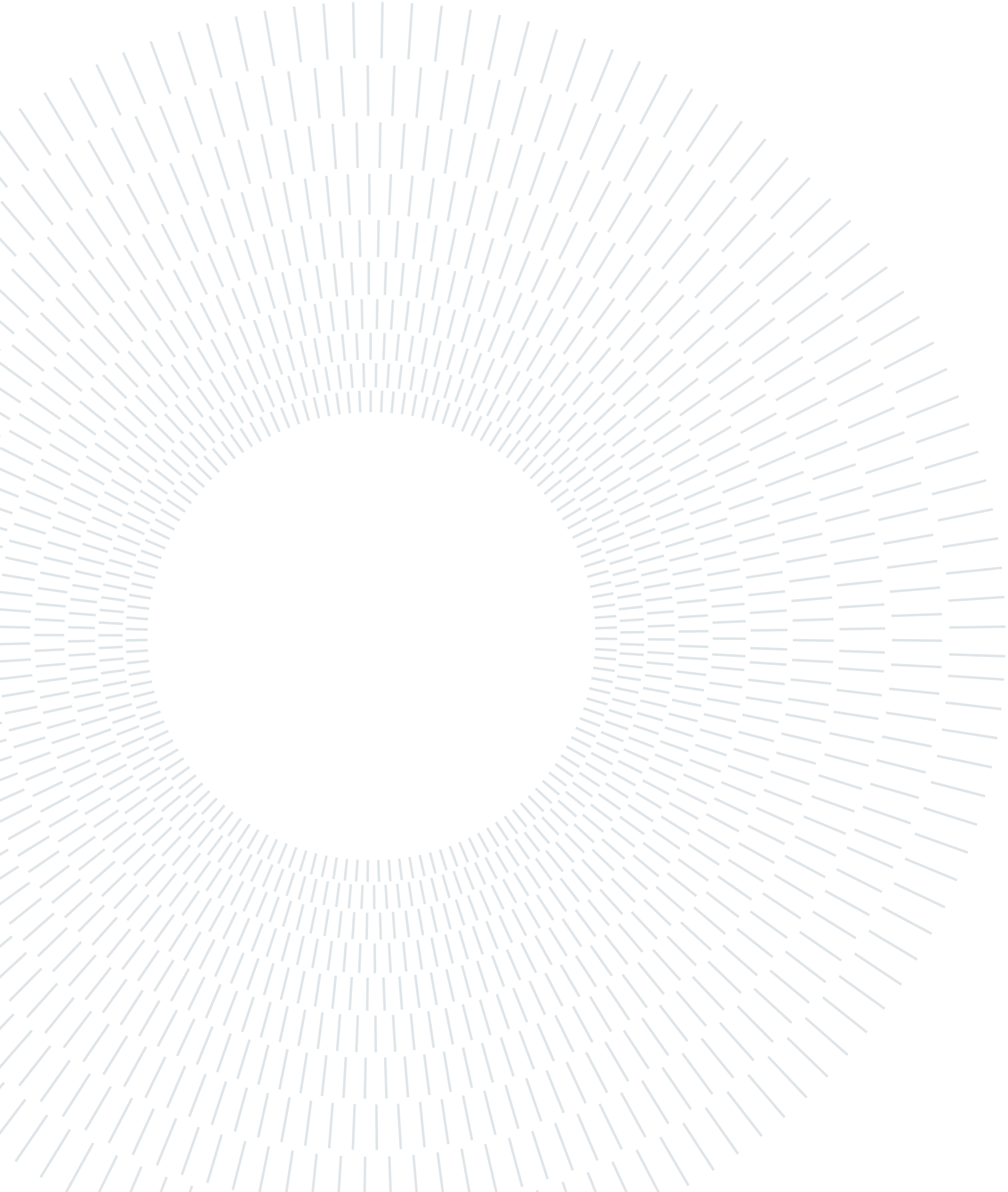

Ringraziamenti

Siamo giunti alla fine di questo percorso e quindi vorrei ringraziare tutte le persone che hanno reso possibile tutto ciò. Vorrei iniziare ringraziando il Dr. Roberto Osellame che mi ha offerto la possibilità di lavorare in questo interessante progetto di ricerca. Vorrei ringraziare gli "Osellami" per avermi accolto nel loro gruppo, in particolare vorrei ringraziare Simone per avermi introdotto nei laboratori, per avermi insegnato i primi passi nel mondo della fotonica e per avermi aiutato nella scrittura della tesi. Vorrei ringraziare il gruppo "photonic lunch" per tutti i pranzi e caffè passati insieme e i ragazzi del "photball" per i calcetti fotonici dopo lavoro. Un grazie a Hugo per aver trascorso insieme tante e tante ore nei lab a fabbricare e caratterizzare. Vorrei ringraziare Guglielmo ed Elena per tutti gli anni passati insieme al Poli. Un grandissimo grazie a tutti i miei amici, dai ragazzi di Casalècc' ai ragazzi di Lido di Classe e a Sara. Vorrei ringraziare tutti i miei familiari, ma in particolare i miei genitori che mi hanno sostenuto in tutto e per tutto e hanno creduto in me sin dal primo momento. Infine un grazie speciale va al mio compagno di vita e migliore amico: mio fratello Filippo. A tutti voi Grazie!